KU LEUVEN
GROEP WETENSCHAP & TECHNOLOGIE
DEPARTEMENT NATUURKUNDE EN STERRENKUNDE
AFDELING HALFGELEIDERFYSICA
Celestijnenlaan 200d-bus 2417, 3001 Leuven, België

Photoelectrochemical Study of n-GaN for Water Photoelectrolysis

Wei-Jhih TSENG

Members of the
Examination Committee:
Prof. Peter Lievens (chair)
Prof. Gustaaf Borghs (promoter)
Prof. Philippe Vereecken (co-promoter)
Prof. Roel Baets
Prof. Paolo Pescarmona
Dr. Ruben Lieten
Dr. Stefan Degroote

Dissertation presented in
partial fulfilment of the
requirements for the degree of
Doctor of Science

In collaboration with
Imec VZW
Kapeldreef 75
B-3001 Leuven, België

ISBN 978-90-8649-771-3
D/2014/10705/79

Acknowledgement

In Oct. 2008, I started the adventurous journey of pursuing a PhD degree. During these 5 years, I have chances to experience many ups and downs, bitterness and sweetness. It would be never possible to finish this journey without guidance, helps and supports scientifically or personally. At the very beginning of this dissertation, I would like to acknowledge people who are directly/indirectly involved in my PhD works.

First of all, I would like to express my deepest gratitude to my Promoter Prof. Gustaaf Borghs and co-Promoter Prof. Philippe Vereecken for this PhD opportunity and the scientific guidance. They have been continuously providing me constructive feedback and have been always scientist models to me. Second, I would like to thank my Supervisor Dr. Ruben Lieten for the Ph.D. project fund and his motivation and encouragement. I thank Prof. Peter Lievens, Prof. Roel Baets, Prof. Paolo Pescarmona and Dr. Stefan Degroote for their participation in my doctoral committee. Special thanks go to Dr. Dennis van Dorp for his scientific insight and discussion. Many achievements in this dissertation cannot be done without his help.

Many thanks go to technicians of the III-V clean room, the glass workshop (KUL) and the electrical workshop for a variety of technical assistances. Without their help, the development of device processing and the establishment of measurement setups were not be possible. I would like to thank my colleagues of the EPI group, particularly the EPI-GaN, and the ESTORE team for necessary material support in the dissertation.

Last but not least, I would like to express my deepest gratitude to my colleagues, friends, brothers and sisters of the international church in Leuven and my family for their support. Their unconditional love and acceptance have always been my biggest strength to move on during my PhD.

Abstract

Hydrogen, as a renewable chemical fuel, can be used to generate motive power and electricity in replacement of fossil energy. Water photoelectrolysis, using semiconductor photo-electrodes, is a sustainable and clean approach to produce hydrogen. Because of the right potential alignment to the redox potentials of water, GaN-based semiconductors have drawn much attention for the application of self-driven water photoelectrolysis.

In this dissertation, the photoelectrochemical properties of n-GaN have been investigated. Under illumination, n-GaN absorbs supra-bandgap light and generates photocarriers. Photo-holes participate in the following activities at the n-GaN anode: (1) oxidation of reductants in the solution, (2) photo-corrosion of GaN, (3) surface recombination and (4) carrier recombination in the bulk. Only the first process is desirable in the application of photoelectrolysis. We use different surface roughening approaches to suppress the 3rd and 4th processes. Br^-, as a sacrificial reducing agent, was added in the solution during the measurements to suppress the 2nd process.

First, the GaN epilayer has been modified into a nanopillar array using dry etching. The enlarged space charge region facilitates charge separation. The plateau photocurrent is therefore increased by 84 % with respect to planar GaN photoanode. Plasma-induced surface damage has been characterized by cyclic voltammetry and impedance spectroscopy. Surface damage of the pillars has been minimized by process engineering and post-wet etching.

The influence of porosity on the photoelectrochemical properties of n-GaN has been investigated. The n-GaN epilayer was porosified using electrochemical anodic etching. Anodic etching of n-GaN was discussed using cyclic voltammetry and chronoamperometry. In the porous GaN, space charge region is tremendously enlarged and charge neutral region is reduced. Carrier recombination at the surface and in the bulk is therefore suppressed. The plateau photocurrents for the porous GaN, etched at 5.5-15.0 V, increase over 400% with respect to pristine n-GaN.

Samenvatting

Waterstof is veelbelovend als hernieuwbare chemische brandstof voor het genereren van elektriciteit en aandrijfkracht, ter vervanging van fossiele energie. Water foto-elektrolyse, met behulp van halfgeleider-katalysatoren, is een duurzame en zuivere methode om waterstof te produceren. Door de juiste ligging van de energie banden ten opzichte van de water redox potentialen, krijgen GaN-gebaseerde halfgeleiders veel aandacht voor de toepassing van zelf-aangedreven water foto-elektrolyse.

In dit proefschrift worden de foto-elektrochemische eigenschappen van n-GaN behandelt. Onder belichting absorbeert n-type GaN supra-bandkloof licht en genereert vrije ladingsdragers. Foto-gaten nemen deel aan de volgende activiteiten op de n-GaN anode: (a) oxidatie van reductoren in de oplossing, (b) foto-corrosie van GaN, (c) oppervlakte recombinatie en (d) ladingsdrager recombinatie in de bulk. Alleen het eerste proces is wenselijk in de toepassing van foto-elektrolyse. Br^- werd als reducerend middel aan de oplossing toegevoegd, om foto-corrosie van het GaN te onderdrukken.

Verder werd het effect van nano-verruwing van de foto-anodes onderzocht. De GaN epilaag werd bewerkt tot nano-pilaren met behulp van droog etsen. De significante vergroting van het ruimteladingsgebied vergemakkelijkt de scheiding van ladingsdragers. Het fotostroom plateau wordt derhalve verhoogd met 84% ten opzichte van de vlakke GaN fotoanode. Plasma-geïnduceerde beschadiging van het oppervlak, ten gevolge van het droog ets proces, werd onderzocht door cyclische voltammetrie en impedantie spectroscopie. Beschadigingen van het oppervlak van de pilaren werd geminimaliseerd door optimalisatie van de procestechniek en nabehandeling met een chemische oplossing.

Ten slotte werd de invloed van de porositeit op de foto-elektrochemische eigenschappen van n-GaN onderzocht. De n-GaN epilaag werd poreus gemaakt aan de hand van een elektrochemische anodische ets. Anodisch etsen van n-GaN werd onderzocht met behulp van cyclische voltammetrie en chronoamperometry. In het poreuze GaN is het ruimteladingsgebied enorm vergroot en het neutrale ladingsgebied kleiner geworden ten op zichte van onbehandeld GaN; Recombinatie van ladingsdragers

aan het oppervlak en in de bulk wordt daarom onderdrukt. De plateau fotostromen voor poreus GaN, geëtst op 5.5-15.0 V, verhogen meer dan 400% ten opzichte van het onbehandelde GaN.

List of publications

Journal contributions

[1] W. J. Tseng, D. H. van Dorp, R. R. Lieten, P. M. Vereecken, and G. Borghs, "Porous n-GaN Photoanode Fabricated by Electrochemical Anodic Etching", *Journal of Physical Chemistry C* (submitted).

[2] W.-J. Tseng, D. H. van Dorp, R. R. Lieten, P. M. Vereecken, R. Langer, and G. Borghs, "The Impact of Plasma-Induced Surface Damage on Photoelectrochemical Properties of GaN Pillars Fabricated by Dry Etching", *Journal of Physical Chemistry C*, **118**, 11261 (2014).

[3] C.-Y. Su, R. Lieten, P. Bakalov, W.-J. Tseng, L. Dillemans, M. Menghini, T. Smets, J. W. Seo, and J.-P. Locquet, "Electrical Properties of Magnesium Oxide Layers with Different Surface Pretreatment on High Mobility $Ge_{1-x}Sn_x$ and Ge MOS Capacitors", *Applied Surface Science*, **291**, 31 (2014).

[4] W. J. Tseng, D. H. van Dorp, R. R. Lieten, B. Mehta, P. M. Vereecken, and G. Borghs, "Enhanced Photocatalytic Activity of Nanoroughened GaN by Dry Etching", *ECS Electrochemistry Letters*, **2**, 11 (2013).

[5] W. J. Tseng, B. Mehta, D. H. van Dorp, R. R. Lieten, P. M. Vereecken, and G. Borghs, "Enhanced Photoelectrochemical Activity of GaN by Dry Etching into Nanopillar Array", *ECS Transactions*, **53**, 29 (2013).

[6] R. R. Lieten, W. J. Tseng, K. M. Yu, W. van de Graaf, J. P. Locquet, J. Dekoster, and G. Borghs, "Single Crystalline $In_xGa_{1-x}N$ Layers on Germanium by Molecular Beam Epitaxy", *CrystEngComm*, **15**, 9121 (2013).

[7] W. J. Tseng, M. Gonzalez, L. Dillemans, K. Cheng, S. J. Jiang, P. M. Vereecken, G. Borghs, and R. R. Lieten, "Strain Relaxation in GaN Nanopillars", *Applied Physics Letters*, **101**, 253102 (2012).

Conference contributions

[1] W. J. Tseng, B. Mehta, D. H. van Dorp, R. R. Lieten, P. M. Vereecken, and G. Borghs, "Enhanced Photoelectrochemical Activity of GaN Pillar Photoanodes Fabricated by Dry Etching of Epilayer", *The Electrochemical Society (ECS) meeting*, Toronto, Canada, May 2013. (oral)

[2] R. R. Lieten, M. Paladugu, W.J. Tseng, J.-P. Locquet, and G. Borghs, "Improved Crystallinity of InGaN Layers by Mg Doping", *European Materials Research Society (EMRS)*, Strasbourg, France, May 2013. (poster)

[3] R. R. Lieten, W. J. Tseng, P. M. Vereecken, and G. Borghs, "III-Nitride Semiconductors for Photoelectrolysis", *Annual Meeting of Royal Dutch Chemical Society*, Delft, Netherlands, Nov. 2012. (invited)

[4] W. J. Tseng, L. Zhang, R. R. Lieten, P. M. Vereecken, and G. Borghs, "H_2 Generation by Solar Water Splitting using a Nanostructured GaN Electrode", *International Workshop on Nitride Semiconductors*, Sapporo, Japan, Oct. 2012. (poster)

[5] W. J. Tseng, L. Dillemans, M. Gonzalez, K. Cheng, G. Borghs, and R. R. Lieten, "Strain Relaxation and Distribution in GaN Nanopillars using In-plane X-ray Diffraction", *European Materials Research Society (EMRS)*, Strasbourg, France, May 2012. (oral)

[6] M. Gonzalez, K. Cheng, P. Tseng, and G. Borghs, "GaN Growth on Patterned Silicon Substrates: A Thermo Mechanical Study on Wafer Bow Reduction", *Thermal Mechanical and Multi-Physics Simulation and Experiments in Microelectronics and Microsystems*, Cascais, Portugal, April 2012. (oral)

[7] W. J. Tseng, M. Gonzalez, B. Sijmus, R. R. Lieten, K. Cheng, and G. Borghs, "Size-Dependent Strain Relaxation in GaN Nanopillars", *European Materials Research Society (EMRS)*, Nice, France, May 2011. (oral)

[8] R. R. Lieten, W.-J. Tseng, M. Leys, J.-P. Locquet, and J. Dekoster, "Indium Rich III-Nitrides on Germanium by Molecular Beam Epitaxy", *Materials Research Society (MRS)*, San Francisco CA, USA, April 2011 (oral)

List of abbreviations

Symbol	Description
AC	alternating current
AE	area enhancement
ALD	atomic layer deposition
aq	aqueous solution
CB	conduction band
CV	cyclic voltammetry
DC	direct current
EIS	electrochemical impedance spectroscopy
FWHM	full width at half maximum
GaN	gallium nitride
GIIXD	grazing incidence in-plane X-ray diffraction
HER	hydrogen evolution reaction
ICP	inductively coupled plasma
IHL	inner Helmholtz layer
InGaN	indium gallium nitride
IPA	isopropyl alcohol
LED	light-emitting diodes
MBE	molecular beam epitaxy
MOCVD	metal organic chemical vapor deposition
M-S	Mott-Schottky
n-GaN	n-type gallium nitride
OER	oxygen evolution reaction
OHL	outer Helmholtz layer
PECVD	plasma-enhanced chemical vapor deposition
p-GaN	p-type gallium nitride

Symbol	Description
PL	photoluminescence
PV	photovoltaic
RIE	reactive ion etching
SA	surface area
SCR	space-charge region
SHE	standard hydrogen electrode
UID	unintentionally doped
UV	ultraviolet
VB	valence band
XRD	X-ray diffraction

List of symbols

Symbol	Explanation	Unit
∅	diameter of pillars	nm
$\Delta U_{onset\text{-}plateau}$	potential difference between current onset and plateau	V
C_H	capacitance density of Helmholtz layer	F/cm^2
C_r	differential electrical capacitance	F/cm^2
$c_{red,s}$	surface concentration of reductant states	$1/cm^2$
C_{sc}	capacitance density of space charge region	F/cm^2
E_g	bandgap energy of semiconductors	eV
E_t	energetic position of surface traps	eV
j	current density	A/cm^2
j_a	partial anodic current density	$1/cm^2$
j_c	partial cathodic current density	$1/cm^2$
j_{ph}	photocurrent density	A/cm^2
$j_{pla,ph}$	plateau photocurrent density	A/cm^2
$j_{plateau}$	plateau current density	A/cm^2
n	doping concentration	$1/cm^3$
n_0	electron concentration of semiconductor bulk	$1/cm^3$
n_s	electron concentration at the surface of semiconductors	$1/cm^3$
p_0	hole concentration of semiconductor bulk	$1/cm^3$
p_s	hole concentration at the surface of semiconductors	$1/cm^3$
Q_H	charge density of Helmholtz layer	C/cm^2
Q_{sc}	charge density of space charge region	C/cm
quad	$= 1\times 10^{18}$ joules	
R	relaxation depth of stress	nm
R_{ct}	interfacial charge transfer resistance	Ω/cm^2
R_s	series resistance	Ω/cm^2
t	time	s
U	applied potential	V
U_C	conduction bandedge potential	V

Symbol	Explanation	Unit
U_{etch}	external bias during anodic etching	V
U_{fb}	flat-band potential	V
U_{H^+/H_2}	reduction potential of H^+/H_2	V
U_{H_2O/O_2}	reduction potential of H_2O/O_2	V
U_{ocp}	open circuit potential	V
U_{onset}	onset potential	V
$U_{plateau}$	plateau potential	V
U_{sc}	potential drop across space charge region	V
U_V	valance bandedge potential	V
$U_{WE\text{-}RE}$	potential difference between working electrode and reference electrode	V
ν	scan rate	mV/s
W_{sc}	width of space charge region	nm
χ^2	goodness of fit	
Z	electrical impedance	Ω/cm^2
Z'	real part of electrical impedance	Ω/cm^2
Z"	imaginary part of electrical impedance	Ω/cm^2
α	optical absorption coefficient	1/cm
α_c	critical angle of optical total reflection	°
α_i	incoming angle of light	°
ε	dielectric constant (= 8.854×10^{-12} F/m)	
ε_0	vacuum permittivity	F/m
$\eta_{solar\text{-}H2}$	solar-to-hydrogen conversion efficiency	%
λ	wavelength	nm
τ_{rad}	minority carrier lifetime for radiative recombination	s
τ_s	minority carrier lifetime for surface recombination	s
τ_{SRH}	minority carrier lifetime for Shockley-Read-Hall recombination	s

Table of contents

CHAPTER 1

Introduction

Chapter 1. Introduction

1.1 Motivation for renewable energy

Energy is a fundamental pillar to sustain civilization of human beings. Transportation, industrial production, economic activities and household activities are empowered by energy. Since the industrial era, the energy demand has been increasing tremendously, and undoubtedly even more energy will be required in the future. The energy need of the world is strongly linked to the world population. Figure 1.1(a) shows the history and prediction of world population, issued by the United Nations [1]. After the mid-20th century, the world population has been booming at an extremely fast path. Especially since 1970, the world population has been increasing 0.8 billion every decade in average. The world population in 2100 is predicted to vary between 6 and 16 billion, based on different fertility models. Although the population of developed countries (OECD members) saturates or even slightly declines over years, the strong population growth of developing countries (non-OECD members) primarily contributes to the population increase in the future decades.

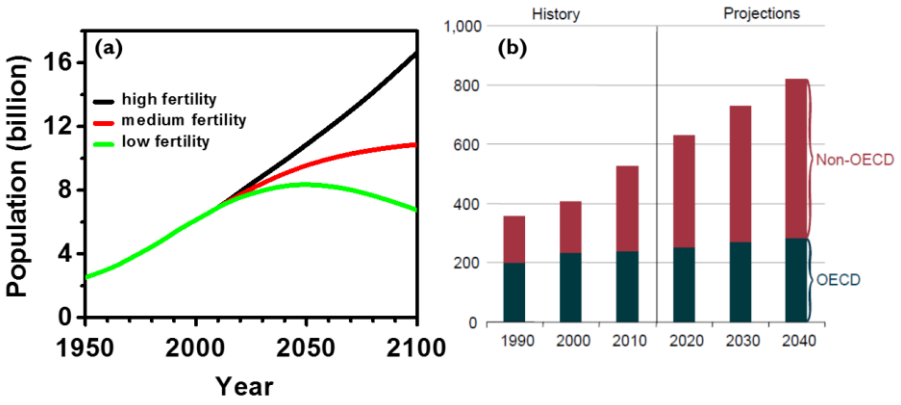

Figure 1.1: History and prediction of (a) world population [1] and (b) energy consumption (unit: quad = 1×10^{18} joules) [2].

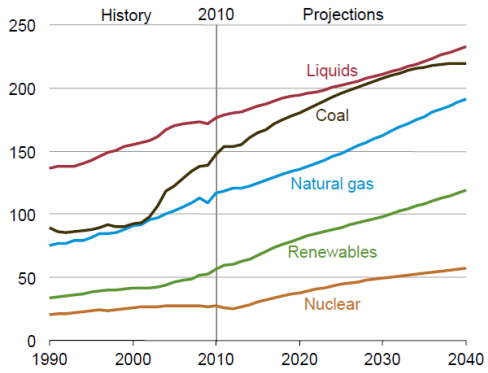

Figure 1.2: History and prediction of world energy consumption (unit: quad) [2]

The outlook of the energy consumption (Figure 1.1 (b)), issued by the Energy Information Administration (EIA), US, confirms the link between population and energy consumption [2]. The energy consumption is expected to increase in the coming decades at a speed of 10 quad (1 quad = 1×10^{18} joules) per year. Non-OECD members predominately contributes to the increase of the energy consumption.

As shown in Figure 1.2, fossil fuels including liquid fuels, coal and natural gas have been the main energy resource and will play an even more important role in the foreseeable future (almost 80% of world energy use through 2040). The energy conversion from fossil fuels is the most industrially developed; the production cost is significantly lower with respect to all the other energy sources. Industries, transportation and powering systems are designed on the platform of fossil energy. However, this energy source is not sustainable with expected resources that can last for 50-100 years.

Moreover, it is a common awareness that the emission of greenhouse gases has serious ecological and environmental impacts on the earth. The increased temperature of the atmosphere causes the rise of sea level, risking the residence at coastal areas and low lands. Most importantly, the following extreme weather (droughts, heats, rains, hurricanes, etc.) and the changes of the climate system (ocean currents, seasons, etc.) seriously endanger personal possessions, food supplies, water supplies and lives.

The electricity generation using nuclear technology could be a solution for carbon-free energy supply, and is used in many countries to some extent (Figure 1.2). However, the safety of nuclear power generation is always a concern. Several accidents in the history occurred because of system faults, unexpected natural disasters and operational error. These events resulted in environmental catastrophes and live casualties. The storage and the treatment of the radioactive waste are also a strong concern. The radioactive decay time of some waste can last over thousand years.

The development of renewable energy therefore plays an essential role in the sustainability of energy supply in the future. Table 1.1 shows the prediction of electricity generated from different renewable sources. Hydroelectric, wind and sunlight are the main renewable energy resources for the electricity; and will dominate the energy supply in the foreseeable future. The growth of renewable energy is the fastest among all energy sources (Figure 1.2), by an average of 2.8% per year. Although renewable energy only accounts for 17% of the electricity supply nowadays, it is expected to increases to 27% in 2040. To meet this growth, the decline of the energy cost per energy unit is essential so renewable energy can be more competitive to fossil energy. Therefore, the energy conversion efficiency needs to be improved from a technology point of view; the cost of manufacturing and maintenance should be further reduced; the laboratory researches and developments of emerging technologies should be introduced into the market.

Table 1.1: Prediction of electricity generated by different renewable energy sources (unit: billion kWh) [2]

	2015	2020	2025	2030	2035	2040	Growth (%)[a]
Hydropower	3805	4452	4762	5177	5692	6232	2.0
Wind	767	1136	1383	1544	1694	1839	5.8
Solar	157	240	288	327	394	452	4.1
Geothermal	112	133	146	171	195	220	9.1
Other	427	549	643	729	800	858	3.2
Total	5267	6509	7222	7948	8775	9601	2.8

[a]average energy growth per year

1.2 Hydrogen as chemical fuel

1.2.1 Storage of renewable energy

The storage of the harvested renewable energy is an essential issue. Currently, the energy of the renewable energy sources is predominately converted to electricity. Limited by its nature, renewable electricity can strongly fluctuate. Figure 1.3 (a) and (b) show the electricity output of the wind and solar energy in Germany in 2013, respectively. The wind source is strongly influenced by the regional or local weather. A sharp power peak can lead to more energy supply than the actual energy demand. The electricity output of photovoltaic (PV) is not only influenced by the local weather, but also by seasons. Moreover, PVs do not produce electricity during evenings. Many schemes have been proposed to assure the stability of electricity supply, such as supplementary electricity supply by conventional power stations, electricity trade to/from neighbor countries, electricity recycle using water pumping or batteries [3]. Nevertheless, the un-prediction and strong fluctuation of renewable energy sources seriously complicate the management of electricity supply; Energy loss often happen at peak seasons. Furthermore, unlike fossil fuel and nuclear power plants, the electricity output is not controllable to match the off-peak and on-peak hours.

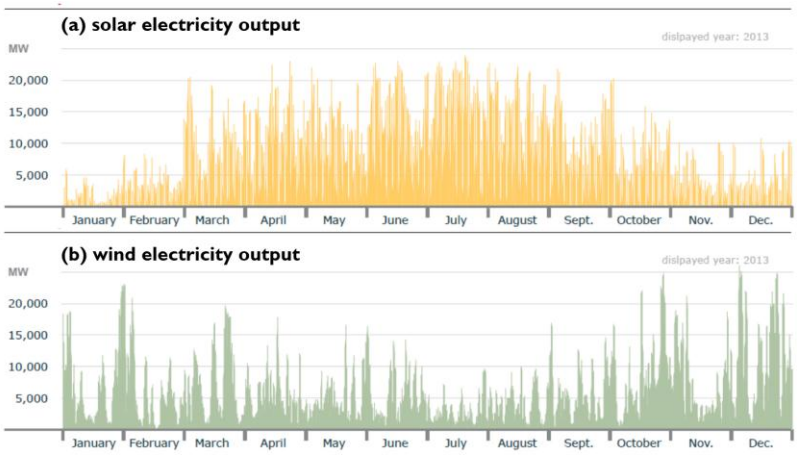

Figure 1.3: Renewable electricity generated by (a) solar and (b) winder energy in Germany in 2013 [6].

The conversion of energy to chemical bonds is an effective solution for this problem. The harvested energy is stored as liquid or gaseous substance in this scenario. At energy output peaks, these substances are abundantly generated and the oversupply can be stored in tanks, pipelines or underground. At peaks, the substances are released to meet supply deficiency.

Notably, the application of renewable energy strongly depends on the local climate, geography and altitude. The PV technology is more efficient at low altitude places due to higher light intensity and shorter seasonal change of light time. The wind sources are more abundant at the Westerlies and trade wind band. Locations for hydroelectric and geothermal energy are very specific. Therefore, long distance of energy transfer or international energy trade are expected to empower the area where energy production is less than energy demand in the future. In this case, the energy storage in the form of a substance is more advantageous than electricity transport. The substance energy loss during transport using pipelines or freight is much less than the electricity.

Hydrogen is a good candidate as the substantial energy carrier. First, the oxidation of hydrogen, which is described in Eq. (1.1), does not emit carbon:

$$H_2 + {}^1\!/_2\, O_2 \rightarrow H_2O \tag{1.1}$$

Water, as the product of this reaction, is harmless to the environment. Moreover, water which is also a resource for hydrogen production exists abundantly on earth.

Motive energy for vehicles, ships and aircrafts is a major energy consumption of the world. Liquid-based fossil fuels (mainly diesels and petroleum) are currently used to drive these vehicles. In the future, to offer momentum will be an important application for hydrogen technology [4]. Motive power can be provided by burning of hydrogen in an internal combustion engine or turbine, or by the electricity transformed from a fuel cell. Taking the advantage of its high energy density (wt. %), with the advancement of storage development [5], motive vehicles with higher energy capacity is expected.

Electricity will be still a power platform for electronic appliances and industrial production. The hydrogen energy can be transformed to electricity using a fuel cell. The

developments of different fuel cell systems are reviewed in Ref [7]-[9]. According to different needs, the electricity can be transformed in a centralized hydrogen power station, and then is distributed to a neighborhood and city. Alternatively, the electricity can also be only transformed at the user side.

1.2.2 Strategies for renewable hydrogen generation

Hydrogen can be generated directly or indirectly using solar energy. Figure 1.4 shows different schemes for renewable hydrogen production [10]. For example, water can be decomposed through a series of thermochemical reactions for hydrogen generation. The direct thermolysis of water only take place at a temperature higher than 2500K [11]. Since 1960s, numerous different chemical reactions have been studied in order to lower the required reaction temperature [12]. Multistep chemical reactions and different catalysts are usually involved in the process. The thermochemical water decomposition process is currently possible for temperatures higher than 1000K [10], and therefore is possible to be driven by a concentrated solar system.

Hydrogen can also be obtained from biomass. Although generation of hydrogen through biomass accompanies carbon-based byproduct (i.e. CO_2 and Ethanol), it is a carbon-neutral renewable scheme which does not increase the concentration of CO_2 in

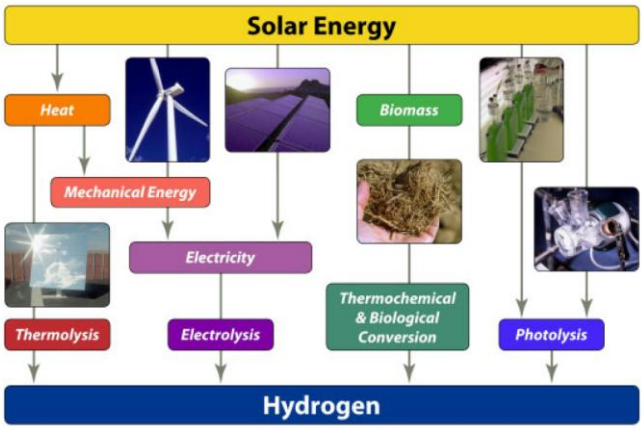

Figure 1.4: Schemes for renewable hydrogen generation [10]

the atmosphere. Corps or agricultural residuals containing rich lignocellulose are primarily the biomass resources [13]. Gasification and pyrolysis are two mainstreams for the biomass-hydrogen production [14]. The main technical challenges for biomass-hydrogen conversion include the impact of the composition variation of the biomass on the production and catalyst development for gas condition [15].

Hydrogen production through photosynthetic microorganisms is a promising alternative [16]. The light absorption efficiency of microorganisms (i.e. green algae, Cyanobacteria) can be over 40 % [17]. The theoretical solar-hydrogen conversion efficiency is therefore around 10-13%. The microorganisms absorb light and generate protons and electrons. With photosynthetically-generated reductants, hydrogenase enzymes convert protons to hydrogen. Currently, this approach is still at the stage of research and development. The control and engineering of photosynthetic electron transport pathways is a crucial barrier limiting the hydrogen conversion efficiency [18].

Hydrogen production by electrolysis is the most industrially-developed approach with respect to other renewable approaches, and is an approach with large capacity of hydrogen production. The electrolyzer can be driven by renewable electricity and performs water decomposition electrochemically. After gas collection and vapor removal, ultra-pure hydrogen is attainable. Water electrolysis with an efficiency of 50-80% is generally achievable, depending on the production scale and the electrolysis technology [22].

However, in the scheme of "renewable electricity + electrolysis", the electricity is first generated using renewable sources, and is then distributed in the electricity grid. Energy losses at energy transformations and during transmission are inevitable. Taking "PV+ electrolysis" as an example, the energy conversion efficiency is 12-18% for a silicon PV module [19]. For a PV power station, the generated direct current (DC) is collected and is inverted to alternating current (AC) before the electricity output with an energy loss of 5~10% [20]. The electric voltage is increased by a substation or transformer to reduce electricity loss during transmission and distribution. The high electric voltage is then stepped down when the electricity is distributed at the electrolyzer side. The energy loss from the power station to the electrolyzer port is typically 8-15% [21]. The AC power needs to be inverted to DC for electrolysis again when it is used.

Direct water photoelectrolysis is an alternative for renewable hydrogen production. The solar energy is absorbed by a semiconductor, and is directly used to electrolyze water in the same system. In this scenario, the energy loss due to multiple energy transformations and energy transmission can be avoided. Furthermore, the structural simplicity of the photoelectrochemical cell is one of major benefits. In contrast to the PV system, the extra module design including grid connection, electricity invertor as well as the metal contacts for current extraction are not needed [22].

1.3 Solar water splitting for hydrogen generation

Under light illumination, a semiconductor absorbs photons whose energy is higher than the bandgap. Bounded electrons in the valence band (VB) are photoexcited to the conduction band (CB), forming free electrons and free holes. After charge separation, electrons and holes migrate to the electrode surface. Electrons at the CB transfer to the solution for water reduction; holes at the VB transfer for water oxidation. The overall water splitting process is expressed by

$$H_2O \rightarrow \frac{1}{2} O_2 + H_2; \qquad \Delta G^\circ = +237 \text{ kJ/mol} \qquad (1.2)$$

Eq. (1.2) is an uphill process, requiring a standard Gibbs free energy change (ΔG°) of 237 kJ/mol (or ΔE = 1.23 eV).

1.3.1 Photoelectrolysis systems

Two photoelectrolysis systems can be classified: photocatalytic water splitting and photoelectrochemical water splitting [23],[24].

In the case of the photocatalytic water splitting (see Figure 1.5 (a)), electrons and holes are photo-generated in the semiconductor and perform water redox reaction at the surface of the semiconductor. Generally speaking, the photocatalytic system has advantages of low cost for the production and the simplicity of the cell design. The photocatalysts are usually in the form of nanoparticles, and are synthesized using chemical approaches [24]. The substrate for the photocatalyst is not always needed. Oxygen and hydrogen are

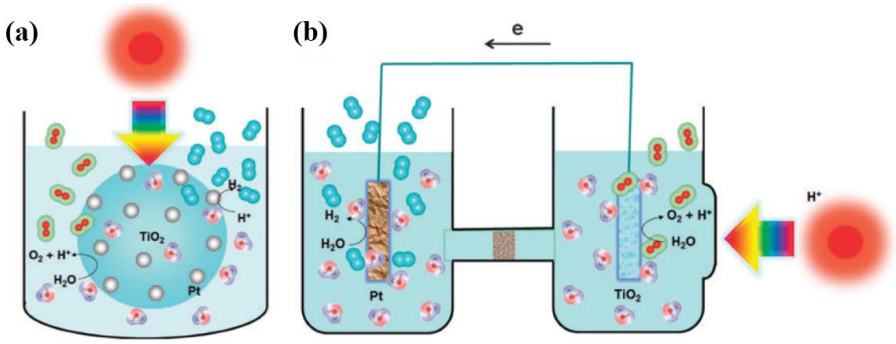

Figure 1.5: Solar water splitting in (a) a photocatalytic system and (b) a photoelectrochemical system using TiO_2 semiconductors as examples [27].

produced in the same cell. The suppression of carrier recombination is a major challenge. The loading of catalyst to facilitate the charge transfer can effectively enhance the conversion efficiency [25]. The nanostructuring of photocatalysts has a significant success in the suppression of carrier recombination [26].

In the photoelectrochemical water splitting system (see Figure 1.5 (b)), after photoexcitation, minority photocarriers are drifted to the interface by the electric field of the depletion region, and perform redox reaction at the photoelectrode surface. Majority carriers are extracted out to an external circuit, and perform redox reaction at the other electrode. Oxygen and hydrogen are therefore generated and collected at different electrodes. After removal of vapor, pure hydrogen is obtained. Additional gas separation is not needed in contrast to the first system. Since current extraction is necessary in this scenario, a substrate or template is always required. More deposition choices are possible to deposit or grow the material on a substrate such as spin coating, spray pyrolysis, colloidal growth, molecular beam epitaxy and chemical vapor deposition, etc [28],[29]. Similar to the photocatalytic system, carrier recombination is also one of the main technical barriers. Both catalyst loading and nanostructuring improve significantly the conversion efficiency [30].

1.3.2 Energy requirements for self-driven photoelectrolysis

Photoelectrodes which are able to perform photoelectrolysis without external energy input is desirable. The efficiency loss when requiring an energy input can be avoided. The external electric connection is not needed and the system design can be further simplified. In order to perform the redox reaction simultaneously, photo-electrons should have higher energy than hydrogen formation energy, and photo-holes should have lower energy than the oxygen formation energy.

Consequently, two energy criteria should be fulfilled, illustrated in Figure 1.6. First, the bandgap of semiconductors should be larger than 1.23 eV (see Eq. (1.2)). Notably, additional energies are required to overcome the energy barrier of OER and HER, and to improve the kinetics [31]. Consequently, the ideal bandgap of a semiconductor is around 1.8-2.0 eV [23],[24]. Secondly, the CB edge potential and VB edge potential should sandwich the water redox potentials. The CB edge should be more negative than the hydrogen formation potential (0 V *vs*. standard hydrogen electrode (SHE) at the standard condition); the VB edge should be more negative than the oxygen formation potential (-1.23 V *vs.* SHE at standard condition).

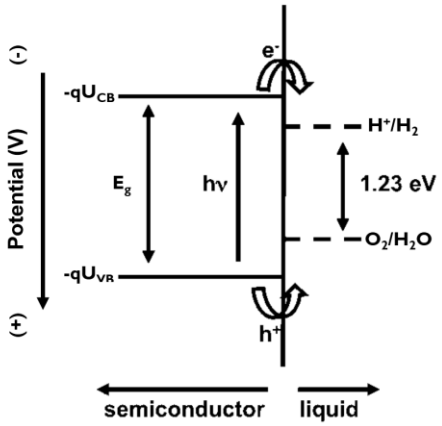

Figure 1.6: Energy requirements between a semiconductor and water redox energy levels for a self-driven photoelectrolysis system. [23]

The light absorption of semiconductor photoelectrodes has a similar concept as conventional PVs. The light absorbers harvest light and generate photocarriers. A semiconductor photoelectrode using a single material is widely used for water photoelectrolysis. This simple structure simplifies material characterization and benefits material optimization such as bandgap engineering, defect mitigation and bandedge manipulation. The bandgap of the material determines which part of solar spectrum can be utilized. The photons with energy higher than the bandgap are absorbed, and unabsorbed light is wasted. Different from photovoltaics whose conversion efficiency is determined by both output potential and current, the energy conversion efficiency of a photoelectrode is only determined by the rate of hydrogen generation. The solar-to-hydrogen efficiency is independent of the photon energy as long as the photons can be absorbed and photocarriers can electrolyze water. The main drawback of this type of photocatalysts is the weak carrier separation. The only electric field which can separate photocarriers exists at the semiconductor/solution interface.

By depositing or growing a different semiconductor material on the host semiconductor, a heterostructure is formed. The major benefit of this structure is the introduction of a heterojunction inside the photoelectrode. An additional electric field in the bulk is therefore available for carrier separation. For materials with short carrier diffusion length such as metal oxides [32]-[34], the energy conversion efficiency can be significantly improved when such a heterostructure is formed. This structure is also widely used for materials whose absorption coefficient is low, such as indirect bandgap materials [35]-[37]. In these materials, photocarriers can be generated far from the surface due to the limited light absorption efficiency. It is almost impossible for photocarriers to reach the interface if there is no additional electric field for charge separation in the bulk of the photoelectrode.

1.3.3 Semiconductors for water photoelectrolysis

Since 1970s, Fujishima and Honda demonstrated direct photoelectrolysis using a TiO_2 photoanode [38], photoelectrochemical properties of many semiconductor materials have been investigated extensively [39]-[41]. Figure 1.7 shows chemical elements which are

involved in the construction or functionalization of photoelectrodes [42]. Metal oxides, sulfides and nitrides are common materials for photoelectrodes. The metal cations typically have an electronic configuration of d0 or d10. Generally speaking, the CB of these photoelectrodes are composed by the d or sp orbitals of the metals. The VB are typically formed by the 3p orbital of sulfur, the 2p orbital of nitrogen or the 2p orbital of oxide.

For perovskite photoelectrodes, metals of group 1 and group 2 are often present in the crystal structure although they do not have a direct impact on the energy structure of photoelectrodes. Some transition metal cations like Cr^{3+}, Ni^{2+} and Rh^{3+} can be introduced into the photoelectrodes in some cases as impurity for defect-assisted light absorption. Some noble metals (Pt and Au) or metal oxide (NiO, RuO_2 and IrO_2) have a strong catalytic property for the oxygen evolution reaction (OER) or hydrogen evolution reaction (HER). Therefore, they are often loaded as catalyst to improve the charge transfer efficiency.

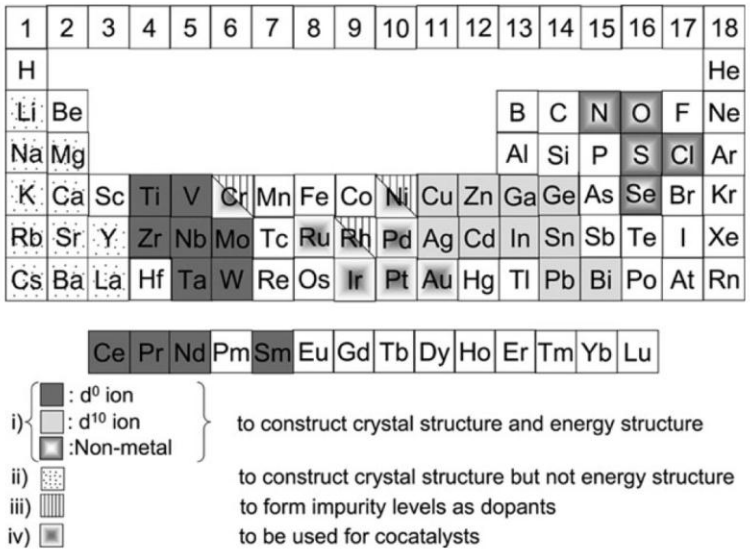

Figure 1.7: Elements which are used to construct or functionalize photocatalyzers [42].

Figure 1.8 presents the band alignments of some photoelectrodes to water redox potential at pH 0 [43],[44]. The potentials for HER and OER are 0 V and 1.23 V, respectively. Generally speaking, the VB edge of metal oxide semiconductors lays ~+3 V with respect to the NHE as a result of the potential of O 3p orbital. Semiconductors whose CB edge and VB edge sandwich the water redox potentials can photoelectrolyze water simultaneously without any external energy input. The semiconductors, which cannot meet the energy criteria, can still be used for self-driven photoelectrolysis once the heterostructure is formed with a material with proper bandgap (i.e. Si + WO_3 or Si + Fe_2O_3).

The bandgap of a photoelectrode determines the theoretical limit of the energy conversion efficiency. Figure 1.9 shows the solar spectrum and the theoretical limit of solar-to-hydrogen energy conversion. In assumption that the light absorption and water electrolysis efficiency are 100% and there is no carrier recombination (two photons lead to the formation of one hydrogen molecule), the theoretical maximum limit of the solar-hydrogen conversion efficiency can be calculated as a function of wavelength (λ). For a material which can only absorb UV light (< 400 nm), the maximum conversion efficiency is only ~2 %. However, if light with λ < 400 nm can be absorbed, the maximum

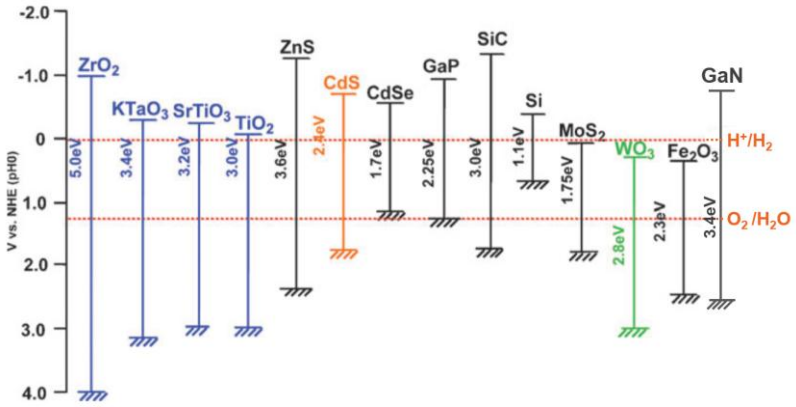

Figure 1.8: Conduction band (CB) edges and valence band (VB) edges of semiconductors with hydrogen and oxygen formation potentials as reference at pH = 0, adapted from [43] and [44].

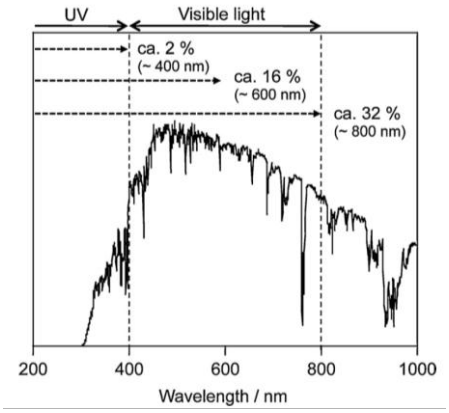

Figure 1.9: Solar spectrum with maximum energy conversion efficiencies of water photoelectrolysis, which are calculated under the assumption that light absorption efficiency and electrolysis efficiency are 100% [44].

conversion can be enhanced to ~ 16%. If the bandgap of a material can be further reduced to harvest light < 800 nm, the efficiency can be further extended to ~ 32% [45].

Consequently, different approaches have been proposed to engineer the bandgap of semiconductors. A common strategy is to introduce elements into a conventional photoelectrode to form an impurity level [46],[47]. Therefore light with energy shorter than the bandgap can be absorbed by donor level-CB transitions or VB-acceptor level transitions. (i.e. doped TiO_2 [47] and $SrTiO_3$ [48])

For most of metal oxide photoelectrodes, the VB edge potential is more positive (~3 V *vs.* NHE) due to the ionization potential of the O 3p orbital. Consequently, the bandgap of metal oxides is generally large. The orbital potential of N 2p is more negative than O 3p. For some metal oxides, the bandgap can be engineered after nitride incorporation. After the compound formation, the photoelectrode possesses a new VB edge potential, which is formed by the hybridization of the O 3p and N 2p orbital, and is less positive. Few successful examples to reduce the bandgap using this strategy are TaON [49] and $LaTiO_2N$ [50]

Another approach to reduce the bandgap is by the repulsion of orbitals at similar potential levels. The most successful example is the compound formation of GaN and

ZnO. GaN and ZnO both have a Wurtzite structure and have a similar bandgap (GaN: 3.4 eV and ZnO: 3.3 eV). After compound formation, the repulsion between N 2p and Zn 3d orbitals pushes the VB edge potential more negative. For $(Ga_{0.87}Zn_{0.13})(N_{0.87}O_{0.13})$, a bandgap of 2.58 eV is experimentally demonstrated [51],[52].

1.3.4 Photostability of semiconductors

Photostability is a general challenge for photoelectrodes, but is particularly a serious issue for n-type non-oxide-based semiconductors. At the n-type semiconductor/solution interface, the CB and VB bend downward. Photo-holes are drifted to the photoelectrode surface and oxidize water. Often, photo-holes not only oxidize water but also oxidize the photoelectrode.

Depending on the thermodynamic stability of the oxidized product in the solution, the oxidized product can either dissolve into solution, leading to a corrosion process, or the surface can be passivated if the oxidized specie is less soluble. In the first case, a short device lifetime is expected, since the hydrogen production is at the cost of material loss. In the second case, the conversion efficiency can drop significantly. The photoelectrode and solution are electrically isolated by the passivated layer and photocarriers mainly recombine.

Photo-holes at the surface of n-type photoelectrodes participate in one of the following activities: carrier recombination, interfacial charge transfer and photo-corrosion of material. Therefore, the kinetics of interfacial charge transfer can play an important role in the photostability of semiconductors. When the charge transfer is promoted, the photo-corrosion rate of the photoelectrode is reduced. The charge transfer kinetics can be enhanced using different sacrificial reducing agents such as Cl^- [53], S^{2-}/SO_3^{2-} [54], Fe^{2+} [55], ethanol [56], etc. It is important to note that in this case photo-holes oxidize the reducing agents instead of water at the photoelectrode surface.

Water oxidation is typically slow at the photoelectrode surface. Four photo-holes and two water molecules are required to generate an oxygen molecule; the formation of oxygen molecules takes several intermediate states. Therefore, a large overpotential and

slow kinetics for the OER are typically observed for a pristine photoelectrode. Unfortunately, the material can be seriously corroded when photo-holes are not transferred fast enough to the solution. Loading of catalysts at the photoelectrode surface is often used to improve the catalytic properties [57],[58]. Different intermediate steps with lower energy barrier for the OER can be constructed with the help of catalysts. Consequently, the corrosion of photoelectrodes could be suppressed when the charge transfer is more favorable. RuO_2, IrO_2 and Pt are the most common catalysts for the OER due to the high catalytic activity [59]-[61]. Because of the low cost and abundance in earth, NiO and Fe_3O_4 are also common used as catalysts for photoelectrodes [62],[63].

The deposition of a robust layer at the photoelectrode surface is an alternative solution against photo-corrosion. The basic idea is to isolate the material of poor photostability from a direct contact with solution using another material which has good photostability. Recently, the deposition of the protection layer using atomic layer deposition (ALD) has attracted many attentions [64]-[66]. Due to the high deposition conformity, a thin protection layer (< 5 nm) is sufficient to fully cover the nanostructure surface. TiO_2 is a commonly used as the protection layer due to its high photostability. After the deposition of the TiO_2 protection layer on the photoelectrode, the device lifetime has shown significantly improvement [67]-[69]. It is important to note that the band alignment of the photoelectrode and protection layer needs to be considered in the design. For the n-type photoelectrode, when the VB edge is more negative than that of the protection layer, the photocurrent is blocked and the conversion efficiency is sacrificed [70].

1.4 InGaN photoelectrodes

1.4.1 Motivation for InGaN

As described earlier, metal oxides generally have a large bandgap due to the positive VB edge potential. In contrast, since the ionization potential of the N 2p orbital is smaller than the O 3p orbital, the VB edge of metal nitrides can be less positive. Therefore, III-Nitride semiconductors with a smaller bandgap than metal oxides are possible. The bandgap of InN and GaN are 0.7 eV [76] and 3.4 eV [77], respectively. Although the

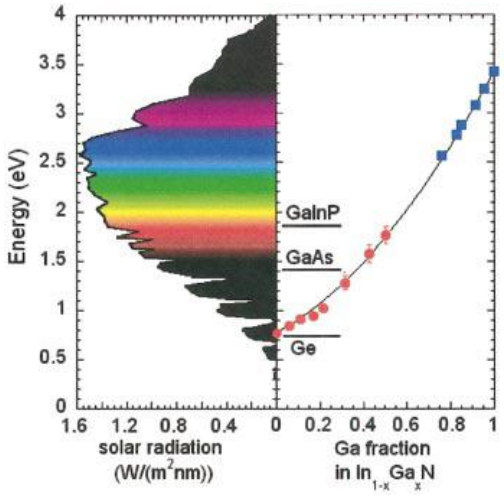

Figure 1.10: Bandgap of $In_{1-x}Ga_xN$ as a function of Ga composition [82].

bandgap of GaN is high, after indium incorporation the bandgap can be reduced. The bandgap of InGaN semiconductors is direct and, depending on the elemental composition, can be tuned from Infrared to UV (0.7-3.4 eV). These material properties enable InGaN to be widely used in different optoelectronic applications such as light-emitting diodes [78], lasers [79], photovoltaic [80] and light sensors [81].

A small bandgap is in favor for light absorption, but the kinetics of the redox reaction can be sluggish when the overpotential is small. To balance the utilization of the solar spectrum and the overpotential of water electrolysis, a semiconductor with a bandgap of 1.8-2.0 eV is desirable [23],[24]. Figure 1.10 shows the bandgap of $In_xGa_{1-x}N$ compounds with different indium composition. $In_xGa_{1-x}N$ with x = 0.4-0.5 have been experimentally demonstrated and show a bandgap of 1.6-1.8 eV [83].

Moreover, due to the large absorption coefficient of III-Nitride semiconductors (10^5 cm^{-1} for GaN and 6×10^4 cm^{-1} for InN [84]), an InGaN film less than 200 nm can absorb most of the supra-bandgap light. Therefore, the material consumption in the photoelectrode growth can be reduced. From another point of view, most photocarriers are generated near the surface region and therefore have a higher chance to reach the interface before carrier recombination occurs.

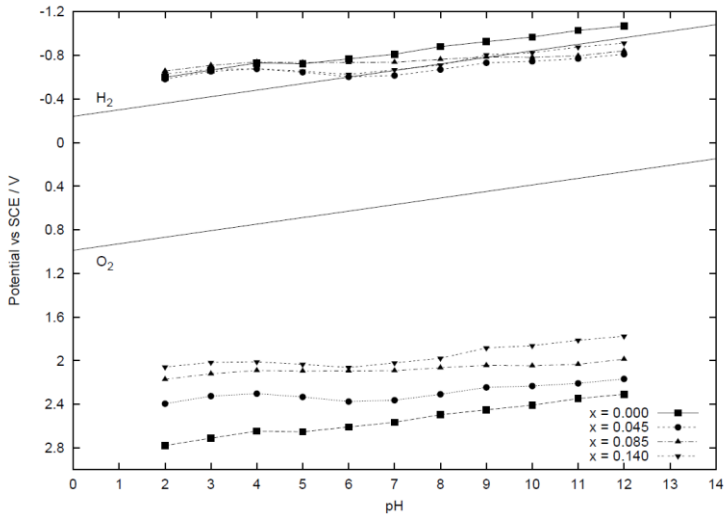

Figure 1.11: CB edge and VB edge potentials of n-type $In_xGa_{1-x}N$ semiconductors as a function of pH [85].

Using density functional theory, Moses et al. calculated the bandgap and band alignment of InGaN as a function of indium composition. The VB edge potential is predicted to decrease linearly with the indium composition. $In_xGa_{1-x}N$ with x up to 50% can still satisfy the energy criteria for the self-driven water photoelectrolysis. Beach et al. measured the CB edge and VB edge of $In_xGa_{1-x}N$ at different pHs [85]. As shown in Figure 1.11, the CB edges of InGaN are less dependent of the indium composition, and the VB edges shift toward negative as the indium composition increases. The CB edge and VB edge of the $In_{0.14}Ga_{0.86}N$ can still sandwich the water redox potentials for pH < 4.

1.4.2 GaN epitaxy

$In_xGa_{1-x}N$ epilayers, for many reasons, are commonly grown on a GaN template. Firstly, GaN and InGaN are both III-Nitride materials and have relatively similar material properties. From the perspective of material growth, the epitaxy of a ternary compound is more complex than that of a binary compound. The epitaxy engineering is easier when the template of the binary compound (GaN) is first developed. Secondly, the crystalline quality and defect density of the template have a strong influence on the quality of the

succeeding epilayer. Thanks to the material development for optoelectronic and power devices, the epitaxial growth of GaN has been well established. High-quality GaN templates with low surface defect density are currently available [86]. Furthermore, the cost of the GaN templates has been tremendously reduced these years following the maturity of GaN epitaxy on Si substrates and the scaling up of the wafer size. Therefore, the production cost of InGaN epilayers can be lower using GaN templates.

Due to the technical difficulty to produce native nitride substrates [71], GaN is predominately grown on a foreign substrate. The most common substrates are Si, sapphire and SiC. Each substrate has its own advantages and disadvantages for GaN epitaxy. The reviews of GaN epitaxy on these substrates are referred to Ref. [71]-[74]. GaN on Si becomes the mainstream of industrial production, predominantly driven by the low cost of Si substrates. The wafer cost of Si is approximately 10% of sapphire or 1% of SiC for the equivalent size [87]. The availability of scaling up and the potential for the system integration to current silicon technology are also in favor of GaN epitaxy using Si substrates. Currently, 8-inch GaN on Si is commercially available and 12-inch Si wafers are commonly used in the CMOS production.

Different issues needs to be overcome for GaN epitaxy on Si. Stress management is a primary challenge. The atomic lattice of GaN is smaller than Si by 17%, resulting in a considerable tensile stress. Moreover, the thermal expansion coefficient of GaN and Si are 5.59×10^{-6}/°C and 2.59×10^{-6}/°C, respectively [72]. The distinct difference in the thermal expansion coefficient (116%) contributes to a large thermal tensile stress after the epilayer is cooled down from the growth temperature (> 1000 °C). The tensile stress leads to severe wafer bowing or the formation of cracks as a result of stress relaxation. The buffer layer therefore plays a crucial role in the stress engineering. For GaN/Si, the buffer layer typically consists of an AlN nucleation layer and multiple $Al_xGa_{1-x}N$ intermediate layers. The nucleation layer introduces surface roughness for a primary stress relaxation, and serves as a wetting layer for the growth of the succeeding layers. The step-graded $Al_xGa_{1-x}N$ intermediate layers introduce additional compressive stress which compensates the large thermal tensile stress between GaN and Si. After proper

stress engineering by optimizing the composition, thickness and number of $Al_xGa_{1-x}N$ intermediate layers, the critical thickness of the GaN layer can be well extended.

The GaN epilayer is notorious for defect richness [74],[89],[90]: point defects include vacancies, interstitials and impurities; extended defects include misfits and threading dislocations; other defects are like cracks, pits, etc. Among all the defects, the dislocations are particularly detrimental for (opto)electrical devices, resulting in issues such as leakage current, breakdown and carrier recombination [91]. The threading dislocations, which originate from the nucleation layer, can grow all the way up to the surface. The AlGaN intermediate layers have been widely used to reduce the dislocation density. The threading dislocations terminate or bend at the interfaces of the AlGaN intermediate layers, triggered by the change of interfacial stress [92]. After using 3-4 layers of AlGaN intermediate layers, the threading dislocations reaching the surface can be typically reduced to $1\text{-}3\times10^9$ cm^{-2} [93],[94]. The dislocation density at the surface can be further reduced to the order of 10^8 cm^{-2} by the insertion of a SiN_x interlayer (see Figure 1.12) [86]. A selective epitaxial overgrowth of GaN on a SiO_2 patterned GaN template also successfully demonstrates GaN with low surface dislocation density [95],[96].

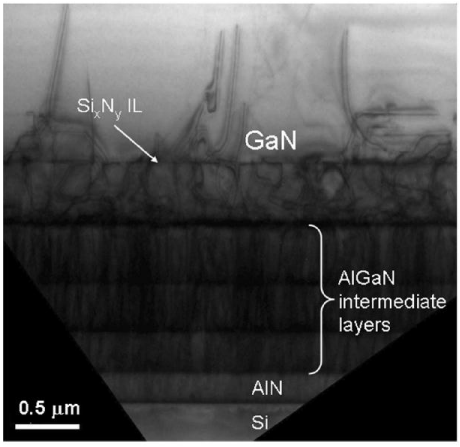

Figure 1.12: A TEM image of GaN epilayer taken under the $(11\bar{2}0)$ two-beam diffraction condition [86].

1.5 Motivation and objectives of the work

To empower our daily activities using clean, renewable energy has been an important focus of scientific research considering the ecological impact to the environment and the continuity of our society. Hydrogen is a promising energy carrier to replace fossil fuel due to its abundance of resource and ecology friendliness. To become cost competitive to fossil-based fuels, the production cost of hydrogen should be lower than $3 per kg by 2015, as stated in the roadmap of the Department of Energy in the United States [97]. Among various schemes of renewable hydrogen generation, direct water photoelectrolysis using semiconductor electrodes has drawn much attention. In this approach, energy loss due to multiple stage energy transformation and energy transmission can be avoided, leading to a higher theoretical solar-to-hydrogen conversion efficiency ($\eta_{solar\text{-}H2}$). Furthermore, the structural simplicity of the photoelectrolysis cell is a major benefit. In contrast to the "PV + water electrolysis" system, extra module designs such as metal contact and the external circuit connection are not needed, and the cost of water electrolyzer can be further reduced.

In the scheme of "PV + water electrolysis", an $\eta_{solar\text{-}H2}$ of ~10% is expected. Solar-to-electricity conversion efficiency ($\eta_{solar\text{-}electricity}$) is typically 12%-18% for commercial silicon PV modules [19]. Water electrolysis with an efficiency ($\eta_{electricity\text{-}H2}$) of 50%-80% is generally achievable, depending on production scale and electrolysis technology [22]. Taking $\eta_{solar\text{-}electricity}$ = 15% and $\eta_{electricity\text{-}H2}$ = 67%, an $\eta_{solar\text{-}H2}$ of ~10% is then expected using this scheme. To give a general idea of the current density output, let us assume that the output voltage is 0.6 V and the output current density is 25 mA/cm^2 under 1 sunlight for a Si PV with $\eta_{solar\text{-}electricity}$ = 15%. Because three PVs in series are required to give an output voltage of 1.8 V for water electrolysis, the current density of this PV system is ~ 8.3 mA/cm^2 (the same output current but for three times the area). To become more efficient than the "PV + water electrolysis" system, at least $\eta_{solar\text{-}H2}$ of 10% is needed for the direct water photoelectrolysis system. This means that a photocurrent of at least 8 mA/cm^2 is required under 1 sunlight (100 mW/cm^2).

For metal oxide-based photoelectrodes, an $\eta_{solar\text{-}H2}$ of 8.3 % has been demonstrated using TiO_2 photoanodes [98]; an $\eta_{solar\text{-}H2}$ of 4.5 % has been demonstrated using WO_3 photoanodes [99]; an $\eta_{solar\text{-}H2}$ of 3.5 % has been demonstrated using Fe_2O_3 photoanodes [28]. Strong carrier recombination and slow carrier mobility of metal oxides shorten minority carrier diffusion length, limiting the conversion efficiency. In contrast, $\eta_{solar\text{-}H2}$ of 12% has been demonstrated using III-V semiconductor heterojunction stacks as photoanodes, taking advantage of the long carrier diffusion length [100]. However, high production cost of the photoanodes is a disadvantage.

$In_xGa_{1-x}N$ semiconductors have drawn much attention in water photoelectrolysis for hydrogen generation [106]-[113]. The bandgap of $In_xGa_{1-x}N$, based on the elemental composition, can be tuned from 0.7 eV to 3.4 eV (Figure 1.10) [82]. The band positions of InGaN have been experimentally shown to sandwich the water redox potentials [85] (Figure 1.11). Since the maturity of GaN epitaxy on Si substrates, the cost of InGaN, which is grown on GaN templates, can be cheaper than the As-based and P-based III-V semiconductors. However, the growth of InGaN is still under development. Due to the difference of material properties between InN and GaN (i.e. growth temperature, vapor pressure, lattice constant, etc.), indium-rich InGaN semiconductors typically suffer from high defect density, indium segregation and high intrinsic carrier concentration [106]-[110] (see Section 7.1).

In contrast to $In_xGa_{1-x}N$, element segregation of GaN can be avoided and carrier concentration of GaN can be well controlled. Using intermediate buffer layers with proper stress engineering, the dislocation density at the surface of GaN can be controlled in the range of $1\text{-}3\times10^9$ cm^{-2} [94],[95] (see Section 1.4.12). Moreover, the long minority carrier diffusion length (200-300 nm [114]) and high absorption coefficient (10^5 cm^{-1} [84]) of n-GaN lead to the incident photon-to-carrier efficiency ~40% for supra-bandgap light [113]. In this dissertation we use n-GaN as a model system to investigate the photoelectrochemical properties of III-Nitride semiconductors.

State of the art

For planar n-GaN, the up-to-date highest photon-to-hydrogen conversion efficiency is only 0.61% under the illumination of Xe lamp (projected light intensity: 100 mW/cm^2). However, photons whose energy > 3.4 eV (bandgap of GaN) accounts for ~4% of photon quantity in the Xe lamp spectrum. The major limitation of the conversion efficiency is carrier recombination. For planar n-GaN, due to the thin SCR, photo-carriers are not efficiently separated (see Figure 4.5) and carrier recombination is severe.

Surface nanostructuring is an effective approach to suppress carrier recombination at the surface and in the bulk [23],[24], and therefore improves the conversion efficiency of n-GaN. Mostly, GaN nanostructures are prepared using bottom-up approaches (i.e. molecular beam epitaxy, selective growth, etc.) [105]-[113]. The photoelectrochemical properties of the bottom-up nanostructured GaN are summarized in Section 8.2.

However, GaN grown on a planar Si substrate by MOCVD is the most industrially mature approach to produce large-scale and cost-competitive GaN layers. Nanostructuring of the planar GaN epilayer is therefore an attractive strategy to achieve cheaper and more efficient photoanodes. However, the photoelectrochemical properties of nanostructured GaN by top-down techniques are seldom investigated [115]-[117].

Benton et al. [115] roughened the epilayer of a light-emitting diode (p-GaN/(In)GaN quantum wells/n-GaN) by dry etching into a nanopillar array. The effective area is enhanced by a factor of 4. Basilio et al. [116] used a two-step etching to roughen an n-GaN (0001) epilayer. The n-GaN was etched photoelectrochemically in 12 M NaOH solution to introduce surface defect sites, followed by a crystallographic etch at these defect sites using $H_3PO_{4(aq)}$ (wt. 85%) at 200 °C. The plateau photocurrent increased by 100% after the two-step etching with respect to the pristine GaN. Ryu et al. [117] used anodic etching to porosify an n-GaN epilayer in a 0.3 M oxalic acid solution. The plateau photocurrent of the GaN photoanode is increased over a factor of 2 after porosification.

In this dissertation, motivated by the advantages of top-down nanoroughening of GaN epilayers and the lack of relative photoelectrochemical studies, we applied different etching approaches to nanorough planar GaN epilayer grown by MOCVD. Therefore,

carrier recombination can be suppressed in the GaN nanostructures, resulting in a higher conversion efficiency.

1.6 References

[1] United Nations, world population prospects: the 2012 revision. http://esa.un.org/wpp/Excel-Data/population.htm

[2] U. S. Energy Information Administration, International Energy Outlook 2013. http://www.eia.gov/forecasts/ieo/pdf/0484(2013).pdf

[3] S. Pacala and R. Socolow, *Science*, **305**, 968 (2004).

[4] G. W. Huber, S. Iborra, and A. Corma, *Chem. Rev.*, **106**, 4044 (2006).

[5] L. Schlapbach and A. Zuttel, *Nature*, **414**, 353 (2001).

[6] Fraunhofer Institute, Electricity production from solar and wind in Germany in 2013. http://www.ise.fraunhofer.de/en/downloads-englisch/pdf-files-englisch/news/electricity-production-from-solar-and-wind-in-germany-in-2013.pdf.

[7] X. Cheng, Z. Shi, N. Glass, L. Zhang, J. Zhang, D. Song, Z.-S. Liu, H. Wang, and J. Shen, *Journal of Power Sources*, **165**, 739 (2007).

[8] A. F. Ghenciu, *Curr. Opin. Solid State Mater. Sci.*, **6**, 389 (2002).

[9] R. Farrauto, S. Hwang, L. Shore, W. Ruettinger, J. Lampert, T. Giroux, Y. Liu, and O. Ilinich, *Annu. Rev. Mater. Res.*, **33**, 1 (2003).

[10] J. Turner, G. Sverdrup, M. K. Mann, P.-C. Maness, B. Kroposki, M. Ghirardi, R. J. Evans, and D. Blake, *Int. J. Energ. Res.*, **32**, 379 (2008).

[11] E. A. Fletcher, *J. Sol. Energ-T. ASME*, **123**, 63 (2001).

[12] J. E. Funk, *Int. J. Hydrog. Energy*, **26**, 185 (2001).

[13] A. Demirbas, *Prog. Energ. Combust.*, **33**, 1 (2007).

[14] G. W. Huber, S. Iborra, and A. Corma, *Chem. Rev.*, **106**, 4044 (2006).

[15] T. A. Milne, C. C. Elam, R. J. Evans, "Hydrogen from biomass: State of the art and challenges", IEA/H2/TR-02/001(2002).

[16] A. Magnuson, M. Anderlund, O. Johansson, P. Lindblad, R. Lomoth, T. Polivka, S. Ott, K. Stensjo, S. Styring, V. Sundstrom, and L. Hammarstrom, *Acc. Chem. Res.*, **42**, 1899 (2009).

[17] R. E. Blankenship, "Molecular Mechanisms of Photosynthesis", John Wiley & Sons, (2008)

[18] P. M. Vignais and A. Colbeau, *Curr. Iss. Mol. Biol.*, **6**, 159 (2004).

[19] A. Luque and S. Hegedus ed., "Handbook of Photovoltaic Science and Engineering", John Wiley & Sons (2010).

[20] CivicSolar, Transformerless Inverters for Solar PV: http://www.civicsolar.com/resource/transformerless-inverters-solar-pv

[21] International Electrotechnical Commission, Efficient electrical energy transmission and distribution: http://www.iec.ch/about/brochures/pdf/technology/transmission.pdf

[22] J. A. Turner, *Science*, **285**, 687 (1999).

[23] M. G. Walter, E. L. Warren, J. R. McKone, S. W. Boettcher, Q. Mi, E. A. Santori, and N. S. Lewis, *Chem. Rev.*, **110** (2010).
[24] X. B. Chen, S. H. Shen, L. J. Guo, and S. S. Mao, *Chem. Rev.*, **110**, 6503 (2010).
[25] W. Kim, T. Tachikawa, T. Majima, W. Choi, *J. Phys. Chem. C*, **113**, 10603 (2009).
[26] H. Kato, K. Asakura and A. Kudo, *J. Am. Chem. Soc.*,**125**, 3082 (2003).
[27] X. Chen, C. Li, M. Gratzel, R. Kostecki, and S. S. Mao, *Chem. Soc. Rev.*, **41**, 7909 (2012).
[28] K. Sivula, F. Le Formal, and M. Graetzel, *Chemsuschem*,**4** , 432 (2011).
[29] D. F. Wang, A. Pierre, M. G. Kibria, K. Cui, X. G. Han, K. H. Bevan, H. Guo, S. Paradis, A. R. Hakima, and Z. T. Mi, *Nano Lett.*, **11**, 2353 (2011).
[30] S. D. Tilley, M. Cornuz, K. Sivula, and M. Graetzel, *Angew. Chem.-Int. Edit.*, **49**, 6405 (2010).
[31] M. F. Weber, M. J. Dignam, *J. Electrochem. Soc.*, **131**, 1258 (1984).
[32] H. Kato and A. Kudo, *J. Phys. Chem. B*, **105**, 4285 (2001).
[33] H. Park, W. Choi, and M .R. Hoffmann, *J. Mater. Chem.*, **18**, 2379 (2008).
[34] H. G. Kim, E. D. Jeong, P. H. Borse, S. Jeon, K. Yong, W. Li, and S. H. Oh, *Appl. Phys. Lett.*, **89**, 064103 (2006).
[35] R. H. Coridan, M. Shaner, C. Wiggenhorn, B. S. Brunschwig, and N. S. Lewis, *J. Phys. Chem. C*, **117**, 6949 (2013).
[36] Q.-B. Ma, B. Kaiser, and W. Jaegermann, *J. Power Sources*, **253**, 41 (2014).
[37] K. Sivula, F. Le Formal, and M. Graetzel, *Chem. Mater.*, **21**, 2862 (2009).
[38] A. Fujishima and K. Honda, *Nature*, **238**, 37 (1972).
[39] Y. Lin, G. Yuan, R. Liu, S. Zhou, S. W. Sheehan, and D. Wang, *Chem. Phys. Lett.*, **507**, 209 (2011).
[40] M. Kitano and M. Hara, *J. Mater. Chem.*, **20**, 627 (2010).
[41] R. M. Navarro Yerga, M. C. Alvarez Galvan, F. del Valle, J. A. Villoria de la Mano, and J. L. G. Fierro, *Chemsuschem*, **2**, 471 (2009).
[42] A. Kudo and Y. Miseki, *Chem. Soc. Rev.*, **38**, 253 (2009).
[43] N. Serpone and E. Pelizzetti, "Photocatalysis", Wiley (1989).
[44] J. D. Beach, R. T. Collins, and J. A. Turner, *J. Electrochem. Soc.*, **150**, A899 (2003).
[45] R. Abe, *J. Photochem. Photobiol. C*, **11**, 179 (2010).
[46] T. Umebayashi, T. Yamaki, H. Itoh, K. Asai, *J. Phys. Chem. Solid*, **63**, 1909 (2002).
[47] T. Nishikawa, Y. Shinohara, T. Nakajima, M. Fujita, S. Mishima, *Chem. Lett.*, **28**, 1133 (1999).
[48] R. Abe, M. Higashi, K. Sayama, Y. Abe, H. Sugihara, *J. Phys. Chem. B*, **110**, 2219 (2006).
[49] Y. Yang, Q. Y. Chen, Z. L. Yin, J. Li. *Appl. Surf. Sci.*, **255**, 8419 (2009).
[50] V. R. Reddy, D. W. Hwang, J. S. Lee, *Catal. Lett.*, **39**, 90 (2003).
[51] K. Domen, A. Kudo, A. Shinozaki, A. Tanaka, K. Maruya, and T. Onishi, *J. Chem. Soc.*, **4**, 356 (1986).
[52] A. Kudo, A. Tanaka, K. Domen, K. Maruya, K. Aika, and T. Onishi, *J. Catal.*, **111**, 67 (1988).
[53] I. M. Huygens, A. Theuwis, W. P. Gomes, and K. Strubbe, *PCCP*, **4**, 2301 (2002).

[54] H. Yan, J. Yang, G. Ma, G. Wu, X. Zong, Z. Lei, J. Shi, and C. Li, *J. Catal.*, **266**, 165 (2009).
[55] T. Ohmori, H. Mametsuka, and E. Suzuki, *Int. J. Hydrogen Energy*, **25**, 953 (2000).
[56] M. Liu, W. You, Z. Lei, G. Zhou, J. Yang, G. Wu, G. Ma, G. Luan, T. Takata, M. Hara, K. Domen, and C. Li, *Chem. Commun*. **19**, 2192 (2004).
[57] D. K. Zhong, J. Sun, H. Inumaru, and D. R. Gamelin, *J. Am. Chem. Soc*., **131**, 6086 (2009).
[58] D. K. Zhong and D. R. Gamelin, *J. Am. Chem. Soc*., **132**, 4202 (2010).
[59] S. D. Tilley, M. Schreier, J. Azevedo, M. Stefik, and M. Graetzel, *Adv. Funct. Mater*., **24**, 303 (2014).
[60] R. Asai, H. Nemoto, Q. Jia, K. Saito, A. Iwase, and A. Kudo, *Chem. Commun*., **50**, 2543 (2014).
[61] H. S. Jeon, A. D. C. Permana, J. Kim, and B. K. Min, *Int. J. Hydrog. Energy*, **38**, 6092 (2013).
[62] S. Trasatti, *J. Electroanal. Chem.*, **111**, 125 (1980).
[63] S. Trasatti, "*Electrodes of Conducti*V*e Metallic Oxides*", Elsevier (1980).
[64] Q. Peng, J. S. Lewis, P. G. Hoertz, J. T. Glass, and G. N. Parsons, *J. Vac. Sci. Technol. A*, **30**, 1 (2012).
[65] T. Tynell and M. Karppinen, *Semicond. Sci. Technol*., **29**, 4 (2014).
[66] S. M. George, *Chem. Rev.*, **110**, 111 (2010).
[67] A. Paracchino, V. Laporte, K. Sivula, M. Graetzel, and E. Thimsen, *Nature Mater*., **10**, 6 (2011).
[68] Y. W. Chen, J. D. Prange, S. Duehnen, Y. Park, M. Gunji, C. E. D. Chidsey, and P. C. McIntyre, *Nature Mater*., **10**, 7 (2011).
[69] M. H. Lee, K. Takei, J. Zhang, R. Kapadia, M. Zheng, Y.-Z. Chen, J. Nah, T. S. Matthews, Y.-L. Chueh, J. W. Ager, and A. Javey, *Angew. Chem.-Int. Edit.*, **51**, 10760 (2012).
[70] L. Guo, D. Hung, W. Wang, W. Shen, L. Zhu, C.-L. Chien, and P. C. Searson, *Appl. Phys. Lett.*, **97**, 063111 (2010).
[71] K. Zeng and D. Zhang, *Prog. Energ. Combust.*, **36**, 307 (2010).
[72] L. Liu and J. H. Edgar, *Mater. Sci. Eng. R*, **37**, 61 (2002).
[73] O. Ambacher, *J. Phys. D: Appl. Phys.*, **31**, 2653 (1998).
[74] S. C. Jain, M. Willander, J. Narayan, and R. Van Overstraeten, *J. Appl. Phys.*, **87**, 965 (2000).
[75] http://en.wikipedia.org/wiki/Electrolysis_of_water#Efficiency
[76] V. Yu. Davydov, A. A. Klochikhin, R. P. Seisyan, and V. V. Emtsev, *Phys. Status Solidi B*, **229**, R1 (2002).
[77] B. Monemar, *Phys. Rev. B*, **10**, 676 (1974).
[78] M. R. Krames, O. B. Shchekin, R. Mueller-Mach, G. O. Mueller, L. Zhou, G. Harbers, and M. G. Craford, *J. Display Technol.*, **3**, 160 (2007).
[79] S. Nakamura, M. Senoh, S. Nagahama, N. Iwasa, T. Yamada, T. Matsushita, H. Kiyoku, Y. Sugimoto, T. Kozaki, H. Umemoto, M. Sano, and K. Chocho, *J. Cryst. Growth*, **189**, 820 (1998).
[80] O. Jani, I. Ferguson, C. Honsberg, and S. Kurtz, *Appl. Phys. Lett.*, **91**, 132117 (2007).

[81] J. Luis Pau, J. Anduaga, C. Rivera, A. Navarro, I. Alava, M. Redondo, and E. Munoz, *Appl. Opt.*, **45**, 7498 (2006).
[82] J. Wu, W. Walukiewicz, K. M. Yu, W. Shan, J. W. Ager, E. E. Haller, H. Lu, W. J. Schaff, W. K. Metzger, and S. Kurtz, *J. Appl. Phys.*, **94**, 6477 (2003).
[83] J. Wu, W. Walukiewicz, K. M. Yu, J. W. Ager, E. E. Haller, H. Lu, and W. J. Schaff, *Appl. Phys. Lett.*, **80**, 4741 (2002).
[84] E. Fred Schubert, "Light-Emitting Diodes", Cambridge University Press (2006).
[85] J. D. Beach, *doctoral dissertation*, Colorado School of Mines (2002).
[86] K. Cheng, M. Leys, S. Degroote, M. Germain, and G. Borghs, *Appl. Phys. Lett.*, **92**, 192111 (2008).
[87] E. S. Mengistu, *doctoral dissertation*, Kassel University (2008).
[88] S. C. Jain, M. Willander, J. Narayan, and R. Van Overstraeten, *J. Appl. Phys.*, **87**, 965 (2000).
[89] M. A. Reshchikov and H. Morkoc, *J. Appl. Phys.*, **97**, 061301 (2005).
[90] P. Ruterana and G. Nouet, *Phys. Status Solidi B*, **227**, 177 (2001).
[91] S. J. Pearton, J. C. Zolper, R. J. Shul, and F. Ren, *J. Appl. Phys.*, **86**, 1 (1999).
[92] K. Cheng, M. Leys, S. Degroote, B. Van Daele, S. Boeykens, J. Derluyn, M. Germain, G. Van Tendeloo, J. Engelen, and G. Borghs, *J. Electron. Mater.*, **35**, 592 (2006).
[93] A. Able, W. Wegscheider, K. Engl, J. Zweck, *J. Crystal Growth*, **276** 415(2005).
[94] H. Marchand, L. Zhao, N. Zhang, B. Moran, R. Coffie, U.K. Mishra, J.S. Speck, S.P. DenBaars, J.A. Freitas, *J. Appl. Phys.*, **89,** 7846 (2001).
[95] A. Sakai, H. Sunakawa, and A. Usui, *Appl. Phys. Lett.*, **73**, 481 (1998).
[96] B. Beaumont, P. Vennegues, and P. Gibart, *Phys. Status Solidi B*, **227**, 1 (2001).
[97] U.S. Department of Energy. Hydrogen, Fuel Cells and Infrastructure Technologies Program. http://www.nrel.gov/docs/fy05osti/34289.pdf
[98] S. U. M. Khan, M. Al-Shahry and W. B. Ingler Jr., *Science*, **297**, 2243 (2002).
[99] M. Gratzel, *Nature*, **441**, 338 (2001).
[100] O. Khaselev, J. A. Turner, *Science*, **280**, 425 (1998).
[101] G. B. Stringfellow, *J. Cryst. Growth*, **312**, 735 (2010).
[102] T. Nagatomo, T. Kuboyama, H. Minamino, O. Omoto, *Jpn. J. Appl. Phys.*, **28**, L1334 (1989).
[103] R. Singh, D. Doppalapudi, T. D. Moustakas, and L. T. Romano, *Appl. Phys. Lett.*, **70**, 1089 (1997).
[104] B. N. Pantha, H. Wang, N. Khan, J. Y. Lin, and H. X. Jiang, *Physical Review B*, **84** (2011).
[105] Y. J. Hwang, C. H. Wu, C. Hahn, H. E. Jeong, and P. D. Yang, *Nano Lett.*, **12**, 1678 (2012).
[106] C. Pendyala, J. B. Jasinski, J. H. Kim, V. K. Vendra, S. Lisenkov, M. Menon, and M. K. Sunkara, *Nanoscale*, **4**, 6269 (2012).
[107] J. Kamimura, P. Bogdanoff, J. Laehnemann, C. Hauswald, L. Geelhaar, S. Fiechter, and H. Riechert, *J. Am. Chem. Soc.*, **135**, 10242 (2013).
[108] D. F. Wang, A. Pierre, M. G. Kibria, K. Cui, X. G. Han, K. H. Bevan, H. Guo, S. Paradis, A. R. Hakima, and Z. T. Mi, *Nano Lett.*, **11**, 2353 (2011).
[109] B. AlOtaibi, M. Harati, S. Fan, S. Zhao, H. P. T. Nguyen, M. G. Kibria, and Z. Mi, *Nanotechnology*, **24**, 175401 (2013).

[110] L. Wang, W. Zhao, Z. B. Hao, and Y. Luo, *Chin. Phys. Lett.*, **28**, 4 (2011).
[111] B. AlOtaibi, H. P. T. Nguyen, S. Zhao, M. G. Kibria, S. Fan, and Z. Mi, *Nano Lett.*, **13**, 4356 (2013).
[112] N. H. Alvi, P. E. D. Soto Rodriguez, P. Kumar, V. J. Gomez, P. Aseev, A. H. Alvi, M. A. Alvi, M. Willander, and R. Noetzel, *Appl. Phys. Lett.*, **104**, 223104 (2014).
[113] J.-S. Hwang, T.-Y. Liu, S. Chattopadhyay, G.-M. Hsu, A. M. Basilio, H.-W. Chen, Y.-K. Hsu, W.-H. Tu, Y.-G. Lin, K.-H. Chen, C.-C. Li, S.-B. Wang, H.-Y. Chen, and L.-C. Chen, *Nanotechnology*, **24**, 055401 (2013).
[114] K. Kumakura, T. Makimoto, N. Kobayashi, T. Hashizume, T. Fukui, and H. Hasegawa, *Appl. Phys. Lett.*, **86**, 052105 (2005).
[115] J. Benton, J. Bai, and T. Wang, *Appl. Phys. Lett.*, **102**, 173905 (2013).
[116] A. M. Basilio, Y.-K. Hsu, W.-H. Tu, C.-H. Yen, G.-M. Hsu, O. Chyan, Y. Chyan, J.-S. Hwang, Y.-T. Chen, L.-C. Chen, and K.-H. Chen, *J. Mater. Chem.*, **20**, 8118 (2010).
[117] S.-W. Ryu, Y. Zhang, B. Leung, C. Yerino, and J. Han, *Semicond. Sci. Technol.*, **27**, 015014 (2012).

CHAPTER 2

Experimental

Chapter 2. Experimental

In this chapter, we introduce the preparation of the working electrode, the design of electrochemical cell and the light source used for this dissertation work.

2.1 The preparation of n-GaN photoanodes

An 8" n-GaN epi-wafer was first diced into squares of 15×15 mm^2. The diced n-GaN sample was then immersed in acetone and isopropyl alcohol (IPA) to remove organic contamination [1], followed by a rinsing with de-ionized (DI) water and drying with N_2. Subsequently, the sample was immersed in HCl aqueous solution (vol. 17%) to remove metallic contamination [1], followed by another rinsing of DI water and drying with N_2.

Figure 2.1 (a) schematically illustrates a cross-section structure of a working electrode. A metal stack of (GaN/)Ti/Al/Mo/Au (30/60/35/500 nm) was deposited by sputtering (Spider 630, Pfeiffer) for the formation of an Ohmic contact to n-GaN (object 2) [2]-[5]. A dummy Si of 13×13 mm^2 was used as a shadow mask at the front side of GaN sample

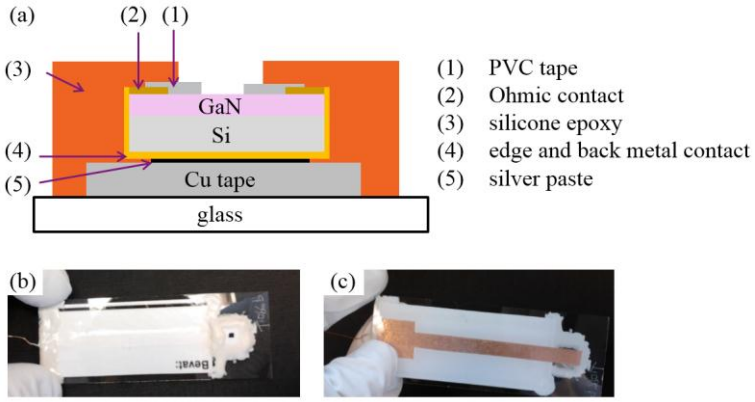

Figure 2.1: (a) A schematic illustration of the cross section of a working electrode. Pictures of the working electrode (b) at the front side and (c) the back side.

during the metal deposition, resulting in a 1 mm wide metal frame at the edge of the n-GaN for electrical contact. Ti is used to improve the adhesion of the metal layer and to reduce the contact resistivity; Al is used to form an Ohmic contact to n-GaN; Mo serves as a barrier layer to prevent the diffusion of Au during the annealing; Au is used to improve electrical conductivity of the stack and to prevent oxidation of the inner metal layers. Another metal stack of (Si/)Ti/Mo/Au: 20/50/300 nm was deposited at the backside of the sample (object 4) using sputtering. The sample edge was covered with metals during the front side and backside deposition. Therefore, electrical current can be extracted from the contact at the sample backside. After the metal depositions, the sample was annealed at 700℃ for 1 minute in N_2 environment using rapid thermal annealing (AS-One, Annealsys) to form the Ohmic contact to n-GaN [2],[6]. The contact resistance of the Ohmic contact to n-GaN is typically lower than 5×10^{-7} Ω -cm^2 [2]. The contact area is typically 0.07-0.10 cm^2.

Regarding the preparation of the working electrode, a conductive Cu tape (AT528, Advance) was first stuck on a glass slide (631-1550, VWR). A Cu wire was taped on one side of the Cu tape as an external connection to the working electrode. The GaN sample was then mounted on the other side of the copper tape using conductive silver paste (Pelco 187, Ted Pella) (object 5). A PVC tape (object 1) was used to define the working area of the electrode. Silicone epoxy (Torr Seal, Varian) (object 3) was used to shield the other components from the solution. The typical electrical resistance between the front metal contact and the Cu wire ranges between 0.5 and 1.5 Ω, measured by a multimeter. Figure 2.1 (b) and (c) show pictures of a representative working electrode at the front side and backside, respectively.

The open area of the working electrode was assessed as follows: The opening of the working electrode was manually cut from the PVC tape using a sharp blade. The paper with the opening was scanned by a copy machine and was printed after being magnified by 256 times. The weight of the magnified open area was measured by a laboratory weighting scale (resolution: 0.0001 g). The typical weight of the magnified open area is 0.04-0.07 g. The typical open area of the working area is 25-50 mm^2.

To exam the light transmission of the PVC tape, the photocurrent density of an n-GaN

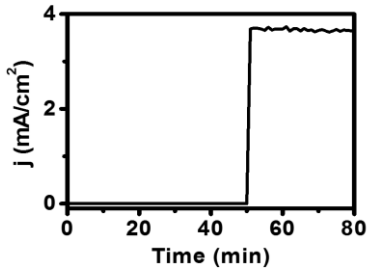

Figure 2.2: A current density-time plot of an n-GaN. The light was shielded by a PVC tape at the first 50 seconds. Solution: 1 M HCl; U_{WE-RE} = 0.5 V.

as a function of time was recorded under illumination, as shown in Figure 2.2. The n-GaN was biased at 0.5 V. For t < 50 s, the light was shielded by the PVC tape in front of n-GaN; for t > 50 s, the light was illuminated at the surface of n-GaN. No photocurrent is observed as the light was shielded. It confirms that photo-excitation is only possible for the GaN in the open area of the working electrode.

2.2 Photoelectrochemical cell and its measurement control

A potentiostat (Autolab, Metrohm) was used for the current-potential control. General-Purpose-Electrochemical-System-Software (GPES) was used to control the potentiostat (Autolab, Metrohm) for voltammogram measurements and chronoamperometric measurements [7]; Frequency Response Analysis (FRA) was used to control the potentiostat for impedance measurements [7].

A picture of the photoelectrochemical cell used in this dissertation work is shown in Figure 2.3. This cell is built of quartz. This quartz cell was regularly cleaned using concentrated HNO_3 aqueous solution (vol. 68%) [1]. The distance between the working electrode and reference electrode is 1.5 cm; the distance between the working electrode and counter electrode is 5.0 cm. In some cases, the solution was agitated using a magnetic stirring bar during the measurements to remove bubbles generated at the electrode surface or to assure that the electrochemical reaction is predominantly under kinetic control.

An Ag/AgCl reference electrode (6.0726.107, Metrohm) with electrolyte of 3 M KCl

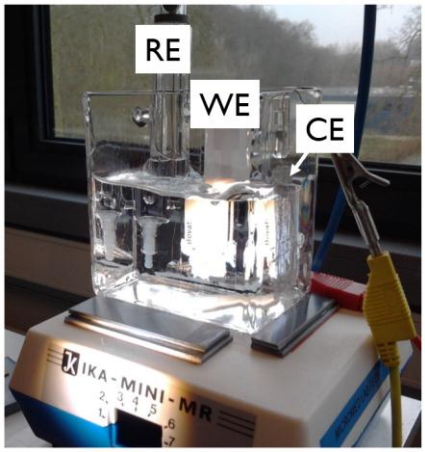

Figure 2.3: A picture of the photoelectrochemical cell used in this dissertation work including a working electrode (WE), reference electrode (RE) and counter electrode (CE).

was used as a potential reference during the electrochemical measurements. The potential *vs.* a standard hydrogen electrode is +210 mV at 25 °C [8]. All electrochemical measurements were carried out at room temperature. The electrolyte of the reference electrode was replaced every three months. A Pt gauze (7440-06-4, Alfa) was used as a counter electrode for the electrochemical measurements. The open area of the gauze is 63% and the effective surface area is 4 cm^2. The Pt gauze was cleaned using HNO_3 solution (vol. 68%) every three months.

An aqueous solution of 0.1 M HBr + 0.2 M Na_2SO_4 (Sigma-Aldrich) was used for (photo)electrochemical measurements in Chapter 4- Chapter 6. Otherwise, it will be mentioned. Br^- is used as a hole scavenger to lessen photocorrosion of GaN. Na_2SO_4 is used to enhance the solution conductivity.

2.3 Light source

A 150 W Xe ozone-free lamp (LS1521, L.O.T.-Oriel) with a rear reflector was used as the light source in the photoelectrochemical measurements for this dissertation work. The

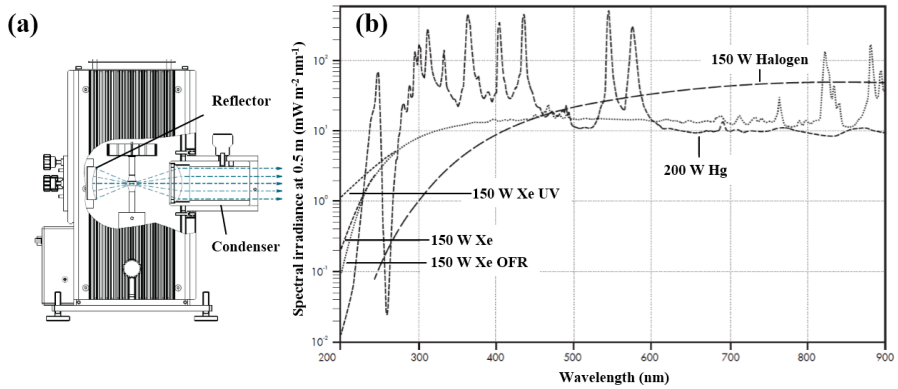

Figure 2.4: (a) Schematics of a Xe lamp and (b) irradiation spectra of Xe lamps. The 150 W Xe ozone-free lamp with a rear reflector (150 W Xe OFR) was used for this dissertation work.

lamp is schematically presented in Figure 2.4 (a). The light is generated by an electric arc burning in Xe gas. The color temperature of the light is 6000-6500 K, which is close to the solar spectrum. To prevent ozone generation, light < 250 nm is absorbed by a quartz coating at the bulb surface. The irradiation spectra of the lamp (150 W Xe OFR) is shown in Figure 2.4 (b). Intensity peaks for $\lambda > 650$ nm are ascribed to different excitation states of Xe in the bulb. The light intensity decreases rapidly for $\lambda < 300$ nm.

The rear reflector assembly in Figure 2.4 (a) consists of a mirror coated with $AlMgF_2$ to enhance the light reflection. The condenser is used to control the horizontal distance of the lens from the light source. In this dissertation work, by choosing a proper location of the lens, the emission of the light can be considered to be in parallel. The light projection at the working electrode plane is a circle with a diameter (∅) = 35 mm. The variation of the light intensity at the center area where ∅ = 15 mm is less than 3 %.

An AM 1.5 G filter (LSZ289, L.O.T.-oriel) was used in front of the condenser to tailor the radiation spectrum of the Xe lamp, as shown in Figure 2.6, so that the filtered spectrum is more similar to the solar spectrum in the AM 1.5 G condition [9]. With the filter, the intensity of infra-red light is reduced so the abrupt intensity peaks contribute less in the irradiation spectrum. More importantly in this dissertation work, the intensity of the UV

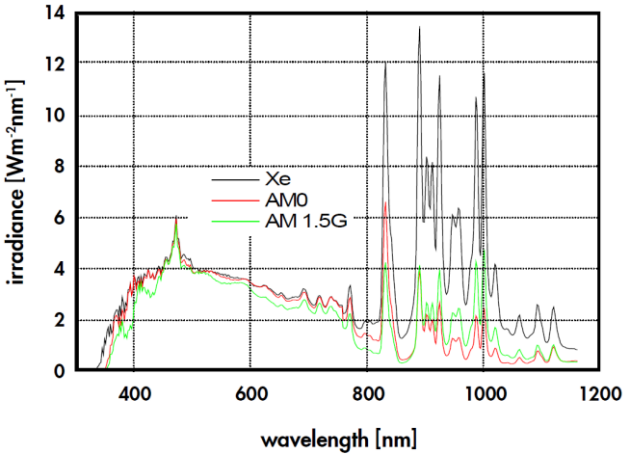

Figure 2.5: The irradiance spectrum of the Xe lamp and the spectra modified by AM0 and 1.5 G filters.

light is reduced by the filter. Therefore, using the filtered light less photocarriers are generated in the n-GaN sample during photoelectrochemical measurements. Consequently, the corrosion of n-GaN which is ascribed to photo-holes is less serious. A thermal power meter (s302c, Thorlabs) was used to assess the light intensity projecting at the surface of the working electrode. The absorption response *vs.* wavelength is shown in Figure 2.5. The absorption efficiency is higher than 98 % and is independent of

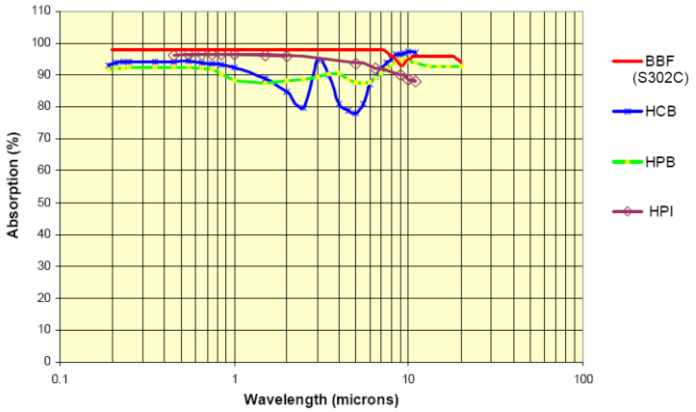

Figure 2.6: Light absorption spectra for different photo-detectors [10]. The detector, BBF (S302C), was used in this dissertation work.

wavelength for $\lambda < 5$ μm. The thermal power meter is calibrated by a solar simulator which is calibrated by a photovoltaic secondary reference cell 0.

For this dissertation work, in Chapter 4 to Chapter 6, the 150 W Xe lamp with AM 1.5 filter was used for the light source. The light intensity of the integrated radiance spectrum illuminated at the sample surface was 63 mW/cm^2, measured by the thermopile detector. If the projected light intensity is not the case, it will be mentioned.

2.4 References

[1] K. A. Reinhardt (ed.), "Handbook for Cleaning for Semiconductor Manufacturing: Fundamentals and Applications", Wiley (2011).

[2] V. Kumar, L. Zhou, D. Selvanathan, and I. Adesida, *J. Appl. Phys.*, **92**, 1712 (2002).

[3] S. N. Mohammad, *J. Appl. Phys.*, **95**, 7940 (2004).

[4] D. Selvanathan, F. M. Mohammed, A. Tesfayesus, and I. Adesida, *J. Vac. Sci. Technol. B*, **22**, 2409 (2004).

[5] L. Wang, F. M. Mohammed, and I. Adesida, *J. Appl. Phys.*, **101**, 013702 (2007).

[6] F. M. Mohammed, L. Wang, and I. Adesida, *Appl. Phys. Lett.*, **88**, 212107 (2006)

[7] www.metrohm.ch/produkte/Autolab.html

[8] Metrohm, Metrosensor electrodes. http://www.metrohm.cz/Download/8.000.5037EN_elektrody.pdf

[9] Green Rhino Energy, standard spectra for solar panels. http://www.greenrhinoenergy.cokm/solar/radiation/spectra.php

[10] Thorlabs, s302c thermal power doctor. http://www.thorlabs.de/thorproduct.cfm?partnumber=S302C
National Renewable Energy Laboratory, Device performance measurement. http://www.nrel.gov/pv/measurements/device_performance.html

CHAPTER 3

n-GaN/solution interface

Chapter 3. n-GaN/solution interface

3.1 Introduction

At a metal/solution interface, electrons are abundantly supplied at the electrode surface. The charge transfer is either a capture process or an injection process of electrons. The charge transfer rate is limited by the kinetics of electrochemical reactions or mass transport at the solution side. However, in the case of a semiconductor/solution interface, semiconductor physics plays a determining role in the charge transfer. The carrier availability at the surface of the semiconductor depends on surface band bending. Besides electrons, under illumination of supra-bandgap light holes are photo-generated in the semiconductor and participate in the electrochemical reactions. Carriers in conduction band (CB) and valence band (VB) of the semiconductor can participate in charge transfer if there are available redox states at the solution side.

In this chapter, the n-type semiconductor/liquid interface is discussed using n-GaN as an example. The thermal equilibrium of the n-type semiconductor/liquid interface is first mentioned, followed by an introduction of interfacial charge transfer mechanism. The characterization techniques (i.e. cyclic voltammetry and impedance spectroscopy) used for this dissertation work are then introduced. Finally, photo-stability of n-GaN during the measurements in the presence of sacrificial reducing agents (Br^-) in the solution is discussed.

3.2 Band diagram of the semiconductor/solution interface

3.2.1 Interfacial energy alignment

When a semiconductor and solution are in contact, energetic alignment occurs at the interface for a new thermal equilibrium [1]. Here, an n-type semiconductor and solution containing a redox system are used to elaborate the interfacial energy alignment. Figure 3.1 (a) shows energy levels of the n-type semiconductor and the redox couples before

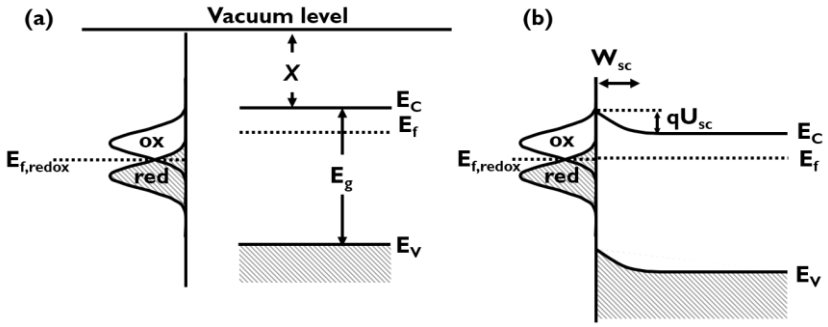

Figure 3.1: Energy diagrams of a redox system in the solution and an n-type semiconductor (a) before and (b) after the contact.

contact. The vacuum energy level is an energy reference for these two systems. Here, to simplify the discussion, we presume that there are no surface states, surface oxide and surface adsorption of solvated species at the semiconductor, so surface band bending does not exist. The energy of the CB edge and the VB edge are denoted as E_C and E_V in the figure, respectively. The bandgap energy (E_g) is given by $E_C - E_V$. The Fermi level energy (E_f) is determined by electron concentration (n_0) or hole concentration (p_0) of the semiconductor, as described by [2]

$$n_0 = N_C \exp\left(-\frac{E_c - E_f}{kT}\right) \tag{3.1}$$

$$p_0 = N_V \exp\left(-\frac{E_f - E_V}{kT}\right) \tag{3.2}$$

where k is the Boltzmann constant and T is the absolute temperature. N_C and N_V are the effective density of states in the CB and VB, respectively. Here we assume the n-type semiconductor is uniformly doped, so n_0 is location-independent.

At the solution side, to simplify the discussion, we assume the redox couple is under standard conditions and the oxidant becomes the reductant after receiving an electron:

$$\mathrm{Ox} + \mathrm{e}^- = \mathrm{Red} \tag{3.3}$$

Reductants and oxidants in Figure 3.1 (a) energetically correspond to occupied states and empty states of electrons, respectively. The standard Fermi energy of the redox system is

denoted as $E^{\circ}_{f,redox}$. Because the Fermi energy of the semiconductor is higher than that of the redox couple, when the n-type semiconductor is in contact with the solution (Figure 3.1 (b)), electrons of the semiconductor therefore transfer to the solution, leaving an electron-depleted region at the semiconductor surface. This region is named depletion region or space-charge region (SCR). Electrons of the n-type semiconductor are provided by donors. Electron donors are positively charged after ionization. Therefore, following depletion of electrons, the SCR loses charge neutrality and becomes positively charged. After energy alignment with the solution, the bands at the surface bend downward towards bulk for the n-type semiconductor, and the potential drop over the SCR (U_{sc}) is built up. The width of the SCR (W_{sc}) can be described by [3]

$$W_{sc} \approx \sqrt{\frac{2\varepsilon\varepsilon_0 U_{sc}}{q n_0}} \tag{3.4}$$

where ε_0 is the vacuum permittivity and ε is the dielectric constant of the semiconductor.

3.2.2 Surface band bending of n-type semiconductor

When the surface bands bend, the energy difference between E_C and E_f changes. Therefore, for the n-type semiconductor, the surface electron concentration (n_s) is different from the bulk electron concentration (n_0). The relation between n_s and n_0 can be described by

$$n_s = n_0 \exp\left(-\frac{qU_{sc}}{kT}\right) \tag{3.5}$$

$$p_s = p_0 \exp\left(\frac{qU_{sc}}{kT}\right) \tag{3.6}$$

When the n-type semiconductor is in depletion condition, $n_s < n_0$ and $p_s > p_0$ as a result of increased energy difference between the E_C and E_f with respect to the bulk. The minus sign in the exponential term indicates that once a positive U_{sc} is formed (the bands bend downward), n_s decreases.

By applying an additional positive potential at the semiconductor, the bands bend further downward, as shown in Figure 3.2 (a). W_{sc} expands as a result of stronger electron

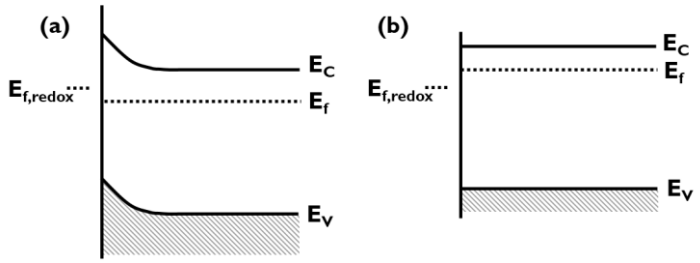

Figure 3.2: Band diagrams of the n-type semiconductor/ solution junction under (a) depletion and (b) flat band. The equilibrium case is shown in Figure 3.1 (b).

depletion. In contrast, when a negative potential is applied, the Fermi-level moves upward. At a particular potential, termed flat-band potential (U_{fb}), the bands become flat (U_{sc} = 0) (Figure 3.2 (b)). At U_{fb}, the carrier concentration at the surface equals to the bulk. It is not straight forward to directly determine U_{sc} experimentally. However, U_{fb} is obtainable from experiments (see Section 3.5.1). Therefore, it is convenient to use U_{fb} as a potential reference. U_{sc} can then be determined experimentally using the relationship of

$$U_{sc}=U-U_{fb} \tag{3.7}$$

where U is the external potential applied over the semiconductor. Using Eq. (3.7), W_{sc} can be rewritten as

$$W_{sc}=\sqrt{\frac{2\varepsilon\varepsilon_0(U-U_{fb})}{qn_0}} \tag{3.8}$$

The SCR behaves electrically as a capacitor since the charge is stored locally. Using a parallel plate model, the capacitance density of SCR (C_{sc}) can be described as

$$C_{sc}=\frac{\varepsilon\varepsilon_0}{W_{sc}} \tag{3.9}$$

3.2.3 Helmholtz double layer

The other side of the interface is a liquid system. For details of redistribution of solvated species at the surface of solid state see Ref. [4]-[6]. The liquid system consists of mobile

solvated ions and molecules. Ions and molecular dipoles move in response to electrostatic attraction or repulsion; or they can be adsorbed at the electrode surface. Therefore, the distribution of species near the electrode/liquid interface is different from the bulk solution. Figure 3.3 schematically illustrates the distribution of species in the solution near the interface. According to the charge distribution, three layers are classified. From the electrode side to the bulk solution, these layers are inner Helmholtz layer (IHL), outer Helmholtz layer (OHL) and Gouy layer.

At the electrode surface, ions or molecules in the solution can be physically adsorbed. In the presence of specific sites or facets, ionic or molecular species can even form chemical bonds with the electrode surface. These ions and molecules are directly in contact with the electrode surface and form the IHL. The electrical charge center is located at x_1. Out of the IHL, molecules or ions are still attracted to the electrode by the electrostatic force, resulting in the OHL with the electrical charge center is at x_2. The formation of the Gouy layer also results from electrostatic attraction of the charge of SCR.

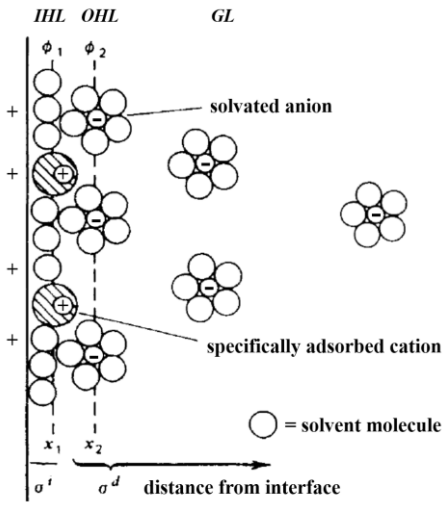

Figure 3.3: Schematic illustration of species distribution at an n-type semiconductor/solution interface. Layers from the electrode to bulk solution: inner Helmholtz layer (IHL), outer Helmholtz layer (OHL) and Gouy layer (GL) [4].

However, in contrast to the Helmholtz double layer, the distance of species-electrode interaction is much longer.

The Helmholtz layer and Gouy layer keep the charge neutrality at the interface region. The SCR of the n-type semiconductor possesses a positive charge, termed Q_{sc}, due to depletion of electrons at the surface. Ions and molecules redistribute at the electrode surface and an imaging charge is formed. The charges at the Helmholtz double layer and Gouy layer are denoted by Q_H and Q_G, respectively. This regional charge neutralization across the semiconductor/electrolyte interface is described by

$$Q_{SCR} = Q_H + Q_G \tag{3.10}$$

when the concentration of conducting salts is high enough (typically > 0.01 M), the thickness of the Gouy layer becomes very thin and can even be merged into the OHL. In this dissertation, the electrolyte concentration is high (i.e. 0.2 M Na_2SO_4) so the Gouy layer is negligible in the discussion.

The charge stored in the Helmholtz layer (the negative charge in Figure 3.4 (a)) and the charge in SCR (the positive charge in the figure) forms a capacitor. All charges of the Helmholtze layer are populated within a narrow distance from the electrode surface (d). Using a parallel plate model, the capacitance density of the Helmholtz layer (C_H) can be described as

$$C_H = \frac{\varepsilon_0 \varepsilon}{d} \tag{3.11}$$

where ε_0 is the vacuum permittivity (= 8.854×10^{-12} F/m) and ε is the dielectric constant of the media. Therefore, the potential drop (U_H) over the Helmholtz layer and charge density of the Helmholtz layer (Q_H) can be can be linked by

$$C_H = \frac{Q_H}{U_H} \tag{3.12}$$

The overall capacitance over the interface including the semiconductor and solution system can be described as

$$\frac{1}{C} = \frac{1}{C_{sc}} + \frac{1}{C_H} \tag{3.13}$$

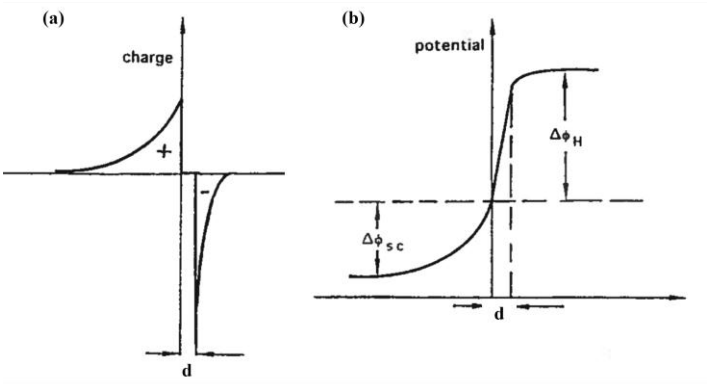

Figure 3.4: (a) Charge and (b) potential distribution at the n-type semiconductor/solution interface [12].

where C_{sc} and C_H are defined respectively in Eq. (3.9) and Eq. (3.11). Due to the relative low carrier concentration of the semiconductor, C_{sc} is typically smaller than C_H by one to two order of magnitude. Therefore, the overall capacitance across the interface is predominately limited by C_{sc}. Taking a general case as an example: suppose an n-type GaN has a carrier concentration of 5×10^{18} cm^{-3} and the potential drop over SCR is 1 V, W_{sc} is calculated to be 14 nm using Eq. (3.8); C_{sc} ~0.6 μF/cm^2. In contrast, taking a solid state/liquid interface with a general electrolyte medium with ε = 20 and thickness of Helmholtz layer = 5 Å, C_H is ~ 30 μF/cm^2 [7].

Charge storage in the SCR and Helmholtz layer creates potential barriers at each interface, as shown in Figure 3.4 (b). The potential drop across the interface can be described by

$$U = U_{sc} + U_H \tag{3.14}$$

where U_{sc} and U_H are the potential difference at the SCR and the Helmholtz double layer, respectively. Here, we presume the ionic conductivity of solution is high enough, so U_{GL} is negligible. As mentioned above, the capacitance of the Helmholtz layer is much larger than the SCR of the semiconductor. Therefore, when the applied potential changes, the corresponding potential change mainly happens across the SCR. With proper Ohmic contact and electrolyte of high ionic conductivity, the applied potential theoretically falls

predominately over the SCR.

3.3 Minority photocarriers

3.3.1 Charge transfer mechanisms

At an n-type semiconductor/solution interface in the dark, three carrier transfer routes are possible [8],[9], as illustrated in Figure 3.5: (1) electron injection in the CB from reductant states in the solution, (2) electron capture by oxidant states from the CB and (3) hole injection in the VB from oxidant states. Under illumination, photo-holes are generated in the n-type semiconductor. The capture of photo-holes by a reductant state from the VB is possible (process 4). Process 4 is not possible at the n-type semiconductor/electrolyte interface in the dark. The charge transfer route (2) and (4) are more important in this dissertation. Process (2) describes the reduction of oxidants when n-GaN is under weak depletion condition. Process (4) describes the oxidation of reductants when n-GaN is in depletion condition and under illumination.

Taking the route (2) as an example, an oxidizing agent can only be reduced by capture of an electron only if the electron and oxidant state both possess the same energy. The partial cathodic charge transfer current density (j_c) therefore depends on the surface concentration of oxidant states ($c_{ox,s}$) and surface electron concentration (n_s), as described by [10]

$$j_c = -q\, k_{red} c_{ox,s}\, n_s \tag{3.15}$$

where k_{red} is the rate constant of electron injection. Notably, the n_s is dependent of U_{sc} (Eq. (3.5)), and $c_{ox,s}$ is a function of energy. Similarly, the partial anodic current density (j_a) ascribed by charge transfer route (4) can be described by

$$j_a = q\, k_{ox} c_{red,s}\, p_s \tag{3.16}$$

where $c_{red,s}$ is the surface concentration of reductant states and k_{ox} is the rate constant of the hole capture. p_s is the surface concentration of photo-holes in the case of an n-type semiconductor under supra-bandgap illumination. It is important to note that p_s in Eq.

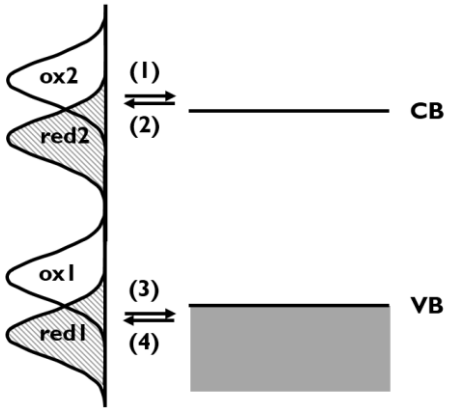

Figure 3.5: Charge transfer paths across an n-type semiconductor/solution interface. The arrows indicate the moving direction of (1)(2) electrons and (3)(4) holes.

(3.16) is not described by Eq. (3.6), but is determined by the light intensity and U_{sc}. For the photo-hole capture process, j_a is typically limited by p_s. For the hole (electron) injection process, the reaction rate is limited by the overlapping of the oxidant (reductant) states with the VB (CB).

Here we use current-potential (j-U) curves of an n-GaN (Figure 3.6) to explain the surface band bending and the charge transfer. The dotted curve and solid curve are for the j-U curves in the dark and under illumination, respectively. The scan starts from positive to negative. An aqueous solution of 1 M HCl was used where Cl^- was a sacrificial reducing agent in the measurement [11]. The reason to use a reducing agent-containing solution instead of inert electrolyte is described in Section 3.6. The solution was agitated during the measurement. Band diagrams of the n-GaN/solution interface under different bias conditions are schematically illustrated in Figure 3.7. The potential barrier across the SCR is denoted as U_{sc} in the figure. It is important to note that the U in Figure 3.6 is the applied potential to the n-GaN, which is not the same as the $U_{sc,}$ as described in Eq. (3.7).

In the dark, no photo-holes are generated. Therefore, the j-U characteristic is mainly a result of the charge transfer of majority carriers. For U < -0.5 V, the surface of the semiconductor is weakly biased (Figure 3.7 (a)). When the U shifts toward negative bias, the n_s increases as the result of decreasing U_{sc} (Eq. (3.5)). Electrons at the interface reduce

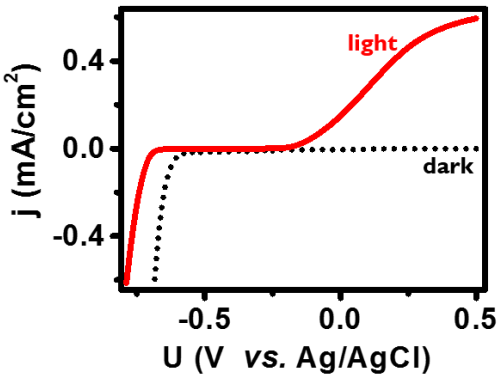

Figure 3.6: Current density-potential (j-U) plots of an n-GaN photoanode in the dark and under illumination. Solution: 1 M HCl; scan rate (v): 1 mV/s

oxygen, which is dissolved from ambient, back to water. The absolute of the cathodic current increases (Eq. (3.15)) when n_s increases. In the case of strong surface depletion (Figure 3.7 (b)), electrons are drifted away from the surface and the n_s becomes negligible. The hole concentration is also negligible in this case due to high bandgap of GaN (3.4 eV) and high doping concentration (5×10^{18} cm^{-3}). Therefore, typically very low anodic current is observed in the dark (less than 50 nA/cm^2 for pristine n-GaN).

Under supra-bandgap illumination, photo-holes are generated. For U < -0.5 V, the surface bands weakly bend (Figure 3.7 (c)). Therefore, n_s is high and p_s is low due to the weak electric field of depletion region. All photo-holes recombine with electrons in this case. The onset potential (U_{onset}) of the oxygen reduction in the dark is more positive than that in the light (see Figure 3.6). This photo-effect may result from the change of surface chemistry (i.e. surface oxidation during the anodic scan) or charging of surface states by photo-holes [13].

When the band bending is sufficiently strong (U > 0.4 V), all photo-holes of the SCR are drifted to the surface and electrons are depleted from the surface (Figure 3.7 (d)). Photo-holes of the SCR are transferred to the solution or are used to corrode GaN. The interfacial charge transfer process is described in Section 3.3.1. In the case of Figure 3.6, Cl^- is the reductant and is oxidized by photo-holes to Cl_2. The photo-corrosion of n-GaN

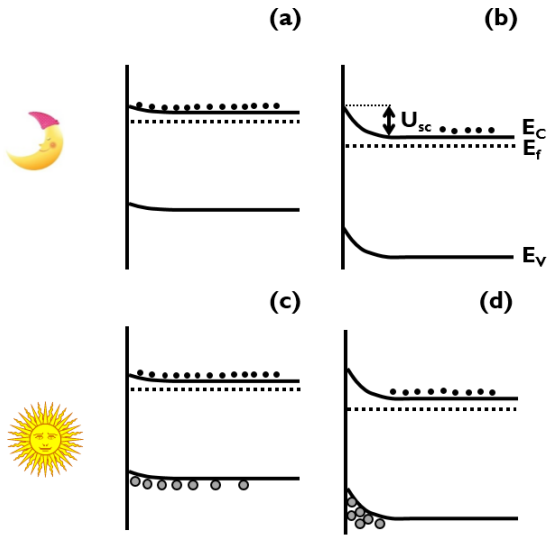

Figure 3.7: Band diagrams of the n-GaN/solution junction in the dark (a) under weak depletion and (b) under strong depletion; under illumination (c) under weak depletion and (d) under strong depletion. The arrows indicate the direction of the current flow.

is described in Section 3.6. In the photocurrent plateau, since all photo-holes in the SCR are separated and surface recombination rate is low, the photocurrent is determined by the number of the photo-holes and is therefore limited by the light intensity (I_0). For a planar n-GaN when the surface recombination is negligible, the plateau photocurrent ($j_{pl,ph}$) can be described by the Gärtner model: [14]

$$j_{pl,ph} = qI_0\left(1 - \frac{\exp(-\alpha W_{sc})}{1+\alpha L_p}\right) \tag{3.17}$$

where α is the absorption coefficient (=1×10^5 cm^{-1} [15]) and L_p is the diffusion length of photo-holes for n-GaN (~ 200-300 nm [16]). W_{sc} is the depletion width of the SCR and is a function of U_{sc} (Eq. (3.4)). It is important to note that here we discuss the case of low projected illumination intensity and high concentration of reducing agents in the solution, so the electrochemical reaction is under kinetic control.

3.3.2 Carrier recombination mechanisms

When n_s is high enough and the surface recombination is not negligible, the Gärtner model fails to describe the relation between j_{ph} and U. Carrier recombination strongly influences the current-potential characteristic between the current onset and the current plateau [17],[18]. Figure 3.8 illustrates possible recombination paths for photo-holes. (i) First, photo-holes are generated by photo-excitation. The supra-bandgap photons are absorbed in GaN and the light intensity decays exponentially as a function of the depth from the surface. The penetration depth of the light is ~ 100 nm ($\alpha_{GaN} = 10^5$ cm^{-1} [15]) where the most of photo-holes are generated.

There are three recombination paths for photo-holes [19]-[22]: (ii) direct recombination, (iii) defect-assisted recombination in the bulk of the semiconductor and (iv) surface recombination. Out of the SCR, the CB and the VB of GaN are flat. Therefore, there is no electric field to separate electrons and holes in the bulk. Photo-holes recombine with electrons through process (ii) and (iii) unless they reach the SCR. The process (ii) describes a direct recombination process between an electron and a hole with emission of a photon. Alternatively, an electron at the CB can first transfer to a trap level in the

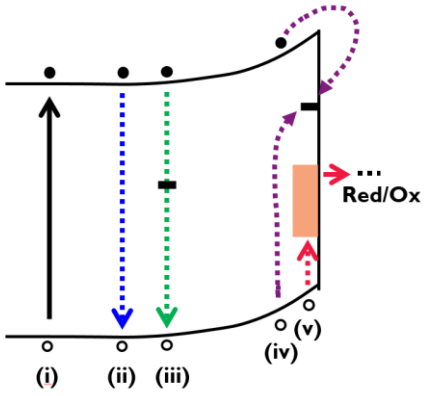

Figure 3.8: Mechanisms associated with photocarriers. After (i) excess carriers are photo-generated, photo-carriers can (ii) recombine directly, (iii) through traps in bulk or (iv) via surface states. Only (v) charge transfer to the solution contributes to photocurrent.

bandgap and then recombines with a hole in the VB, as indicated in process (iii). The process (iii) can be a single step charge transfer or can be a multi-step charge transfer. Typically, the density of surface defects is higher than bulk defects, and the concentration of photo-holes is higher than the bulk. Therefore, although the concentration of electrons at the surface is lower than the bulk, the recombination rate of process (iv) can be higher than process (iii).

Process (v) is the only process that leads to the oxidation of reducing at the working electrode. As mentioned in Figure 3.5, the charge transfer is only possible if holes and reductant states both have the same energetic position. In the case of Figure 3.6, Cl^- is used as the reducing agent, and the reductant states (Cl^-) do not overlap with the VB [23],[24]. Therefore, it is necessary for photo-holes to first transfer to specific surface traps, which are of the same energetic position as the Cl^- states, before the charge can transfer.

Consequently, the measured photocurrent in Figure 3.6 is a result of competitions between the process (ii) to process (v). The U_{onset} of the photocurrent is -0.16 V, and the photocurrent plateau starts at 0.4 V. For $U_{onset} < U$, all photo-holes recombine with electrons through the process (ii) to process (iv). For $-0.16\ V < U < 0.4\ V$, the oxidation of Cl^- is possible but surface recombination is still influential. As U increases, the surface electron concentration is further reduced, and surface recombination becomes suppressed. When the current plateau is reached, all the photo-holes in the SCR are used to oxidize Cl^-.

3.3.3 Roles of surface states

When the lattice periodicity is terminated at the surface of semiconductors, broken bonds form and result in localized electronic states in the bandgap. We use this section to briefly describe the surface state-associated activities in phtoelectrolysis. Here, we use an n-type semiconductor as an example.

A fundamental nature of surface states is the trapping of charges. Surface states refer to the energy levels of the unterminated bonds, and have specific energy with respect to

the CB and VB of the semiconductor bulk, depending on their properties. Free electrons of CB or holes of VB can be captured by surface traps and occupy the traps. Alternatively, they can be released from traps and therefore the states are unoccupied. Depending on the properties of surface traps, the kinetics of electron trapping or hole trapping can be different [39]. The rate of charge trapping and detrapping can be different as well for a surface state.

The property of charge trapping/detrapping of surface states therefore leads to several phenomena in the semiconductor photoelectrochemistry. At the interface of solution and an n-type semiconductor without surface states, an additional external bias predominately falls across SCR. Therefore, the change of Fermi-level potential should be the same as the change of applied bias. However, at the interface of solution and an n-type semiconductor with surface states, this is not always the case. In the case of monoenergetic traps at the semiconductor surface, the applied potential is used to deplete the electron-occupied surface states rather than to change the surface band bending when the Fermi level potential is the same as the potential of the surface states. This is commonly observed in a semiconductor electrode at a weak external bias. In this case, the Fermi-level is pinned and the surface band bending is independent of the bias, unless the surface states are completely depleted [12]. In reality, surface states typically distribute over an energy range in the bandgap. The surface band bending of the SCR can still respond to the external bias. However, the applied potential is distributed over both SCR and the surface states. This partially-pinned Fermi-level effect can be observed in a j-U plot of a semiconductor photoanode under illumination. When Fermi level pinning occurs at the surface of the photoanode, the potential different between the current onset and current plateau ($\Delta U_{onset\text{-}plateau}$) is enlarged [17]. It is important to note that not all surface states lead to Fermi level pining. Fermi level pinning only occurs when the Fermi level energy is the same as surface states. Consequently, not all surface states have an impact on the $\Delta U_{onset\text{-}plateau}$ of a j-U plot under illumination.

Surface states also effect the carrier recombination rate. The presence of surface traps results in a lower j_{ph}, especially at weak surface band bending. Under illumination, photo-holes are present at the surface of photoanodes. Electrons can be first trapped by surface

defects and then recombine with photo-holes. Alternatively, electrons can recombine with trapped photo-holes. For surface recombination via surface states at a specific energy, the carrier recombination rate is proportional to the density of these monoenergetic surface traps. A detailed discussion is given in Section 4.6.1. Hence, carrier recombination rates via different surface states are not the same. Moreover, surface recombination requires a free charge and a surface state occupied by a charge of opposite polarity. Therefore, not all surface states contribute to carrier recombination.

For an n-type semiconductor photoanode, reductants in the solution are oxidized by capture of photo-holes. This interfacial charge transfer only occurs when the photo-holes in the solid state possess the same energy as the occupied states of the reductants in the solution (Figure 3.5). However, for a wide-bandgap semiconductor like GaN, the occupied reductant states may not overlay with the VB. As an example, we can look at the Br_3^-/Br^- redox couple at n-GaN/solution interface, as discussed in Section 3.5.3 and Figure 3.15. The redox potential of Br_3^-/Br^- is 0.92 V, and the potential of the VB edge is 2.63 V *vs.* SHE. For a typical rearrangement potential of ~1 V [12], the direct capture of photo-holes from the VB of GaN is very unlikely to occur. Therefore, the existence of surface states is necessary for this interfacial charge transfer [23],[24]. Photo-holes can be first trapped by surface traps whose potential matches to the potential of reductant states, and subsequently captured by the reductant.

3.4 Study of n-GaN using cyclic voltammetry

3.4.1 Br^--related redox reactions

In this section, cyclic voltammetry was used to characterize photoelectrochemical properties of n-GaN. A Br^--containing solution was used in the measurements to reduce photo-corrosion of n-GaN [25]. In order to understand electrochemical reactions related to Br^-, a cyclic voltammogram of a Pt working electrode is firstly discussed, as shown in Figure 3.9. A solution of 0.1 M HBr + 0.2 M Na_2SO_4 was used and the measurement was recorded at a scan rate of 100 mV/s. The scan starts first positively and then negatively.

In the forward scan, when the Fermi level of the Pt energetically matches to the oxidant states, electrons are injected from Br^- to the Pt electrode and Br^- is oxidized to Br_2, as described by [26]

$$2Br^- \leftrightarrow Br_2 + 2e^- \tag{3.18}$$

The anodic peak at 1.00 V results from the oxidation of Br^- to Br_2. Br_3^- is an intermediate species which is more stable than Br_2. Therefore, once Br_2 is generated at the electrode surface, it immediately forms Br_3^- with another Br^-, as described by [26]

$$Br^- + Br_2 \leftrightarrow Br_3^- \tag{3.19}$$

Eq. (3.19) is a chemical process so there is no charge transfer. The equilibrium constant (defined as $K = [Br_3^-]/[Br^-][Br_2]$) of this equation is 16-20 M^{-1} [27]-[29]. Therefore, the formation of Br_3^- is thermodynamically favored in a Br^- rich medium. Including both Eq. (3.18) and Eq. (3.19), the oxidation of Br^- can be written as

$$3Br^- \leftrightarrow Br_3^- + 2e^- \tag{3.20}$$

However, as Br^- becomes depleted at the electrode surface, Br_3^- decomposes to Br_2 and Br^- (the reverse process of Eq. (3.19)). Subsequently Br^- is available at the surface and is immediately oxidized to Br_2, resulting in the second anodic peak (Figure 3.9) at 1.40 V.

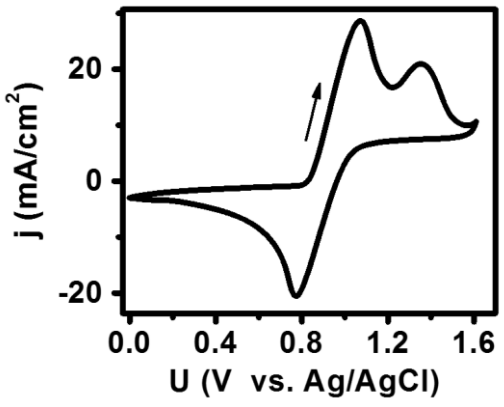

Figure 3.9: A j-U plot for a Pt working electrode in a solution of 0.1 M HBr and 0.2 M Na_2SO_4. *v*: 100 mV/s.

In the cathodic scan, when the Fermi level of the Pt energetically matches to the reductant states, electrons are transferred from the Pt to Br_2. Br_2 is then reduced back to Br^- (the reverse process of Eq. (3.18)), resulting in a cathodic peak at 0.77 V. When the Br_2 concentration at the electrode surface becomes zero, the reaction rate depends only on the diffusion of Br_2 to the surface. The cathodic current is then proportional to the Br_2 concentration gradient, which can be described by the Cottrell equation [4].

3.4.2 Cyclic voltammograms of n-GaN

Now, let's look at the case of the n-GaN/solution interface. Figure 3.10 (a) shows a cyclic voltammogram of an n-GaN photoanode under illumination. The UV light of the Xe lamp was not reduced by an AM 1.5 filter. An aqueous solution of 0.1 M HBr + 0.2 M H_2SO_4 was used. The measurement was scanned at 100 mV/s, and started first in the positive direction and then returned. In order to avoid the reduction of oxygen, the cathodic scan was reversed at -1.25 V.

The concentration of the Br^-/Br_3^- redox couple as a function of distance from the GaN surface is schematically illustrated in Figure 3.10. The potential of the anodic current onset, the anodic peak maximum, the cathodic current onset and the cathodic peak maximum are denoted by $U_{on,a}$, $U_{p,a}$, $U_{on,c}$ and $U_{p,c}$, respectively. The formation of one Br_3^- requires three Br^- (Eq. (3.20)). For better visualization, the concentration of Br_3^- is multiplied by three. In the forward scan, for $U < U_{on,a}$, the concentration of Br^- at the surface equals to the bulk solution, and there is no Br_3^- at the surface. In the anodic scan, Br^- is oxidized to Br_3^-, contributing to the photocurrent, as described by

$$3Br^- + 2h^+ \rightarrow Br_3^- \tag{3.21}$$

The oxidation of Br^- in this case is a hole-capture process. Photo-holes transfer from VB of n-GaN to Br^- states. This process is different from the electron injection from Br^- states to metal in Eq. (3.19), which is not possible in this case due to the energy difference.

At the beginning of the photocurrent onset, the anodic current depends on the competition between charge transfer and surface recombination [19], which depends on the electric field of the SCR. The kinetics of Br^- oxidation is not a limiting step. As the scan potential becomes more positive, the electric field of the SCR is enhanced and the photocurrent increases; The $[Br^-]$ at the surface becomes lower than the bulk solution.

As the electric field of the SCR is strong enough to separate all the charges, all photo-holes are used to oxidize Br^-. For $U > U_{p,a}$, the photocurrent is controlled by both the mass

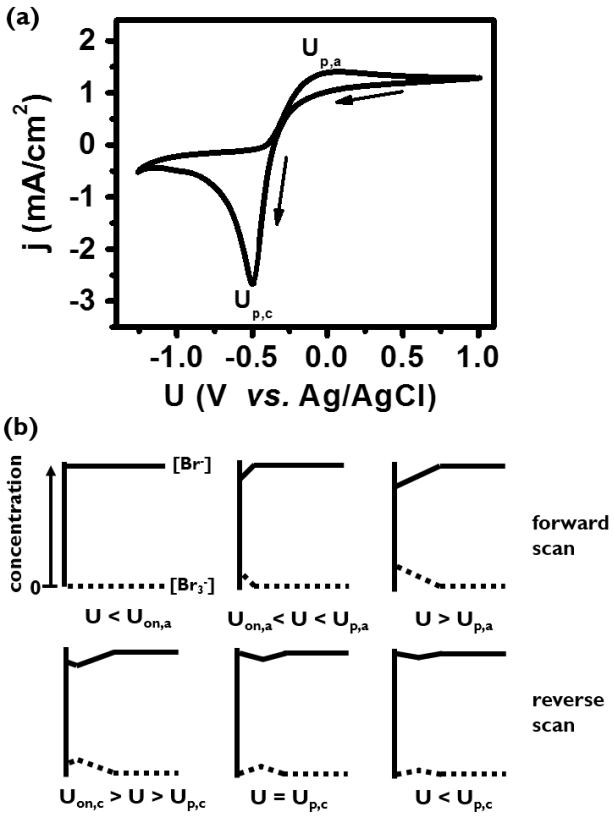

Figure 3.10: (a) a j-U plot of an n-GaN photoanode under illumination. Solution: 0.1 M HBr and 0.2 M Na_2SO_4; *v*: 100 mV/s. (b) $[Br^-]$ and $[Br_3^-]$ as a function of distance from the electrode surface under different conditions. $[Br_3^-]$ is multiplied by three for better visualization.

transport of [Br^-] and the concentration of photo-holes. The photocurrent decreases with increasing scan time because the concentration gradient of the [Br^-] at the surface decreases over time. The [Br^-] at the surface is not zero in our case. The concentration of photo-holes is not high enough to oxidize all the Br^- at the surface.

In the reverse scan, Br_3^- is reduced back to Br^- at the surface by electrons of the CB. Electrons of the VB cannot reduce Br_3^- due to the potential difference. At $U = U_{p,c}$, Br_3^- is fully consumed at the surface. For $U < U_{p,c}$, the cathodic current depends on the diffusion of Br_3^-. The current density as a function of scan time can be described by the Cottrell equation. As the CB bends upward, surface concentration of majority carriers increases. The availability of carriers is not a limiting step but the availability of oxidants, which is similar to the case of the metal/electrolyte interface.

For all the measurements in Chapter 4-Chapter6, weak UV illumination and high concentration of reducing agents (> 0.1 M) were used in the measurement. Therefore, the concentration of reducing reagents at the surface of the GaN electrode and in the bulk solution are the same. The j-U characteristic in the anodic scan is determined by the semiconductor physics; the electrochemistry at the interface is under kinetic control.

Figure 3.11 shows cyclic voltammograms (CV) of n-GaN under weak UV illumination. An aqueous solution of 0.1 M HBr + 0.2 M H_2SO_4 was used; the solution was not purged with N_2 before the measurements. The j-U curves were scanned continuously for 7 times. Each scan went first positive, reversed at U_j, as indicated in the figure, and then went negative. The subscript j indicates the scan sequence, ascending from 1 to 7. Two cathodic peaks, located at -0.47 V and -1.07 V, are observed in the reverse scans.

Under illumination of supra-bandgap light, photo-holes are generated and are drifted to the GaN surface by the electric field of the SCR. For U > -0.31 V, photo-holes oxidize reactants in the solution, resulting in the photocurrent. In the presence of Br^-, which is a strong reducing agent, photo-holes are predominately used to oxidize Br^- to Br_3^-. In the reverse scan, surface band bending reduces, and the concentration of electrons at the surface increases. For U < -0.32 V, Br_3^- is reduced back to Br^- by surface electrons, resulting in the cathodic peak at -0.47 V. As U scans more negative, the reduction peak

of O_2 is observed at -1.07 V. The reduction of protons starts for U > ~-1.15 V.

The inset of Figure 3.11 shows the maximum current density of the Br_3^- reduction peak ($j_{Br_3^-/Br^-}$) as a function of integrated anodic charge in each scan (Q_{anodic}). The scan rate and the scan step are 100 mV/s and 10 mV, respectively. Due to the difficulty of decoupling the reduction peak of Br_3^- and the reduction peak of O_2, $j_{Br_3^-/Br^-}$ is used here. The $|j_{Br_3^-/Br^-}|$ increases as the Q_{anodic} increases. This indicates that the reduction peak maximum is related to the quantity of Br_3^- which is oxidized in the anodic scan. For the scan reversed at U_7, the reduction peak of Br_3^- is barely observed. U_7 is more positive than the onset potential by only 0.02 V, very few Br_3^- are generated in the forward scan. When Br_3^- is generated in the anodic scan, Br_3^- starts to diffuse from the GaN surface. Therefore, not all Br_3^- can be reduced back to Br^-. This explains why the $j_{Br_3^-/Br^-}$-Q_{anodic} slope decreases when the U_j becomes more positive.

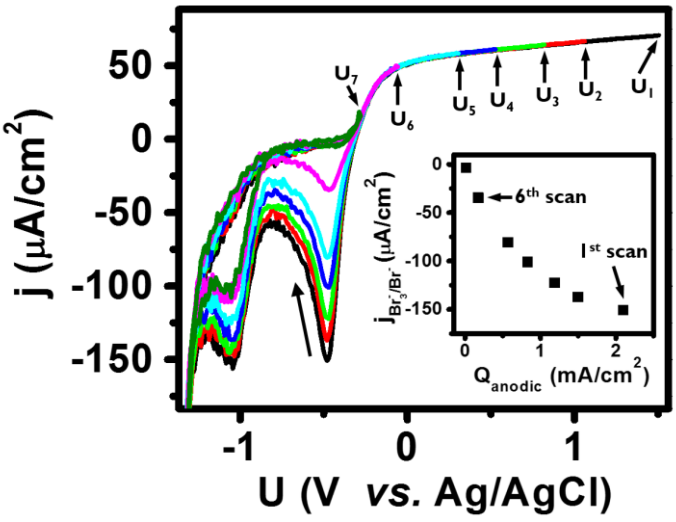

Figure 3.11: Cyclic voltammograms of n-GaN under illumination, which were scanned continuously for 7 times and were reversed at U_j at each scan. Subscript j denotes the scan sequence, ascending from 1 to 7. The inset shows the peak current of the Br_3^- reduction (U = ~-0.5 V) as a function of integrated anodic charge for each scan. Solution: 0.1 M HBr and 0.2 M Na_2SO_4; *v*: 100 mV/s.

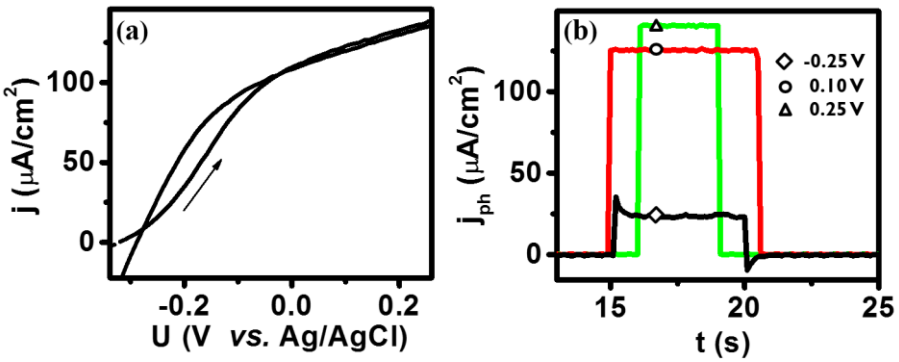

Figure 3.12: (a) A cyclic voltammogram of n-GaN under illumination. (b) Current density-time (j-t) plots of the n-GaN at different biases, which were first measured in the dark, then under illumination and finally in the dark. Solution: 0.1 M HBr and 0.2 M Na_2SO_4; *v*: 100 mV/s.

Since dissolved oxygen was not purged out of the solution before the measurements, the reduction peak of O_2 is observed in the cathodic scan, as is confirmed in scan 7. The current maximum of the oxygen reduction peak also increases with U_j. This indicates that not all photo-holes are used to oxidize Br^- and some of photo-holes oxidize water.

The cyclic voltammograms of the n-GaN photoanode in Figure 3.11 show the consistent photocurrent density in the forward scan and in the reverse scan. However, for some n-GaN samples, the photocurrent in the forward and in the reverse scan are different. Figure 3.12 (a) shows a cyclic voltammogram of an n-GaN under illumination in a solution of 0.1 M HBr and 0.2 M Na_2SO_4. The measurement was recorded at a scan rate of 100 mV/s. The onset potential is at ~-0.3 V and the plateau photocurrent is reached at ~0.0 V. For -0.3 V < U < 0.0 V, the photocurrent in the forward and reverse scan are different. This effect is not observed in the n-GaN sample in Figure 3.11. We do not know the crystalline quality difference between the n-GaN samples used in Figure 3.11 and Figure 3.12. Both samples have a comparable doping concentration (5×10^{18} cm^{-3}).

Figure 3.12 (b) shows the current density-time (j-t) plots of the n-GaN at different biases. The measurements were first performed in the dark, then under illumination and finally in the dark. The illumination was controlled by a shelter. For current biased at 0.10

V and 0.25 V, no current is observed in the dark. Once the sample is illuminated, the current increases sharply. The photocurrent at 0.25 V is higher than 0.10 V as a result of SCR expansion. After the light is shielded, the current drops sharply to zero. At -0.25 V, when the sample is illuminated, the current increases sharply and a current spike is observed. The photocurrent reaches the steady state after ~0.5 s. Once the light is sheltered, a cathodic current spike is observed. This current spike decays to zero after ~0.5 s. The transient current in the j-t measurement confirms that the photocurrent difference between the forward scan and the reverse scan in Figure 3.12 (a) is a time effect.

The transient effect in the j-U and j-t measurements have been reported for different photoanodes [30]-[33]. When the illumination intensity is suddenly increased, photo-holes can accumulate at the surface due to low kinetics of charge transfer to solution [32]. In the presence of Br^- in the solution and under weak UV illumination, Faradaic charge transfer should not be rate-limiting in our case. The charging of surface states or traps in the bulk can lead to the transient current [33]. Once photo-holes are suddenly present, electrons in traps may recombine with photo-holes efficiently, contributing to the transient current. Similarly, once photoexcitation stops, the process is reversed and negative transient current may be generated.

3.5 Study of n-GaN using impedance spectroscopy

3.5.1 An equivalent circuit for semiconductor/solution interface

The interface of an n-type semiconductor and solution contains resistance and capacitance components. Therefore, potential drops across the interface. The change of the potential and current may have a different time response. In this section, we use impedance spectroscopy to study these electrical components. Details of the impedance theory can be found in Ref [34]-[37].

Figure 3.13 shows an equivalent circuit for an electrochemical cell consisting of the n-type semiconductor/electrolyte interface. R_S includes the resistance of the metal contact, the semiconductor and the solution. R_{ct} is the resistance of charge transfer between the semiconductor to the solution. C_{sc} is the capacitance of the SCR of the semiconductor. It is important to note firstly that in the electrochemical cell, Ohmic contact to the semiconductor and Helmholtz layer of the solution also contribute a parallel pair of resistance and capacitance to the equivalent circuit [37]. However, the capacitance of the Ohmic contact is negligible when charge storage at the metal/semiconductor interface is few or the contact area is large enough, which is our case. The capacitance of the Helmholtz layer is negligible in the case of the semiconductor/solution interface since $C_{sc} << C_H$, as discussed earlier in Section 3.2.3. Therefore, the overall impedance (Z) of the circuit in Figure 3.13 can be described by

$$Z = R_s + \frac{1}{\frac{1}{R_{ct}} + i2\pi f C_{sc}} \tag{3.22}$$

where f is the modulated frequency during the impedance measurement. Z is a complex number containing a real component (Z') and imaginary component (Z''):

$$Z = Z' + iZ'' \tag{3.23}$$

Using Eq. (3.22), Z' and Z'' can be respectively described as

$$Z' = R_s + \frac{R_{ct}}{1 + 4\pi^2 f^2 {R_{ct}}^2 {C_{cs}}^2} \tag{3.24}$$

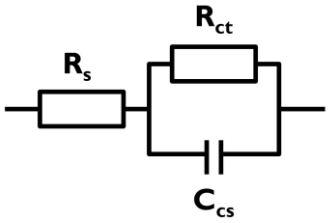

Figure 3.13: An equivalent circuit for an electrochemical cell consisting of a semiconductor/ solution interface. The components of the Helmholtz double layer are not included in the circuit.

$$Z'' = -\frac{2\pi f {C_{cs}} {R_{ct}}^2}{1+4\pi^2 f^2 {R_{ct}}^2 {C_{cs}}^2} \tag{3.25}$$

When the modulated frequency is extremely high ($f \to \infty$), the impedance of C_{sc} in Figure 3.13 ($=i/(2\pi f C_{cs})$) becomes zero, and $Z \to R_s$. For the other extreme case, when a very low frequency is applied ($f \to 0$), the impedance of C_{sc} becomes very large, and $Z \to R_s + R_{ct}$. In both cases, the imaginary part of the impedance becomes zero.

When electrons are depleted from the surface of an n-type semiconductor, the SCR is formed and the surface becomes positively charged. The charge of the SCR (Q_{sc}) is ascribed by immobile ionized donors. Considering an uniformly-doped n-type semiconductor, this charge is determined by the doping concentration (n_0) and the thickness of the SCR (W_{sc}), as described by

$$Q_{sc} = q n_0 W_{sc} \tag{3.26}$$

where q is the elementary charge. The capacitance density of the SCR (C_{sc}) is defined by $\frac{\mathrm{d}Q_{sc}}{\mathrm{d}U_{sc}}$, where U_{sc} is the potential drop over the SCR. Using Eq. (3.26), C_{sc} can be rewritten as

$$C_{sc} = q n_0 \frac{\mathrm{d}W_{sc}}{\mathrm{d}U_{sc}} \tag{3.27}$$

The capacitance of the SCR can also be described using a parallel plate model (Eq. (3.9)). After replacing the C_{sc} of Eq. (3.27) by Eq. (3.9) and substituting W_{sc} using Eq. (3.8), we can describe n_0 by

$$\frac{1}{n_0} = -q\varepsilon\varepsilon_0 \frac{1}{{C_{sc}}^3} \frac{\mathrm{d}C_{sc}}{\mathrm{d}U_{sc}} \tag{3.28}$$

Using $\frac{1}{{C_{sc}}^3}\frac{\mathrm{d}C_{sc}}{\mathrm{d}U_{sc}} = -\frac{1}{2}\frac{\mathrm{d}{C_{sc}}^{-2}}{\mathrm{d}U_{sc}}$, the carrier concentration can be described as

$$n_0 = \frac{2}{q\varepsilon\varepsilon_0 \frac{\mathrm{d}{C_{sc}}^{-2}}{\mathrm{d}U_{sc}}} \tag{3.29}$$

It is important to note again that here the C_{sc} is the capacitance density of the SCR. The deduction of Eq. (3.29) is described in Ref. [38] in detail.

According to Eq. (3.29), once $\frac{\mathrm{d}C_{sc}^{-2}}{\mathrm{d}U_{sc}}$ is known, the carrier concentration can be obtained. Therefore, it is useful to plot the C_{sc}^{-2} as a function of the U_{sc}, which is termed the Mott-Schottky plot. $\frac{\mathrm{d}C_{sc}^{-2}}{\mathrm{d}U_{b}}$ is the slope of the Mott-Schottky plot. For an n-type semiconductor whose doping is uniform all over SCR, the M-S plot is a linear line. In addition, from the Mott-Schottky plot, the flat-band potential (U_{fb}) can be obtained by an extrapolation of the C_{sc}^{-2}-U_{sc} line to the U_{sc}-axis. According to Eq. (3.8), when $U = U_{fb}$, W_{sc} becomes zero and C_{sc} becomes infinite. Therefore, $C_{sc}^{-2} = 0$ as $U_{sc} = U_{fb}$.

It is important to note that the change of the applied potential (ΔU) and the change of the potential over the SCR (ΔU_{sc}) can be different. The ΔU is larger than the ΔU_{sc} if the IR drop is large due to low solution conductivity, high resistivity of the semiconductor or in the presence of surface oxides or surface states. In Eq. (3.29), the U_{sc} can only be experimentally replaced by U when the ΔU predominately falls over the SCR.

3.5.2 Mott-Schottky plot

Figure 3.2 (b) shows the bandedge potential of an n-type semiconductor biased at the U_{fb}. The potential difference (Δ) between the CB edge potential (U_C) and Fermi-level potential (U_f) is determined by the carrier concentration (n_0), as described by

$$\Delta = U_C - U_f = \frac{kT}{q}\ln\left(\frac{n_0}{N_C}\right) \tag{3.30}$$

where k, q and T are the Boltzmann constant, the elementary charge unit and the absolute temperature, respectively. N_C is the effective density of states for the CB and is defined by [39]

$$N_C = \frac{2(2\pi m_e^* kT)^{3/2}}{h^3} \tag{3.31}$$

where m_e^* is the electron effective mass and h is the Planck's constant. For wurtzite n-GaN, $N_C \cong 4.3 \times 10^{14} \times T^{3/2}$ [40]. Once U_{fb} is known from the extrapolation of the Mott-Schottky plot, U_C can be obtained by $U_C = U_{fb} + \Delta$. Using Eq. (3.30), U_C can be calculated by

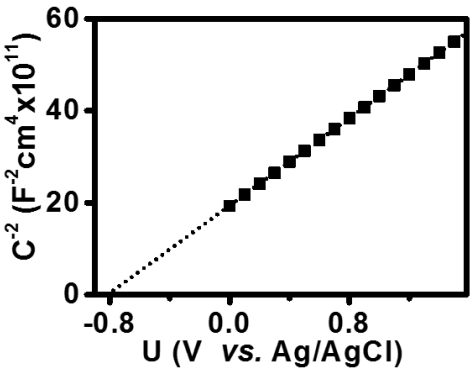

Figure 3.14: A Mott-Schottky plot of n-GaN in the dark.
Solution: 0.1 M HBr + 0.2 M Na_2SO_4.

$$U_C = U_{fb} + \frac{kT}{q}\ln\left(\frac{n_0}{N_C}\right) \tag{3.32}$$

Using the bandgap of n-GaN (E_g), U_V can be calculated by

$$U_V = \frac{E_g}{q} + U_C \tag{3.33}$$

Let's take a Mott-Schottky plot of n-GaN in the dark as an example, as shown in Figure 3.14. A solution of 0.1 M HBr + 0.2 M Na_2SO_4 was used during the measurement. The slope of this Mott-Schottky plot is 23.8×10^{11} $F^{-2}cm^4V^{-1}$. Using Eq. (3.29) and ε_{GaN} = 8.9 [40], the carrier concentration is calculated to be 5.2×10^{18} cm^{-2}. The U_{fb} of this n-GaN is -0.81 V. E_g of GaN is 3.42 eV [40]. Using Eq. (3.32) and Eq. (3.33), U_C and U_V are calculated to be -0.79 V and 2.63 V (vs. Ag/AgCl), respectively.

3.5.3 Redox potentials

Water splitting ($H_2O \leftrightarrow \frac{1}{2}O_2 + H_2$) by photoelectrolysis can be separated into two half reactions: hydrogen formation (Eq. (3.34)) and oxygen formation (Eq. (3.35)), as described by

$$2H^+ + 2e^- \leftrightarrow H_2 \tag{3.34}$$

$$H_2O + 2h^+ \leftrightarrow \frac{1}{2}O_2 + 2H^+ \tag{3.35}$$

The reduction potential ($U_{ox/red}$) of an electrochemical reaction is defined by the Nernst equation [9]:

$$U_{ox/red} = U^{\circ}_{ox/red} - \frac{RT}{n_e F}\ln K_{eq} \tag{3.36}$$

where *R*, *F* and *T* are the universal gas constant, the Faraday's constant and the absolute temperature. $U^{\circ}_{ox/red}$ is the reduction potential of the reaction under the standard condition. K_{eq} is the equilibrium constant of the chemical reaction. n_e is the number of electrons participating in the electrochemical reaction. In the case of proton reduction (Eq. (3.34)), two electrons are required to form one hydrogen. Therefore, the reduction potential of H^+/H_2 (U_{H^+/H^2}) can be described as

$$U_{H^+/H_2} = U^{\circ}_{H^+/H_2} - \frac{2.303\times 8.314\times 298}{2\times 96487}\log\frac{1}{[H^+]^2} \tag{3.37}$$

Here, the standard reduction potential for protons ($U^{\circ}_{H^+/H_2}$) is a potential reference for all electrochemical reactions in the solution and is set to be 0 V. Therefore, U_{H^+/H_2} can be written as

$$U_{H^+/H_2} = -0.059 \times \text{pH (V } \textit{vs.}\text{ SHE)} \tag{3.38}$$

where pH is defined as $\log\frac{1}{[H^+]}$.

Similarly, the formation of one oxygen requires four charges to transfer. The standard reduction potential of O_2/H_2O ($U^{\circ}_{H_2O/O_2}$) is 1.23 V. The reduction potential of O_2/H_2O is therefore defined as

$$U_{O_2/H_2O} = 1.23 - 0.059 \times \text{pH (V } \textit{vs.}\text{ SHE)} \tag{3.39}$$

It is important to note that the reduction potentials of protons and oxygen refer to the standard hydrogen electrode (SHE) as the potential reference. However, in this dissertation, a reference electrode of Ag/AgCl/3 M KCl was used. The potential relation between these two reference electrodes at the room temperature is: $U_{Ag/AgCl/3\ M\ KCl} = U_{SHE}$ + 0.210 V [41]. Therefore, these two reduction potentials as a function of pH can be

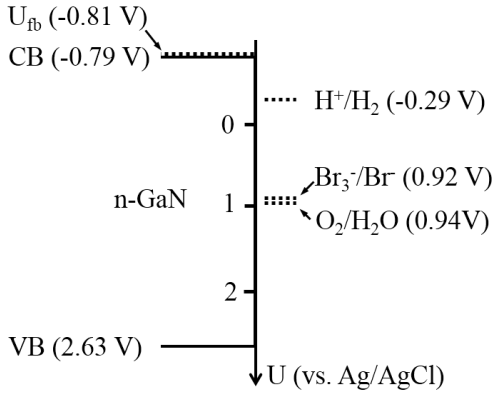

Figure 3.15: Bandedge potentials of n-GaN and reduction potentials of H^+/H_2, Br_3^-/Br^- and O_2/H_2O in the solution of 0.1 M HBr + 0.2 M Na_2SO_4 (pH = 1.4).

described as:

$$U_{H^+/H^2} = -0.210 - 0.059 \times \text{pH (V } vs. \text{ Ag/AgCl)} \quad (3.40)$$

$$U_{O_2/H_2O} = 1.019 - 0.059 \times \text{pH (V } vs. \text{ Ag/AgCl)} \quad (3.41)$$

Let's go back to the case in Figure 3.14. The solution of 0.1 M HBr + 0.2 M Na_2SO_4 was used in the measurement. pH of the solution was 1.4. Therefore, using Eq. (3.40) and Eq. (3.41), U_{H^+/H^2} = -0.29 V and U_{H_2O/O_2} = 0.94 V (*vs.* Ag/AgCl), respectively. The U_{fb} of this n-GaN is at -0.81 V (Figure 3.14). Using Eq. (3.32) and Eq. (3.33), U_C and U_V are calculated to be -0.79 V and 2.63 V (vs. Ag/AgCl), respectively. These values are in agreement with the reported U_C and U_V of n-GaN in Ref. [41],[42]. The reduction potential of Br_3^-/Br^- (Figure 3.9) is estimated to be the center of the Br_3^- peak and the Br^- peaks, which is 0.92 V. Consequently, the bandedge potentials of GaN at the flat-band condition relative to the reduction potential of H^+/H_2, Br_3^-/Br^- and O_2/H_2O can be constructed, as illustrated in Figure 3.15.

3.6 Photo-corrosion of n-GaN in Br^--containing solution

When supra-bandgap light illuminates n-GaN, photocarriers are generated. Photo-holes are drifted to the surface of the n-GaN layer. Besides carrier recombination and oxidation of solvated ions, photo-holes at the surface can also oxidize GaN, resulting in photo-corrosion. In an inert electrolyte (i.e. $Na_2SO_{4\,(aq)}$), water is oxidized at the surface of the photoanode during water photoelectrolysis. The oxidation of water has slow kinetics at the GaN surface. Therefore, when carrier recombination is suppressed, photo-corrosion of n-GaN is a predominate reaction instead of water oxidation [44]-[48]. Huygens et al. quantified the concentration of Ga ions dissolved in the solution after photoelectrochemical measurements. 84% and 98 % of photo-holes were found to corrode n-GaN in the measurements using H_2SO_4 and NaOH aqueous solution, respectively [48].

Therefore, addition of sacrificial reducing agents in the solution, which has strong reaction kinetics, is necessary to reduce photo-corrosion of GaN during photoelectrochemical characterization. A review of reducing agents for photoanodes is referred to Ref. [49]. Cl^- is an effective reducing agent and is commonly used in phototelectrolysis of n-GaN [50]-[52]. However, photo-corrosion of n-GaN is still observed after the measurements [53]-[55]. Minsky et al. reported that the etching rate of GaN was ~ 40 nm/min in a solution of HCl:H_2O (vol. 1:10) under illumination of 325 nm light (570 mW/cm^2) [53]. CH_3OH [56] and C_2H_5OH [57] have also been used as sacrificial reducing agents although photo-corrosion of n-GaN after the measurements was not qualitatively discussed in their works.

To further suppress photo-corrosion of n-GaN, in this dissertation, Br^- was used as the sacrificial reducing agent. Due to higher reaction kinetics, Br^- suppresses photo-corrosion of n-GaN more efficiently than Cl^- [55],[58]. Luo et al. [55] studied photo-corrosion of n-InGaN, which is less photo-stable than GaN, in a 1 M HCl solution and a 1 M HBr solution. The surface of the InGaN was characterized by the EDX before and after a chronoamperometric measurement. The EDX measurements show the atomic ratio of the indium decreases by 5% and 47% after the integrated charge of 3.6 C/cm^2 and 0.46 C/cm^2 in the HCl and HBr solution, respectively. The oxidation of Br^- is a hole-capture process

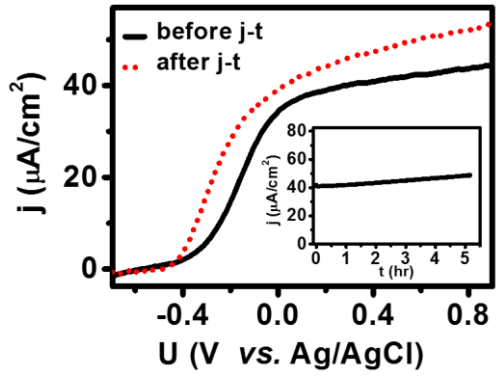

Figure 3.16: j-U plots of n-GaN under illumination before and after a chronoamperometric measurement. The inset shows the chronoamperogram of the n-GaN biased at 0.5 V for 5 hours. Solution: 0.1 M HBr + 0.2 M Na_2SO_4; *v*: 100 mV/s.

(Eq. (3.21)) and does not lead to photocurrent doubling (see Section 4.3). Br_3^-, as the oxidized product of Br^-, is highly dissolvable in the solution and therefore bubble formation at the surface of GaN can be avoided. Moreover, the intensity of the UV light for the illumination, was reduced in this work using an AM 1.5 filter, as mentioned in Section 2.3. In this case, the density of photo-holes at the GaN surface decreases; photo-corrosion rate of n-GaN decreases

Here, we compare the photoelectrochemical properties of n-GaN before and after a chronoamperometric measurement. A solution of 0.1 M HBr + 0.2 M Na_2SO_4 and weak UV illumination were used during the measurements. The photocurrent density-potential (j_{ph}-U) plot for a pristine n-GaN is shown in Figure 3.16 (solid line). Subsequently, the n-GaN was biased at 0.5 V for 5 hours under illumination, and the current density-time (j-t) plot is shown in the inset of Figure 3.16. The photocurrent at 0.5 V increases as a function of time, and becomes 19.4% higher at the end of the chronoamperogram. The integrated charge of the j-t plot is 0.83 C/cm^2. Afterwards, the photocurrent density as a function of potential was measured (dashed line). The plateau photocurrent of the n-GaN increases and the photocurrent onset shifts toward negative potential after the j-t measurement.

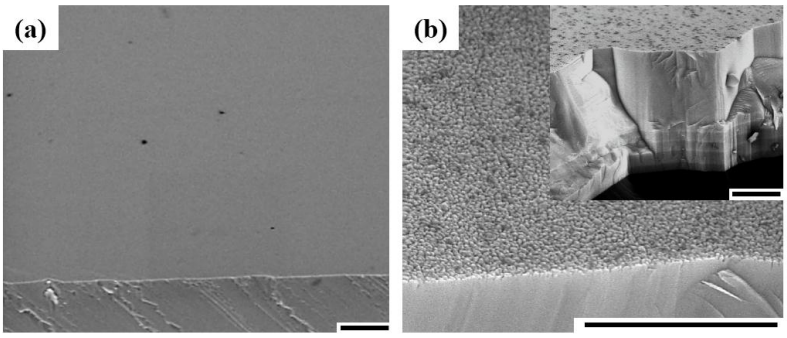

Figure 3.17: 45˚ SEM images of the n-GaN surface (a) before and (b) after the measurements in Figure 3.16. The inset shows the etched surface at a different scale. Scale bar: 1 μm.

The morphology of the n-GaN before and after the measurement were assessed by SEM, as indicated in Figure 3.17 (a) and (b) respectively. The pristine GaN layer is smooth (rms of the surface is 1.4 nm, assessed by a 10×10 μm^2 AFM scan). After the photoelectrochemical measurements, the surface of n-GaN was slightly corroded and becomes nanoroughened. Due to the surface nanoroughening, the total depletion area of the n-GaN increases. Better carrier separation and hole collection for the etched GaN may contribute to a higher plateau photocurrent with respect to the planar GaN. Moreover, the surface chemistry of GaN changes after photo-corrosion. At the etched surface, the formation of intermediate states which are required for Br^- oxidation may be favored, resulting in the negative shift of the onset potential (Figure 3.16).

We did not have the facilities to quantify the amount of dissolved ions in the solution. However, from the inset of Figure 3.16, we know the charge of 0.83 C/cm^2 was generated during the j-t measurement. A 390 nm-thick n-GaN layer can be fully oxidized using this charge if all photo-holes are dedicated to photo-corrosion of the n-GaN. However, from the SEM image, the surface is only slightly corroded. In this dissertation, for each n-GaN sample the anodic charge integrated from all photoelectrochemical characterizations, including cyclic voltammetry and chronoamperometry, is typically lower than 0.03 C/cm^2. Although the n-GaN is not completely free of photo-corrosion, the changes of photoelectrochemical properties and surface morphology are very minor in our work as

Br^- and the weak UV illumination are used.

3.7 References

[1] N. Sato, "Electrochemistry at Metal and Semiconductor Electrodes", Elsevier Science B. V. (1998).
[2] K. Seeger, "Semiconductor Physics: An Introduction", Springer (2004).
[3] C. Hamaguchi, "Basic Semiconductor Physics", Springer (2010).
[4] A. J. Bard and L. R. Faulkner, "Electrochemical Methods: Fundamentals and Applications", John Wiley & Sons (2001).
[5] P. P. Konorov, A. M. Yafyasov, V. B. Bogevolnov, "Field Effect in Semiconductor-electrolyte Interfaces: Application to Investigations of Electronic Properties of Semiconductor Surfaces", Princeton University Press (2006).
[6] W. Schmickler, "Interfacial Electrochemistry", Oxford University Press (1996).
[7] S. Srinivasan, "Fuel Cells: From Fundamentals to Applications", Springer (2006).
[8] S. J. Anz1, A. M. Fajardo1, W. J. Royea1, N. S. Lewis, A. J. Morris, "Semiconductor Photoelectrochemistry", John Wiley & Sons (2012).
[9] A. J. Bard, M. Stratmann, S. Licht, "Encyclopedia of Electrochemistry, Semiconductor Electrodes and Photoelectrochemistry", Wiley-VCH (2002).
[10] M. X. Tan, P. E. Laibinis, S. T. Nguyen, J. M. Kesselman, C. E. Stanton, and N. S. Lewis, *Prog. Inorg. Chemi.*, **41**, 21 (1994).
[11] I. M. Huygens, K. Strubbe, and W. P. Gomes, *J. Electrochem. Soc.*, **147**, 1797 (2000).
[12] R. Memming, "Semiconductor Electrochemistry", Wiley-VCH (2001).
[13] K. Rajeshwar, "Fundamentals of Semiconductor Electrochemistry and Photoelectrochemistry", Wiley-VCH (2007).
[14] W.W. Gartner, Phys. Rev. 116, 84 (1959).
[15] J. F. Muth, J. H. Lee, I. K. Shmagin, R. M. Kolbas, H. C. Casey, B. P. Keller, U. K. Mishra, and S. P. DenBaars, *Appl. Phys. Lett.*, **71**, 2572 (1997).
[16] K. Kumakura, T. Makimoto, N. Kobayashi, T. Hashizume, T. Fukui, and H. Hasegawa, *Appl. Phys. Lett.*, **86**, 052105 (2005).
[17] J. Reichman, *Appl. Phys. Lett.*, **36**, 574 (1980).
[18] C. T. Sah, R. N. Noyce, W. Shockley, *Proc. IRE*, **45**, 1228 (1957).
[19] Lewis, N. S., *Inorg. Chem.*, **44**, 6900 (2005).
[20] Gerischer, H., *J. Electroanal.Chem.*, **150**, 553 (1983).
[21] Lewis, N. S. *Acc. Chem. Res.*, **23**, 176 (1990).
[22] K. Rajeshwar, *Spectroscopy*, **8**, 16 (1993).
[23] R. N. Hall, *Phys. Rev*., **87**, 387 (1982).
[24] S. Schaefer, A. H. R. Koch, A. Cavallini, M. Stutzmann, and I. D. Sharp, *J. Phys. Chem. C*, **116**, 22281 (2012).
[25] Fujihara, K.; Ohno, T.; Matsumura, M. *J. Chem. Soc., Faraday Trans.*, **94**, 3705 (1998).
[26] G. Faita, G. Fior and T. Mussini, *Electrochim. Acta*, **13**, 1765 (1968).

[27] V. Vojinovic, S. Mentus, and V. Komnenic, *J. Electroanal. Chem.*, **547**, 109 (2003).
[28] Robert Owen Griffith, Andrew McKeown and Albert Gordon Winn, *Trans. Faraday Soc.*, **28**, 101 (1932).
[29] T. X. Wang, M. D. Kelley, J. N. Cooper, R. C. Beckwith, and D. W. Margerum, *Inorg. Chem.*, **33**, 5872 (1994).
[30] F. Le Formal, M. Gratzel and K. Sivula, *Adv. Funct. Mater.*, **20**, 1099 (2010).
[31] P. Iwanski, J. Curran, W. Gissler and R. Memming, *J. Electrochem. Soc.*, **128**, 2128 (1981).
[32] C. Sanchez, K. Sieber and G. Somorjai, *J. Electroanal. Chem.*, **252**, 269 (1988).
[33] M. Dareedwards, J. Goodenough, A. Hamnett and P. Trevellick, *J. Chem. Soc., Faraday Trans. 1*, **79**, 2027 (1983).
[34] J. R. MacDonald, "Impedance Spectroscopy: Emphasizing Solid Materials and Systems", John Wiley & Sons (1987).
[35] Mark E. Orazem, Bernard Tribollet, "Electrochemical Impedance Spectroscopy", Wiley (2008).
[36] L. Andrzej, "Electrochemical Impedance Spectroscopy and its Applications", Springer (2014).
[37] S. R. Morrison, "Electrochemistry at Semiconductor and Oxidized Metal Electrodes", Plenum Press (1980).
[38] J. D. Beach, *doctoral dissertation*, Colorado School of Mines (2002).
[39] S. M. Sze and K. K. Ng, "Physics of Semiconductor Devices", Wiley (2007).
[40] M. E. Levinshtein (ed.), S. L. Rumyantsev (ed.) and M. S. Shur (ed.), "Properties of Advanced Semiconductor Materials: GaN, AIN, InN, BN, SiC, SiGe", John Wiley & Sons, (2001).
[41] Metrohm, Metrosensor electrodes. http://www.metrohm.cz/Download/8.000.5037EN_elektrody.pdf
[42] K. Fujii, M. Ono, T. Ito, Y. Iwaki, A. Hirako, and K. Ohkawa, *J. Electrochem. Soc.*, **154**, B175 (2007).
[43] J. D. Beach, R. T. Collins, and J. A. Turner, *J. Electrochem. Soc.*, **150**, A899 (2003).
[44] D. Zhuang and J. H. Edgar, *Materials Science & Engineering R-Reports*, **48**, 1 (2005).
[45] K. Fujii, T. Ito, M. Ono, Y. Iwaki, T. Yao, and K. Ohkawa, *Phys. Status Solidi C*, **4**, 2650 (2007).
[46] M.S. Minsky, M. White, E.L. Hu, *Appl. Phys. Lett.*, **68**, 1531 (1996).
[47] L. Macht, J. J. Kelly, J. L. Weyher, A. Grzegorczyk, and P. K. Larsen, *J. Cryst. Growth*, **273**, 347 (2005).
[48] I. M. Huygens, K. Strubbe, and W. P. Gomes, *J. Electrochem. Soc.*, **147**, 1797 (2000).
[49] X. B. Chen, S. H. Shen, L. J. Guo, and S. S. Mao, *Chem. Rev.*, **110**, 6503 (2010).
[50] K. Fujii, M. Ono, Y. Iwaki, K. Sato, K. Ohkawa, and T. Yao, *J. Phys. Chem. C*, **114**, 22727 (2010).
[51] W.-H. Tu, Y.-K. Hsu, C.-H. Yen, C.-I. Wu, J.-S. Hwang, L.-C. Chen, and K.-H. Chen, *Electrochem. Commun.*, **13**, 530 (2011).
[52] J. Li, J. Y. Lin, and H. X. Jiang, *Appl. Phys. Lett.*, **93**, 162107 (2008).

[53] M.S. Minsky, M. White, E. L. Hu, *Appl. Phys. Lett.*, **68**, 1531 (1996).
[54] E. D. Haberer, R. Sharma, C. Meier, A. R. Stonas, S. Nakamura, S. P. DenBaars, and E. L. Hu, *Appl. Phys. Lett.*, **85**, 5179 (2004).
[55] W. Luo, B. Liu, Z. Li, Z. Xie, D. Chen, Z. Zou, and R. Zhang, *Appl. Phys. Lett.*, **92**, 262110 (2008).
[56] K. Fujii, K. Sato, T. Kato, K. Koike, and T. Yao, *Phys. Status Solidi C*, **6**, S627 (2009).
[57] D. F. Wang, A. Pierre, M. G. Kibria, K. Cui, X. G. Han, K. H. Bevan, H. Guo, S. Paradis, A. R. Hakima, and Z. T. Mi, *Nano Lett.*, **11**, 2353 (2011).
[58] A. Ennaoui and H. Tributsch, *J. Electroanal. Chem.*, **204**, 185 (1986).

CHAPTER 4

Nanoroughened n-GaN photoanodes by dry etching

Chapter 4. Nanoroughened n-GaN photoanodes by dry etching

4.1. Introduction

Under illumination, the n-GaN photoanode absorbs supra-bandgap light and generates electrons and holes. Space charge region (SCR) plays an important role in charge separation. Surface nanostructuring can increase the surface area of the electrode, and therefore enlarges depletion area. The improved charge separation increases the number of photo-holes at the surface [1]. Photo-holes generated in charge-neutral region of n-GaN mainly recombine with electrons if they cannot reach the SCR. The diffusion distance for photo-holes in the charge-neutral region to the SCR is significantly reduced in the nanostructures as compared to a planar structure. Furthermore, the abundant reactive sites at the nanostructured surface may facilitate charge transfer at the solution/semiconductor interface [2]. For the oxidation of water, each intermediate state has a characteristic activation energy which may depends on the crystal plane [3]. By revealing particular crystal facets at the GaN nanostructure, the charge transfer efficiency could be improved. Different nanostructure architectures such as nanopillars [4], nanowires [5] and pyramid stripes [6] have been constructed at the GaN surface. These GaN nanostructures are commonly synthesized by molecular beam epitaxy (MBE) or are grown selectively on patterned templates.

Surface nanostructuring can be alternatively achieved by dry etching technologies, which could be more advantageous in morphology control over the bottom-up strategies. Taking advantage of anisotropy in etching, nanostructures of high aspect ratio can be achieved by dry etching methods [7],[8]. Using proper mask technology, the dimensions and topography of the nanostructures can be designed and fabricated after considering the influence of light absorption, charge transfer and electric resistivity [9],[10].

However, the photoelectrochemical properties of GaN nanostructures fabricated by dry etching have been rarely investigated [11]. Benton *et al.* [11] reported the plateau

photocurrent of the GaN light-emitting diodes (LED) after the surface roughening using dry etching is increased by 6 times. However, the LED stack used in their work consists of a p-GaN layer, multiple InGaN/GaN quantum wells and an n-GaN layer, which strongly complicates the discussion. The p-n junction of GaN and InGaN/GaN quantum well structure are both reported unfavorable for photo-holes to reach the surface because of improper band bending [12],[13]; therefore, the plateau photocurrent decreases with respect to an n-GaN photoanode. It is very possible that, after the formation of the pillar array, photo-holes accumulating inside the (In)GaN layers reach the surface through the wall of the pillars; therefore the photocurrent is increased.

In order to investigate the photoelectrochemical properties of n-GaN after surface roughening, in this chapter, we nanoroughened a GaN epilayer into a pillar array by dry etching, using a self-assembled Ni cluster mask. The GaN pillars of 0.4-1.6 μm in height were prepared and were investigated photoelectrochemically. After the nanoroughening, the surface area increases up to 6 times and the plateau photocurrent is increased by 84% with respect to planar GaN. The process of the surface nanoroughening is firstly introduced, followed by the photoelectrochemical characterizations of the GaN pillars. Subsequently, the impedance and photoluminescence measurements of the GaN pillars are presented to discuss plasma-induced surface damage of n-GaN. Some results of this chapter are published in Ref. [14].

4.2. Process description: pillars at different heights

A GaN (0001) layer was epitaxially grown on a Si substrate by metal organic chemical vapor deposition (MOCVD) [15]. For high-n-type GaN samples, the top 2 μm of the n-GaN layer is highly Si-doped, followed by the unintentionally-doped (UID) GaN and AlGaN buffer layers. The electron concentration of the n-GaN and the UID GaN layer are respectively 5×10^{18} cm^{-3} and 5×10^{16} cm^{-3}, assessed by Hall measurements. The full width at half maximum (FWHM) of the GaN X-ray diffraction measurement (Panalytical, Philips) is 450 and 600 arc second for the (0002) and ($10\bar{1}2$) reflection, respectively.

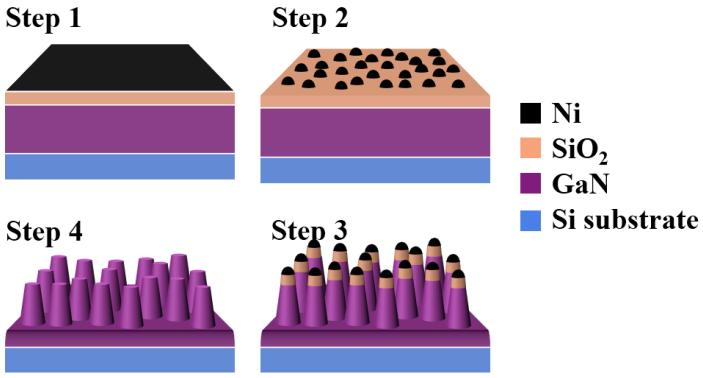

Figure 4.1: Fabrication steps of GaN nanopillars by dry etching from a planar GaN using self-assembled Ni clusters as mask. Step1: SiO_2 layer and Ni film deposition, Step 2: Ni clusters by agglomeration anneal, Step 3: nanopillars by dry etching of SiO_2 and GaN and Step 4: wet etching of the Ni and SiO_2.

Figure 4.1 illustrates the fabrication steps of the GaN nanopillars by inductively coupled plasma (ICP) dry etching (Plasma Lab 100, Oxford) using a self-assembled Ni cluster mask [16]. After the GaN epitaxy, a 250 nm SiO_2 layer and a 15 nm Ni film were deposited on the GaN by PECVD (Plasmalab 100, Oxford) and sputtering (Spider 630, Pfeiffer), respectively. The samples were subsequently annealed at 850°C in N_2 environment for 90 seconds to transform the Ni film into the Ni nanoclusters. The Ni cluster pattern was subsequently transferred to the SiO_2 layer using a SF_6-based ICP dry etching with an etching rate of 50 nm/min. The etching parameter of the SiO_2 etch was: RF power/ICP power/SF_6 flow/ O_2 flow/chamber pressure/temperature/time: 50 W/300 W/ 100 sccm/10 sccm/10 mtorr/20 ˚C/7.5 mins. Then, a Cl_2-based ICP dry etching was used to etch the GaN layer with an etching rate of 400 nm/min. The Ni and SiO_2 islands were the mask during the GaN etch. The etching parameter of the Cl_2 etch was: RF power/ICP power/Cl_2 flow/Ar flow/chamber pressure/temperature: 100 W/200 W/ 50 sccm/20 sccm/5 mtorr/20 ˚C. Finally, the remaining Ni clusters and SiO_2 were respectively removed by HNO_3 (vol. 7%) solution at 70 ˚C and BHF [17] at room temperature, resulting in the GaN nanopillars.

Figure 4.2 (a) shows the SEM image of the surface of the pristine GaN epilayer. The rms of the surface is 1.4 nm, assessed by a 10×10 μm^2 AFM scan. Figure 4.2 (b)-(d) show the SEM images of the 1.6 μm GaN pillars recorded at different magnifications and angles. The pillars are uniformly distributed with an average density of 3.0 ± 0.4 $\times 10^8$ cm^{-2}, evaluated from top-view SEM images (areal size > 21×22 μm^2). The effective surface area enhancement (*AE*) of the pillars, estimated from the SEM images, increases linearly with the pillar height (*H* in μm), plotted in Figure 4.2 (e); Its relation can be fitted by the equation: $AE = SA(H)/SA(0) = 1.0 + 3.5 \times H$, where *SA(H)* and *SA(0)* are the

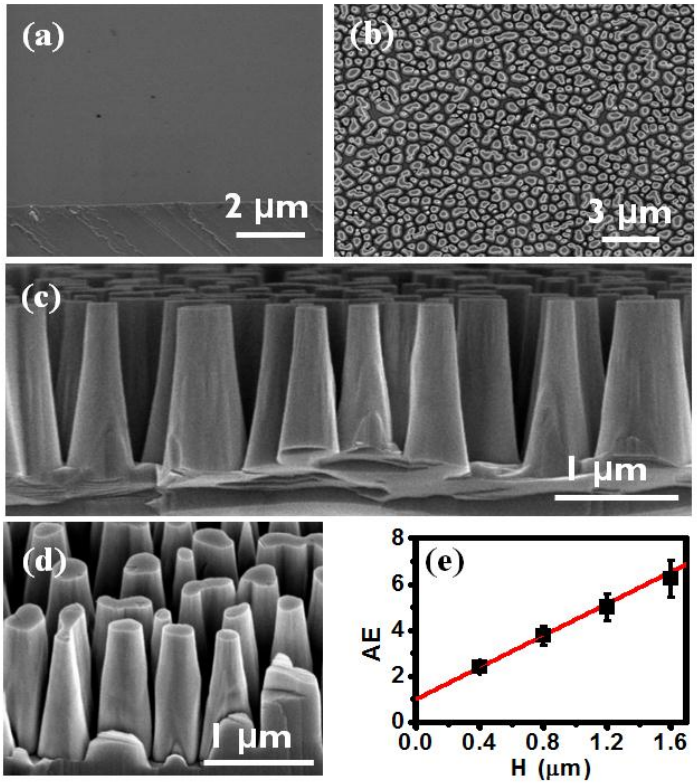

Figure 4.2: SEM images of the GaN pillar array. (a) Planar GaN epilayer before the surface roughening (rms = 1.4 nm for 10×10 μm^2). The morphology of the 1.6 μm high pillars imaged at different angles: (b) top view, (c) 85˚ and (d) 45 ˚. (e) The dependence of the pillar height (*H* in μm) and the effective surface area enhancement (*AE*): $AE = 1.0 + 3.5 \times H$.

surface area of the GaN pillars and planar GaN, respectively. The *AE* increases up to 6 times for the 1.6 μm high pillars.

4.3. Photoelectrochemical properties of GaN pillars

In this section, the photoelectrochemical properties of the n-GaN pillars are discussed. An aqueous solution of 0.1 M HBr + 0.2 M Na_2SO_4 was used for the measurements. A Xe lamp with an AM 1.5 filter was used as the light source. The projected light intensity at the sample surface was 63 mW/cm^2, measured by a thermopile detector. The details of the light source are referred to Section 2.3.

Figure 4.3 (a) shows the current density (j) as a function of the applied potential (U) for the n-GaN before and after the nanostructuring. In the dark, no anodic current was observed (< 50 nA/cm^2) for all GaN samples; a cathodic current was observed for U < -0.4 V as a result of the reduction of oxygen in the solution. The oxygen was dissolved from ambient air.

Under illumination, photocarriers are generated and contribute to the photocurrent. The photocurrent onset potential (U_{onset}: j > 4 μA/cm^2) and the open circuit voltage (U_{ocp}) of planar n-GaN are at -0.30 V and -0.45 V, respectively. For planar GaN, the photocurrent plateau is reached for U > 0.00V. Between the photocurrent onset and plateau (-0.30 V < U < 0.00 V), electrons and photo-holes are partly separated by the electric field of the space charge region (SCR), and carrier recombination is still influential. In the photocurrent plateau region, all photo-holes are separated and the carrier recombination in the SCR is fully suppressed. Photo-holes at the GaN surface oxidize Br^- to Br_3^-, as described by Eq. (3.21).

The pillar samples all show a similar U_{onset} (~-0.32 V) and U_{ocp} (~-0.38 V). The photocurrent plateau for the pillars all starts from ~ 0.25 V on. The potential difference between the current onset and plateau ($\Delta U_{onset\text{-}plateau}$) for the pillars are ~ 0.6 V, which is larger than that of planar GaN (~0.3 V). This implies carrier recombination is enhanced for the pillars with respect to planar GaN. As a consequence, a larger electric field is needed to suppress the carrier recombination in the SCR.

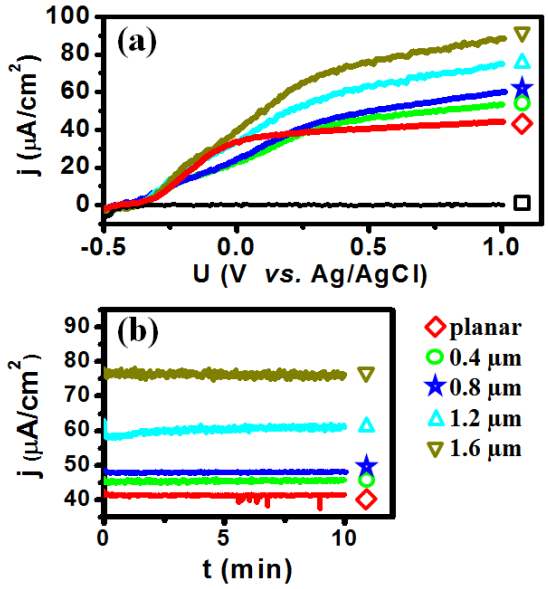

Figure 4.3: (a) Current-potential (j-U) plots of the planar n-GaN and the n-GaN pillars. The black curve (□) is the dark current of the planar GaN, and the other curves were measured under illumination. Solution: 0.1 M HBr + 0.2 M Na_2SO_4; *v*: 100 mV/s. (b) Current-time (j-t) plots of the n-GaN samples (U_{GaN-RE} = 0.5 V).

To investigate the stability of the photocurrent, the photocurrent density (U_{WE-RE} = 0.5 V) as a function of time for the planar GaN and the GaN pillars were measured for 10 mins, as shown in Figure 4.3 (b). For the GaN samples, the photocurrents were all stable. This confirms the effectivity of Br^- as the hole scavenger. The plateau photocurrents of the 1.2 μm and 1.6 μm high pillars are increased by 47% and 84% with respect to planar GaN, respectively.

Here, it is worth noting that the plateau photocurrent is independent of the concentration of Br^- and the agitation of the solution, but is dependent of the light intensity. Figure 4.4 (a) shows the j-t plots of planar n-GaN under illumination of different light intensities. The photocurrent was biased at the plateau (U_{WE-RE} = 0.5 V). The plateau photocurrent density increases linearly with the light intensity, shown in Figure 4.4 (b). This confirms that the electrochemical oxidation of Br^- at the GaN surface is a kinetically-

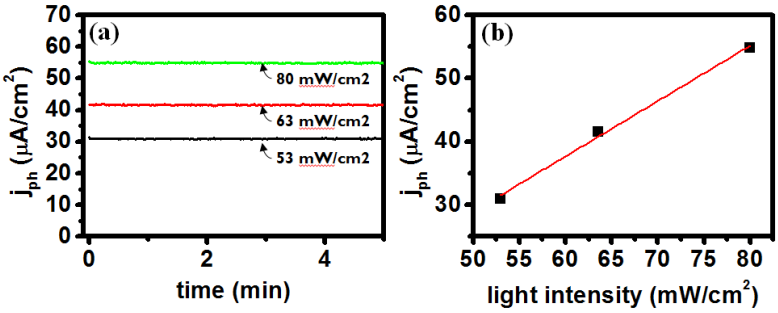

Figure 4.4: (a) j-t plots of planar GaN under illumination of different light intensities and (b) the plateau photo-current density *vs.* the light intensity. Solution: 0.1 M HBr + 0.2 M Na_2SO_4; $U_{GaN\text{-}RE}$ = 0.5 V.

controlled reaction; the photocurrent is limited by the photon flux incident on the surface of the samples.

Moreover, photocurrent multiplication was not observed in the measurements using the Br^--containing solution. Figure 4.6 (a) shows the j-U plots of planar GaN in aqueous solutions of 0.1 M HBr + 0.2 M Na_2SO_4 (pH = 1.4) and 1 M HCl (pH = 0) under illumination. The U_{onset} measured in these two solution are different, resulting from the change of the reactants and the pH. The n-GaN photoanode generates similar photocurrent densities in these two solutions (Figure 4.6(b)). Cl^- is often used as a hole scavenger to enhance photostability of n-GaN, and does not contribute to photocurrent multiplication [18]. Consequently, the oxidation of Br^- is a pure hole capture process.

Figure 4.5 illustrate the schematics of the depletion region in the planar GaN and the GaN pillars. The flat-band potential (U_{fb}) of the n-GaN epilayer in this work is -0.81 V, determined by the Mott-Schottky plot in Section 4.4. At the photocurrent plateau ($U_{WE\text{-}RE}$ = 0.5 V), the depletion width is calculated to be only 16 nm in our highly n-doped GaN layer. Under illumination, UV light is mostly absorbed within the first 100 nm from the surface due to the high absorption coefficient of GaN ($\alpha = 10^5$ cm^{-1} [19]). Some photocarriers generated in the charge-neutral area can reach the depletion region considering the diffusion length of the minority carriers (200-250 nm) [20]. However, carrier recombination in the charge-neutral region is inevitable.

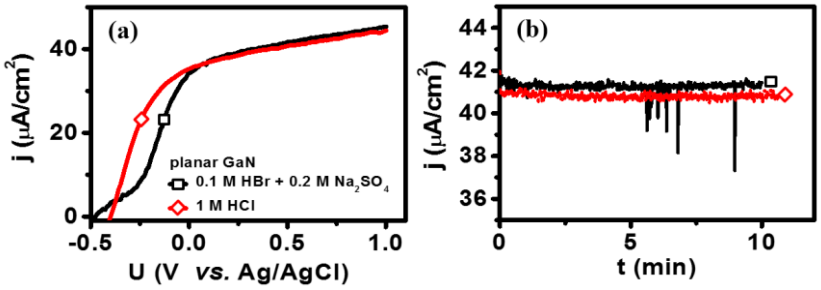

Figure 4.5: (a) j-U plots and (b) j-t plots ($U_{GaN\text{-}RE}$ = 0.5 V) for planar GaN in aqueous solutions of 0.1 M HBr + 0.2 M Na_2SO_4 (pH = 1.4) and 1 M HCl (pH = 0) under illumination. *v*: 100 mV/s.

Due to the surface enhancement, the pillar structure provides a much larger volume of depletion region as compared to the planar GaN. In addition, the charge-neutral region of the pillars is surrounded by the depletion region. The radius of the pillars in this work is between 250 nm to 450 nm, which is comparable to the diffusion length of photo-holes. Consequently, photo-holes in the GaN pillars are more probable to reach the depletion region before carrier recombination occurs. Hence, the number of photo-holes at the surface of the GaN pillars is higher than that of the planar GaN, resulting in the increased photocurrent.

Figure 4.6: Schematics of depletion region, diffusion region and bulk in the planar GaN and the GaN pillars. At $U_{GaN\text{-}RE}$ = 0.5 V, the depletion width is calculated to be 16 nm. The diffusion length of minority carrier is 200-250 nm. The penetration depth of supra-bandgap light from the surface is ~100 nm ($\alpha = 10^5$ cm^{-1}).

4.4. Impedance properties of GaN pillars

In this section, we characterized the n-GaN pillars of different height (0.4-1.6 μm) by electrochemical impedance spectroscopy (EIS). The measurements were performed in an aqueous solution of 0.1 M HBr + 0.2 M Na_2SO_4 (pH = 1.4) in the dark. The solution was not agitated. No evident anodic leakage current is observed for all the samples. The recorded j-U plots of the planar GaN and the GaN samples in the dark are shown in Figure 4.7. The measurement noise becomes dominant for $j < 1$ μA/cm^2. The dark current for the planar and pillar samples can therefore not be distinguished. The applied potential in the EIS measurements started from 1.25 V to -0.25 V. The AC frequency was modulated from 10 kHz to 500 Hz; an AC potential of 0.1 V was applied for each scan.

Figure 4.8 shows the Nyquist plots of the planar GaN and the GaN pillars biased at 0.5 V. The scales of Z' axis and Z'' axis are the same for better visualization. The Z' and Z'' values were normalized using the projected working area of the electrodes. No second semicircle was observed for all Nyquist plots. The resistance and capacitance of the Helmholtz double layer were therefore not included in the equivalent circuit. The Nyquist plots were fitted using a $R_s(R_{ct}C_{cs})$ model (inset of Figure 4.8 (a)). The "goodness of fit" (χ^2) [23] is less than 0.03 for all the fittings. The R_s is the overall series resistance including the resistance of the Ohmic contact, the n-GaN and the solution. The R_{ct} is the resistance of the interfacial charge transfer over the solution/n-GaN interface. The C_{cs} is

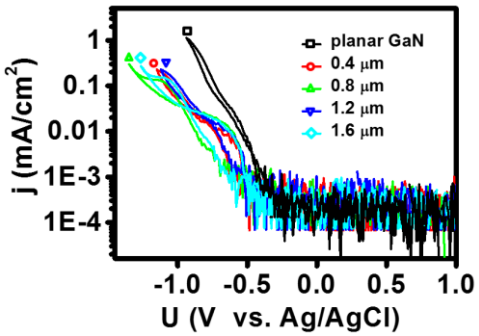

Figure 4.7: j-U plots in the dark for the planar GaN and the GaN pillars. Solution: 0.1 M HBr + 0.2 M Na_2SO_4; v = 100 mV/s

the capacitance of the SCR of the n-GaN. Details of the equivalent circuit are described in Section 3.5.1. The R_s increases after the surface roughening as a result of the damaged surface and the reduced thickness of the n-GaN layer in the pillar structure. The R_{ct} of the measured pillar structures are all much smaller than planar GaN as a result of increased surface area.

The Mott-Schottky (M-S) plots of the planar GaN and the GaN pillars are presented in Figure 4.9 (a). The M-S plot for planar GaN (inset of Figure 4.9) has the highest M-S slope (2.38×10^{12} $F^{-2}cm^4V^{-1}$). The slope decreases with increasing pillar height (down to 1.04×10^{11} $F^{-2}cm^4V^{-1}$ for the 1.6 μm high pillars). The C_{sc} here was normalized using the projected area of the electrodes. The C_{sc}^{2-} decreases with increasing pillar height as a result of the increased effective surface area.

The surface area enhancement of the pillars has been estimated by the SEM images. The area enhancement as a function of the pillar height is shown in Figure 4.2 (e). Therefore, the C_{sc} normalized by the effective surface area of the samples can be obtained and the M-S plots are presented in Figure 4.9 (b). The M-S slope of planar GaN is constant for all the potential range. For all the pillar samples, a constant M-S slope is found for U > ~ 0.5 V, and a smaller non-constant M-S slope is observed for U < ~0.5 V. The change

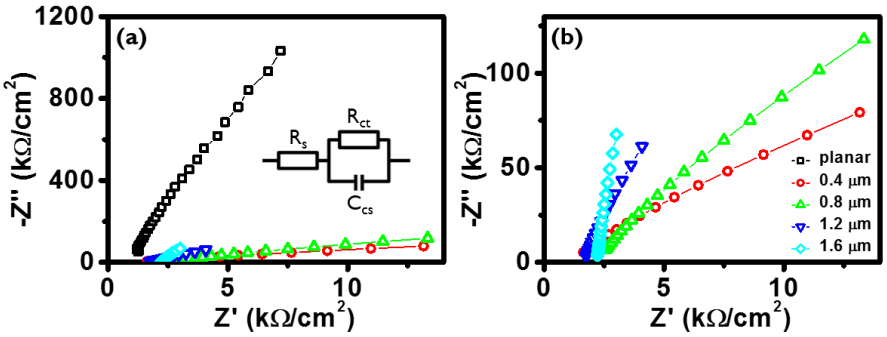

Figure 4.8: (a) Nyquist plots of the planar n-GaN and the n-GaN pillars in the dark ($U_{GaN\text{-}RE}$ = 0.5 V) and (b) the Nyquist plots at a different scale. The inset shows the equivalent circuit. Each impedance was normalized using the projected area of the electrode. Solution: 0.1 M HBr + 0.2 M Na_2SO_4; frequency range: 10 kHz - 500 Hz; AC potential: 0.1 V.

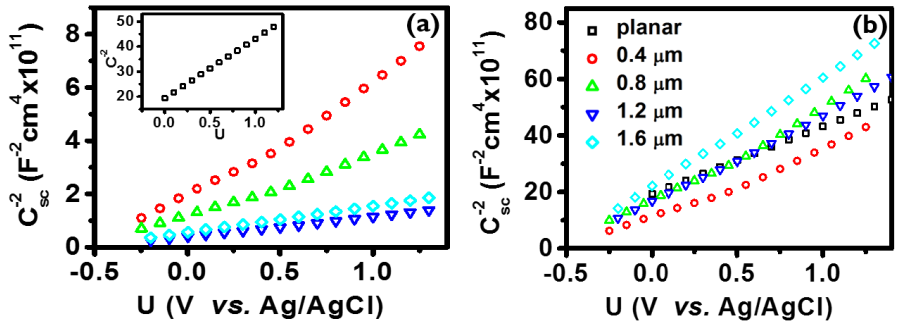

Figure 4.9: Mott-Schottky (M-S) plots of the planar GaN and the GaN pillars, where the C_{sc} was normalized (a) using the projected area of the electrode and (b) using the effective surface area of the electrode evaluated by the SEM images (Figure 4.2 (e)).

of the M-S slope becomes less different when the pillar height increases. We believe, for the GaN pillars, the change of the M-S slope results from quasi Fermi-level pinning by the plasma-induced surface states, which will be discussed later.

In Figure 4.9 (b), for U > 0.6 V, the M-S plots of the pillars are approximately parallel. This shows that the effective surface areas of the pillars were properly assessed by the SEM images. However, the M-S slope of planar GaN is evidently smaller than that of the pillars. In addition to surface area, the M-S slope is also influenced by carrier concentration (Eq. (3.29)). As mentioned earlier, ion bombardment during dry etching damages the surface of n-GaN. The introduction of donor-like defects or acceptor-like defects can therefore change the carrier concentration [21],[22], and may lead to the difference of the M-S slopes between the planar GaN and the GaN pillars.

To facilitate the discussion, we normalized the M-S slopes of the GaN samples to that of the 1.6 μm-high pillars (1.04×10^{11} $F^{-2}cm^4V^{-1}$). The slope-normalized M-S plots are presented in Figure 4.10. For the pillars ≥ 1.2 μm in height, the M-S line for U > ~0.4 V and U < ~0.0 V is characterized by two similar and constant slopes, separated by the M-S line with a smaller and non-constant slope. For the pillars ≤ 0.8 μm in height, a linear M-S relation is observed for U > ~0.5 V; the M-S slope becomes non-constant and smaller for U < ~0.5 V.

We believe, for the GaN pillars, the change of the M-S slopes for U < ~0.5 V results from quasi Fermi-level pinning by the dry etching-induced surface states. A simple case is used to illustrate the role of surface defects in the M-S plot, as shown in Figure 4.11. Here we assume there are monoenergetic surface states at the surface of an n-type semiconductor. The energetic position of the surface states is lower than the CB edge by E_{ss}. We also assume that the potential change across the Helmholtz double layer is ignorable, and the applied potential only falls across the SCR or at the surface traps. The Helmholtz double layer with a layer thickness, d, is formed at the surface of the semiconductor. x' and μ are the width of the SCR and the energy difference between the Fermi level and the CB edge, respectively. The charge of the donor-like surface states and acceptor-like surface states are denoted by Q_D and Q_A, respectively.

When the electrode is biased negatively, the Fermi-level moves upward. Before the Fermi-level reaches the energy level of the surface states, the applied potential falls only across the SCR of the semiconductor. A linear M-S relation can be obtained for the uniformly doped n-type semiconductor (Eq. (3.29)). When the Fermi-level reaches the

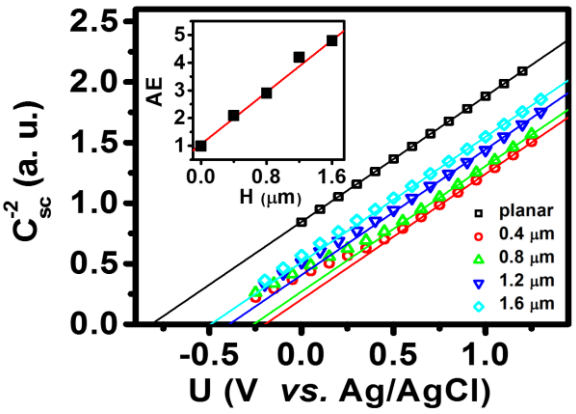

Figure 4.10: M-S plots of the planar GaN and the GaN pillars, where all the M-S slopes were normalized to that of the 1.6 μm high pillars (1.04 $\times 10^{11}$ $F^{-2}cm^4V^{-1}$). Inset shows the effective surface area enhancement (*AE*) of the samples as a function of the pillar height (*H* in μm): $AE = 1 + 2.4 \times H$. The *AE* is obtained under assumption of the same carrier concentration for all samples.

energy level of the surface states, electrons start to occupy the empty surface states. The Fermi level is pinned at these traps. A horizontal M-S plot is therefore observed as a consequence that the capacitance of the SCR is independent of the potential change. The linear M-S slope is only observed again when the surface states are completely filled, and the applied potential falls across the SCR again. The potential used to occupy all the acceptor-like surface states is $-Q_A/C_d$, resulting in the shift from U_{fb} to U'_{fb}. Similarly, the detrapping of the surface states happens when the Fermi-level moves downward and reaches the energy of the occupied surface states. The potential required to completely deplete the surface states is $+Q_D/C_d$, resulting in the shift from U_{fb} to U''_{fb}.

We did not observe the horizontal M-S relation, as shown in Figure 4.11 (b), for the GaN pillars. We believe that in our case the Fermi-level may be only partially pinned by the surface traps, or the surface traps may be not monoenergetically distributed, which is

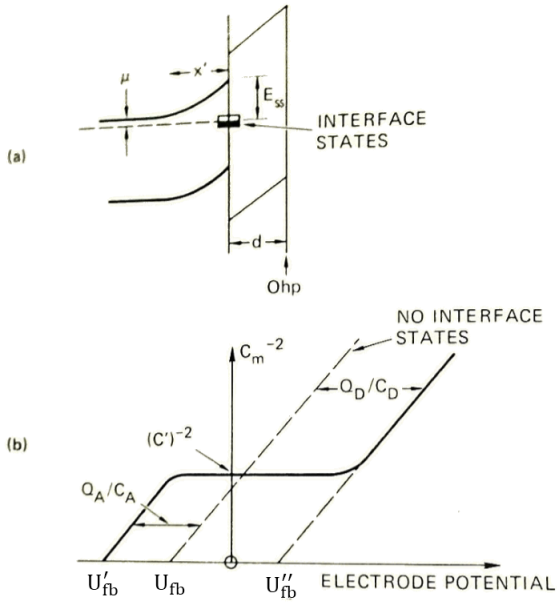

Figure 4.11: (a) A band diagram of an n-type semiconductor/liquid interface with monoenergetic surface states. (b) A M-S plot of the semiconductor influenced by the charging and discharging of the surface states [24].

different from the. To avoid the increase of cathodic current, the impedance was not measured for U < -0.25 V. Therefore, the linear M-S relation for U < 0.00 V is less explicit for the pillar shorter than 1.2 µm. However, for the pillars higher than 1.2 µm, the parallel shift of the M-S line between 0.00 V and 0.40 V is clearly observed. The potential shift of the M-S plot is higher with decreasing pillar height, which indicates that the surface damage is stronger in this case.

Furthermore, the surface damage also has a distinct impact on the U_{fb} of the GaN pillars. Before the discussion of the U_{fb}, it is important to point out that the presence of the donor-like or acceptor-like surface traps can offset the U_{fb}, as discussed in Figure 4.11 (b). However, the characterization metrologies for the species and the density of the surface traps are not available in this work [21],[22]. Therefore, we only used the linear extrapolation of the M-S plots for U > ~0.6 V to determine the U_{fb} of the pillars, as shown in Figure 4.10. The U_{fb} of planar GaN is -0.81V. The U_{fb} of the 0.4 µm high pillars shifts toward more positive by 0.62 V with respect to the planar GaN. With increasing pillar height, the U_{fb} of the pillars becomes more negative, but the U_{fb} of the pillars are all more positive than the unetched GaN. During dry etching, the GaN at the bottom between pillars is damaged most because ions bombard the surface perpendicularly. The pillar wall receives less damage, since the surface is more parallel to the direction of the ion bombardment. When the pillar height increases, the surface area of the highly-damaged GaN over the total surface area decreases. Therefore, the U_{fb} shifts more negative with increasing pillar height.

We can use the M-S plots in Figure 4.10 to evaluate the effective surface area of the GaN pillars. The effective surface area enhancement (*AE*) of the GaN pillars with respect to planar GaN is defined by

$$AE(H) = \frac{SA(H)}{SA(0)} \tag{4.1}$$

where *SA(H)* is the effective surface area of the pillars at a pillar height (*H*), and *SA(0)* is the surface area of planar GaN. By assuming that, for the planar GaN and all the GaN pillars, the carrier concentration as a function of depth from the surface is the same, Eq. (3.29) for the pillar sample and planar GaN can be expressed by

$$\frac{1}{AE(H)^2\frac{\mathrm{d}C_{SC}(H)^{-2}}{\mathrm{d}U}} = \frac{1}{\frac{\mathrm{d}C_{SC}(0)^{-2}}{\mathrm{d}U}} \tag{4.2}$$

Therefore, the *AE* of the pillars can be described by

$$AE(H) = \sqrt{\frac{\mathrm{d}C_{SC}(0)^{-2}/\mathrm{d}U}{\mathrm{d}C_{SC}(H)^{-2}/\mathrm{d}U}} \tag{4.3}$$

The inset of Figure 4.10 shows the *AE-H* plot for the GaN samples, obtained using Eq. (4.3). The *AE-H* relation can be fitted by: $AE = 1.1 + 2.3 \times H$. The *AE-H* relation evaluated by the M-S plots is comparable to that evaluated by the SEM images (Figure 4.2 (e)) although the former slope is slightly smaller than the later slope. These two approaches give an approximated effective surface area for the GaN pillars. However, to determine the *AE* precisely, the other characterization methodologies are required. For the *AE-H* plots evaluated by SEM images, a larger estimation error of the surface area is expected. For the *AE* plots evaluated by the M-S plots, carrier concentration is presumed the same for all samples, which is not true.

In the end of this section, it is important to note that in the equivalent circuit surface states typically contribute to a resistance (R_{ss}) and a capacitance (C_{ss}) in series, as shown in Figure 4.12 [25]-[27]. However, because of the large resistance density of charge transfer, R_{ct}, we did not observe the influence of the R_{ss}-C_{ss} component in the Nyquist plots (Figure 4.8 (b)) although they probably exist in the circuit. In the dark under reverse bias, the R_{ct} of the n-GaN/solution interface is typically over 100 M Ω /cm^2 for a planar n-GaN. Therefore, the curve of parallel R_{ct} and C_{sc} dominate in the Nyquist plots of n-GaN.

Moreover, as described above, surface damage is distributed non-uniformly at the GaN pillars. Therefore, the measured Nyquist plot of the pillars is contributed by numerous different R_{ct}, C_{sc} and R_s. However, in the section, the Nyquist plot was only fitted using a single $R_s(R_{ct}C_{sc})$ model. Therefore, the fitted parameters do not reflect the real impedance property of the GaN pillars in this work. However, we can still qualitatively discuss the influences of the pillar height and the surface damage on the impedance properties of the GaN electrodes.

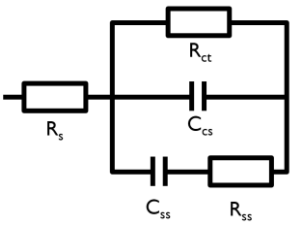

Figure 4.13: An equivalent circuit for the semiconductor/liquid interface in the presence of surface states [25]. The definitions of the symbols are given in the text.

4.5. Photo-stabilty of GaN pillars

To examine the photo-stability of the n-GaN pillar photanodes, the 1.6 µm high pillars have been biased at U = 0.5 V for 5 hours under illumination of the Xe light source filtered by the AM 1.5 filter, which has been used for this chapter. The inset of Figure 4.13 shows the j-t plot of the chronoamperometric measurement. The total charge transfer under the j-t plot is 1.37 C/cm^2. The solution was stirred by a rotating magnetic rod. The j_{ph} increases by 6.8% from initial 73 µA/cm^2 to 78 µA/cm^2 after the measurement. The j-U

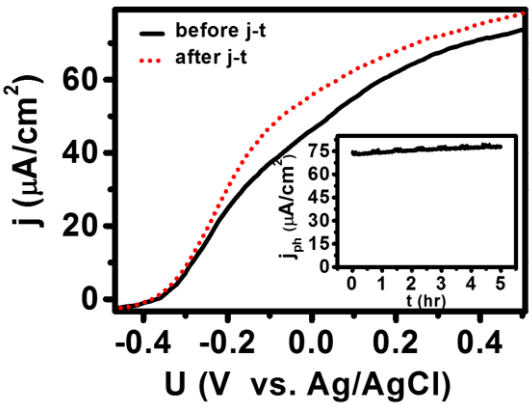

Figure 4.12: j-U plots of n-GaN pillars under illumination before and after a chronoamperometric measurement. The inset shows the chronoamperogram of the pillars biased at 0.5 V for 5 hours. Solution: 0.1 M HBr + 0.2 M Na_2SO_4; *v*: 100 mV/s.

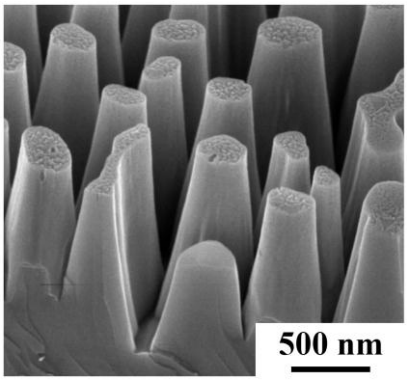

Figure 4.14: A 45° SEM image of the n-GaN pillars after the measurements in Figure 4.12.

curves before and after the j-t measurement are shown in Figure 4.13. The U_{onset} of the pillars before and after the j-t measurement are the same. The j_{ph} at U = 0.5 V increases by 6% after the j-t measurement.

The morphology of the GaN pillars after the measurements have been assessed by SEM (see Figure 4.14). No evident corrosion is observed at the surface of the pillar walls. In contrast, the top plane (0001) of the pillars is slightly corroded. We do not have a solid explanation for this phenomenon, but we suspect it to be due to different photo-stability for different GaN surface orientations. To our knowledge, no studies are available to show the dependence of photo-corrosion on different GaN surface orientations in the solutions containing Br^-.

The introduction of Br^-, as a hole scavenger in the solution, combined with low UV light intensity have successfully reduced the photo-corrosion of n-GaN during the photoelectorchemical measurements. We do not know the individual effect of the light intensity and Br^- on photo-corrosion of the pillars. However, we do expect photo-corrosion to be evidently enhanced when the light intensity is higher than a certain value (certainly happens when the j_{ph} > diffusion-limited current density of Br^- oxidation). When the light intensity increases, more photocarriers appear at the surface of the GaN pillars. If the surface concentration of photo-holes is too high to be efficiently consumed

by the oxidation of Br^-, photo-holes accumulating at the surface can participate in other reactions such as photo-corrosion of GaN.

4.6. Photoluminescence properties of pillars

The surface damage of the n-GaN pillars is discussed in this section using photoluminescence (PL) measurements. Firstly, carrier recombination mechanisms are briefly introduced. Subsequently, the PL spectra of n-GaN and UID GaN which are etched blankly or into pillar array are discussed.

4.6.1. Minority carrier lifetime

Under illumination, the n-type semiconductor absorbs supra-bandgap light, and generates photocarriers. Excess carriers tend to recombine so that the equilibrium state can be reached. Under constant illumination, when the steady-state condition is reached, the recombination rate of excess carriers is equal to photocarrier generation rate. The recombination of excess carriers can be categorized into radiative recombination and non-radiative recombination. Details of carrier recombination theory can be found in Ref. [28]-[30]. The following discussion is based on an n-type semiconductor.

The radiative recombination process is a direct recombination between an electron and a hole, emitting a photon. Exciton states or energetic levels of dopants may be involved in the transition process [31]-[33]. The minority carrier lifetime for radiative recombination (τ_{rad}) at steady state can be expressed by [28]

$$\frac{1}{\tau_{rad}} \approx R_{re} n \tag{4.4}$$

where R_{re} and n are the recombination coefficient and the electron concentration of the n-type semiconductor, respectively.

A semiconductor always contains a certain degree of structural defects, and these defects form energy levels in the bandgap of the semiconductors [34],[35]. In the presence of energy levels in the bandgap, electrons and holes can recombine through a multi-step

transfer. During the process of recombination, the energy is typically released in the form of phonons. Therefore, this type of defect-assisted recombination is called non-radiative recombination. The non-radiative recombination happening in the bulk of the semiconductor is named the Shockley-Read-Hall (SRH) recombination; the recombination at the surface of the semiconductor is named surface recombination [28],[36]. The carrier lifetime for the SRH recombination (τ_{SRH}) and surface recombination (τ_s) can be expressed by [28]

$$\frac{1}{\tau_{SRH}} \approx N_{bt} v_p \sigma_p \tag{4.5}$$

$$\frac{1}{\tau_s} \approx N_{st} v_p \sigma_p \tag{4.6}$$

where v_p, σ_p, N_{st} and N_{bt} are the hole thermal velocity, the hole capture cross section, the density of bulk traps associated with the carrier recombination and the density of surface trapping centers, respectively. The minority carrier lifetime in Eq. (4.5) and Eq. (4.6) depends on the trap density, but are independent of carrier concentration of the semiconductor which is not the case in Eq. (4.4). Due to a large lattice and thermal mismatch between the GaN layer and substrate, GaN grown by heteroepitaxy is well known to have a high defect density (see Section 1.4.2) [37]-[39].

In some cases the recombination energy is not released by photon emission but is transferred to a third charge carrier. This third carrier later on becomes thermalized through phonon emission. This non-radiative process is named Auger recombination, and the carrier lifetime (τ_{Auger}) can be expressed by [28]

$$\frac{1}{\tau_{Auger}} \approx A_{agur} n^2 \tag{7}$$

where A_{auger} is the Auger coefficient. Because the $1/\tau_{Auger}$ is proportional to the square of *n*, this process becomes dominant at a high concentration of excess carriers. However, at low-level injection of excess carriers in GaN (i.e. the PL measurement of bulk GaN), the Auger recombination is ignorable since the Auger coefficient is relatively too small [40],[41].

Consequently, the overall carrier lifetime in the PL measurements of bulk GaN at low light intensity injection can therefore be described by

$$\frac{1}{\tau} = \frac{1}{\tau_{rad}} + \frac{1}{\tau_{SRH}} + \frac{1}{\tau_s} \quad (8)$$

4.6.2. Photoluminescence of plasma-damaged n-GaN

Figure 4.15 (a) shows the PL spectra of planar n-GaN (n = 5×10^{18} cm^{-3}) and the n-GaN pillars at the near-bandedge (NBE) transition [39], measured at room temperature. The pillar height varies from 0.4 to 1.6 μm. The planar n-GaN and the n-GaN pillars are the same as the samples used in the photoelectrochemical measurements in Section 4.3. The fabrication details of the GaN pillars are described in Section 4.2. The luminescence properties of GaN has been reviewed in Ref. [39]. For planar GaN, the interference fringes are observed in the PL spectrum (Figure 4.15 (a)), which is ascribed by the Fabry-Pérot interference [42]. Due to the difference of the refractive index of GaN (n_{GaN} = 2.3) and air (n_{air} = 1), the critical angle of total internal reflection is only 23° at the air/GaN interface. Therefore, the light generated in the GaN cavity may undergo several internal reflection before it escapes. The transmission of the light is determined by the wavelength of the light, the cavity thickness and the interfacial reflectivity [42]. The strong Fabry-

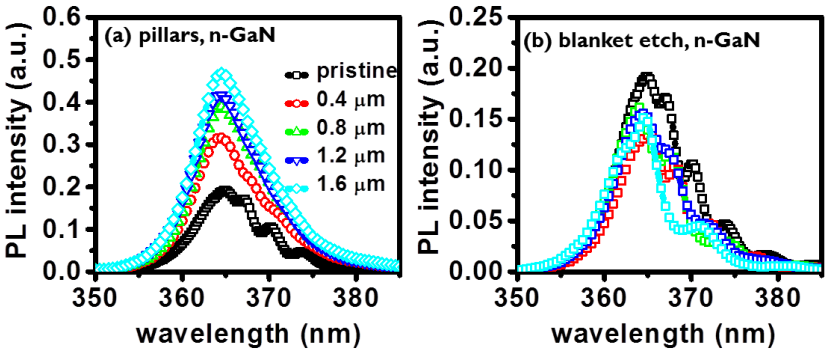

Figure 4.15: Near-bandedge (NBE) photoluminescence (PL) spectra of (a) n-GaN pillars and (b) blanket-etched n-GaN (5×10^{18} cm^{-3}), measured at room temperature. The etched depth of the samples varies from 0.4 μm to 1.6 μm.

Pérot interference for the PL spectrum of planar GaN confirms the smoothness of the GaN epilayer.

For the n-GaN pillars, the NBE PL peak intensity increases with increasing pillar height (Figure 4.15 (a)). The PL peak intensity of the 1.6 μm high pillars is higher by a factor of 2.4 than planar n-GaN. Due to the small total reflection angle, the light extraction efficiency at the planar n-GaN is limited. The nanopillar array provide abundant interfaces. Therefore, more light can come out and the PL intensity increases [43].

In order to exclude the light extraction effect, the blanket-etched n-GaN for different etch depths were fabricated. The GaN epilayer was etched without the Ni and SiO_2 mask, and was etched using the same etching recipe as the pillars in Figure 4.15 (a). The NBE PL spectra of the blanket-etched n-GaN are shown in Figure 4.15 (b). The Fabry-Pérot interference was observed in all the PL spectra of the samples. This indicates that the GaN samples were uniformly etched and the etched surface is still smooth.

The PL intensities of the blanket-etched n-GaN become 15 - 30% lower than the unetched n-GaN. As mentioned in Section 4.6.1, the PL emission is the result of the competition between radiative and non-radiative recombination. The radiative recombination rate is proportional to the carrier concentration of the GaN, but the non-radiative recombination rate is independent of the carrier concentration. Due to the high doping concentration of the n-GaN, the radiative recombination is very fast. Even though the surface damage promotes the surface recombination, the radiative recombination, resulting in the PL emission, can be still a relatively dominant process for photo-holes. Therefore, the PL intensities of the blanket-etched n-GaN are only slightly lower than the unetched GaN.

4.6.3. Photoluminescence of plasma-damaged UID GaN

To suppress the radiative recombination, an UID GaN epilayer ($n = 5 \times 10^{16}$ cm^{-3}) was chosen for the pillar etch and the blanket etch. The samples were fabricated using the same recipes as the n-GaN samples in Figure 4.15 (a) and Figure 4.15 (b). The NBE PL spectra of the UID GaN pillars are presented in Figure 4.16 (a). The PL peak intensity of

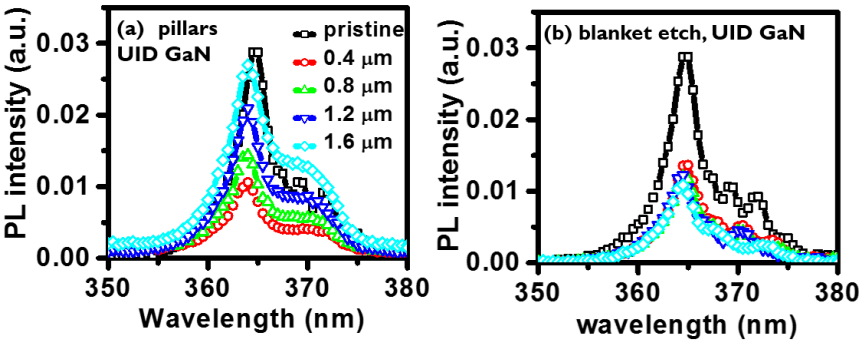

Figure 4.16: NBE PL spectra of (a) UID GaN pillars and (b) blanket-etched UID GaN (5×10^{16} cm^{-3}), measured at room temperature. The etched depth of the samples varies from 0.4 μm to 1.6 μm.

the unetched UID GaN is lower than the unetched n-GaN by a factor of 6.6, which confirms that the radiative recombination is significantly suppressed in the UID GaN. The NBE PL intensity of the 0.4 μm high UID GaN pillars is ~66% lower than unetched UID GaN. The PL intensity increases with increasing pillar height due to improved light extraction. The PL intensity of the 1.6 μm high UID GaN pillars becomes comparable with planar UID GaN. The NBE PL spectra of the blanket-etched UID GaN are presented in Figure 4.16 (b). The PL peak intensities of the blanket-etch UID GaN are independent of the etch depth and are all ~50% lower than the unetched UID GaN.

When the radiative recombination is suppressed, the surface damages show clearly distinct impact on the PL intensities of the UID GaN samples. During dry etching process, ion bombardment damages the surface, leaving the surface with abundant surface states [44],[45]. These surface states serve as the recombination centers and enhance the surface recombination velocity; the PL intensity decreases.

4.7. Summary

In this chapter, the GaN nanopillars were fabricated by dry etching of an n-GaN epilayer, using self-assembled Ni clusters as a mask. The properties of these nanopillars were studied using photoelectrochemical measurements, EIS measurements and PL

measurements. Charge separation in the GaN nanopillars is enhanced due to the abundant SCR. The enlarged SCR also improves the extraction of photo-holes from the charge-neutral region. Therefore, the number of photo-holes at the electrode surface is increased. The plateau photocurrent is enhanced by 84% for the 1.6 μm high pillars with respect to the planar GaN.

However, ion bombardment during dry etching damages the surface of the GaN pillars; therefore a larger $\Delta U_{onset\text{-}plateau}$ is required. The positive shift of the U_{fb}, obtained from the M-S plots, results in a weaker band bending for the pillars. The promoted non-radiative recombination reduces the lifetime of photo-holes, concluded from the PL measurements. The minimization of the surface damage is therefore important for the GaN pillars fabricated by dry etching technology.

4.8. References

[1] J. M. Spurgeon, H. A. Atwater, and N. S. Lewis, *J. Phys. Chem. C*, **112**, 6186 (2008).
[2] H. Kato, K. Asakura, A. Kudo, *J. Am. Chem. Soc.*, **125**, 3082 (2003).
[3] P.-T. Chen, C.-L. Sun, and M. Hayashi, *J. Phys. Chem. C*, **114**, 18228 (2010).
[4] Y. J. Hwang, C. H. Wu, C. Hahn, H. E. Jeong, and P. D. Yang, *Nano Lett.*, **12**, 1678 (2012).
[5] C. Pendyala, J. B. Jasinski, J. H. Kim, V. K. Vendra, S. Lisenkov, M. Menon, and M. K. Sunkara, *Nanoscale*, **4**, 6269 (2012).
[6] I. Waki, D. Cohen, R. Lal, U. Mishra, S. P. DenBaars, and S. Nakamura, *Appl. Phys. Lett.*, **91**, 093519 (2007).
[7] M. J. de Boer, J. G. E. Gardeniers, H. V. Jansen, E. Smulders, M. J. Gilde, G. Roelofs, J. N. Sasserath, and M. Elwenspoek, *J. Microelectromech. Syst.*, **11**, 385 (2002).
[8] H. V. Jansen, M. J. de Boer, S. Unnikrishnan, M. C. Louwerse, and M. C. Elwenspoek, *J. Micromech. Microeng.*, **19**, 033001 (2009).
[9] T. Richter, H. Lueth, R. Meijers, R. Calarco, and M. Marso, *Nano Lett.*, **8**, 3056 (2008).
[10] J. Wallys, J. Teubert, F. Furtmayr, D. M. Hofmann, and M. Eickhoff, *Nano Lett.*, **12**, 6180 (2012).
[11] J. Benton, J. Bai, and T. Wang, *Appl. Phys. Lett.*, **102**, 173905 (2013).
[12] K. Fujii, M. Ono, Y. Iwaki, K. Sato, K. Ohkawa, and T. Yao, *J. Phys. Chem. C*, **114**, 22727 (2010).
[13] K. Fujii, S. Nakamura, S. Yokojima, T. Goto, T. Yao, M. Sugiyama, and Y. Nakano, *J. Phys. Chem. C*, **115**, 25165 (2011).

[14] W. J. Tseng, D. H. van Dorp, R. R. Lieten, B. Mehta, P. M. Vereecken, and G. Borghs, *ECS Electrochem. Lett.*, **2**, H51 (2013).
[15] K. Cheng, M. Leys, S. Degroote, M. Germain, and G. Borghs, *Appl. Phys. Lett.* **92**, 192111 (2008).
[16] Q. Wang, J. Bai, Y. P. Gong, and T. Wang, *J. Phys. D:Appl. Phys.*, **44**, 395102 (2011).
[17] Buffered HF contains 6:1 volume ratio of $NH_4F_{(aq)}$ (vol. 40%) and $HF_{(aq)}$ (vol. 49%). Honeywell, Buffered oxide etchants. https://www.honeywell-pmt.com/sm/em/common/documents/Buffered_Oxide_Etchants.pdf
[18] Huygens, I. M., Strubbe, K., and Gomes, W. P., *J. Electrochem. Soc.*, **147**, 1797 (2000).
[19] J. F. Muth, J. H. Lee, I. K. Shmagin, R. M. Kolbas, H. C. Casey, B. P. Keller, U. K. Mishra, and S. P. DenBaars, *Appl. Phys. Lett.*, **71**, 2572 (1997).
[20] K. Kumakura, T. Makimoto, N. Kobayashi, T. Hashizume, T. Fukui, and H. Hasegawa, *Appl. Phys. Lett.*, **86**, 052105 (2005).
[21] W. Gotz, N. M. Johnson, H. Amano, and I. Akasaki, *Appl. Phys. Lett.*, **65**, 463 (1994).
[22] J. Oila, J. Kivioja, V. Ranki, K. Saarinen, D. C. Look, R. J. Molnar, S. S. Park, S. K. Lee, and J. Y. Han, *Appl. Phys. Lett.*, **82**, 3433 (2003).
[23] χ^2 of 10^{-4}, 10^{-2} and 10^{-1} approximately corresponds to a 1%, 10% and 30% difference between the measured and fitted impedances. Gamry Instruments, Equivalent Circuit Modeling. http://www.gamry.com/application-notes/equivalent-circuit-modeling-using-the-gamry-eis300-electrochemical-impedance-spectroscopy-software/
[24] S. R. Morrison, "Electrochemistry at Semiconductor and Oxidized Metal Electrodes," Plenum press (1980).
[25] G. Nagasubramanian, B. L. Wheeler, G. A. Hope, and A. J. Bard, *J. Electrochem. Soc.*, **130**, 385 (1983).
[26] F. Cardon, *Physica*, **57**, 390 (1972).
[27] W. P. Gomes and D. Vanmaekelbergh, *Electrochim. Acta*, **41**, 967 (1996).
[28] S. M. Sze and K. K. Ng, "Physics of Semiconductor Devices," Wiley Interscience (2007).
[29] K. Seeger, "Semiconductor Physics: An Introduction", Springer (2004).
[30] C. Hamaguchi, "Basic Semiconductor Physics", Springer (2010).
[31] A. K. Viswanath, J. I. Lee, S. Yu, D. Kim, Y. Choi, and C. H. Hong, *J. Appl. Phys.*, **84**, 3848 (1998).
[32] S. C. Jain, M. Willander, J. Narayan, and R. Van Overstraeten, *J. Appl. Phys.*, **87**, 965 (2000).
[33] B. Monemar, P. P. Paskov, J. P. Bergman, A. A. Toropov, T. V. Shubina, T. Malinauskas, and A. Usui, *Phys. Status Solidi B*, **245**, 1723 (2008).
[34] D. Segev and C. G. Van de Walle, *Europhys. Lett.*, **76**, 305 (2006).
[35] J. Y. Chen, C. J. Pan, and G. C. Chi, *Solid-State Electron.*, **43**, 649 (1999).
[36] D. E. Aspnes, *Surf. Sci.*, **132**, 406 (1983).
[37] K. J. Lee, E. H. Shin, and K. Y. Lim, *Appl. Phys. Lett.*, **85**, 1502 (2004).
[38] L. Liu and J. H. Edgar, *Mat. Sci. Eng. R*, **37**, 61 (2002).
[39] M. A. Reshchikov and H. Morkoc, *J. Appl. Phys.*, **97**, 061301 (2005).

[40] A. Laubsch, M. Sabathil, J. Baur, M. Peter, and B. Hahn, *IEEE Trans. Electron Devices*, **57**, 79 (2010).
[41] Y. C. Shen, G. O. Mueller, S. Watanabe, N. F. Gardner, A. Munkholm, and M. R. Krames, *Appl. Phys. Lett.*, **91**, 141101 (2007).
[42] S.G. Lipson, H. Lipson, and D.S. Tannhauser, "Optical Physics" Cambridge University Press (1995).
[43] Y. D. Wang, S. J. Chua, S. Tripathy, M. S. Sander, P. Chen, and C. G. Fonstad, *Appl. Phys. Lett.*, **86**, 071917 (2005).
[44] H. W. Choi, S. J. Chua, A. Raman, J. S. Pan, and A. T. S. Wee, *Appl. Phys. Lett.*, **77**, 1795 (2000).
[45] J. M. Lee, K. M. Chang, S. W. Kim, C. Huh, I. H. Lee, and S. J. Park, *J. Appl. Phys.*, **87**, 7667 (2000).

CHAPTER 5

Plasma-induced surface damage reduction

Chapter 5. Plasma-induced surface damage reduction

5.1 Introduction

In the previous chapter, we have demonstrated that the photoactivity of the n-GaN photoanode can be enhanced after surface nanoroughening by dry etching. The plateau photocurrent is increased by 84 % for the 1.6 μm high pillars with respect to the planar n-GaN a result of improved carrier separation [1]. However, surface damage is introduced during dry etching and promotes surface recombination. A larger potential is required to suppress carrier recombination.

To further improve the photoelectrochemical properties of the GaN pillars, it is necessary to reduce the surface damage introduced during dry etching. In this chapter, two different strategies are presented: (i) bombardment energy control during dry etching and (ii) post wet etching using NaOH solution. (Photo)electrochemical measurements, SEM measurements and impedance spectroscopy (EIS) were used to characterize the GaN pillars and the surface damage. Some results of this chapter are published in Ref. [2].

5.2 Process description: RF power engineering and post-wet etching

The n-GaN epi-wafer used in this chapter is the same as the GaN wafer used in Chapter 4 [3]. The material properties of the n-GaN epilayer are described in detail in Section 4.2. The top 2 μm of the n-GaN layer is highly Si-doped ($n = 5\times10^{18}$ cm^{-3}), followed by unintentionally-doped GaN and AlGaN buffer layers. The GaN nanopillars were fabricated by reactive-ion etching (RIE) dry etching with an inductively coupled plasma (ICP) source (Plasma Lab 100, Oxford) using self-assembled Ni clusters as mask [4],[5]. The fabrication processes of the GaN pillars are addressed in Section 4.2. The thickness of the Ni and SiO_2 film were 15 nm and 250 nm, respectively. The etching parameters of the SiO_2 etch were: RF power/ICP power/SF_6 flow/O_2 flow/chamber

pressure/temperature/time: 50 W/300 W/ 100 sccm/10 sccm/10 mtorr/20˚C/7.5 mins. The etching rate of SiO_2 was 50 nm/mins. The RF chuck power of the GaN etch was controlled between 13 W to 125 W to introduce different amount of surface damage. The etching rates of GaN range from 55 nm/mins (13 W) to 300 nm/mins (125 W). The other dry etching parameters of the GaN etch were the same for all the pillars (ICP source power/Cl_2 flow/Ar flow/chamber pressure/ temperature =125 W/10 sccm/5 sccm/5 mtorr/20℃). The GaN pillars of 1.6 μm height were used for this work.

After the pillar fabrication using 125 W RF power, the samples were immersed into a 1 M NaOH aqueous solution in the dark for 1 to 15 minutes for the post etching. No solution agitation was applied. The working electrode preparations including the Ohmic contract formation to n-GaN, electrical connection, working area definition and sample encapsulation are described in Section 2.1. The photoelectrochemical measurements were performed using a UV-transparent quartz cell. All potentials were given with respect to an Ag/AgCl RE (Metrohm). A 150 W Xe lamp with an AM 1.5 filter was used as the light source for the photoelectrochemical measurements. The light intensity illuminated at the sample surface was 63 mW/cm^2. Details of the light source are described in Section 2.3. A potentiostat (Autolab, Metrohm) was used for the current-potential control. All linear scan voltammograms were recorded at a constant scan rate (v) of 100 mV/s from negative to positive potentials, unless otherwise stated. A 0.1 M HBr and 0.2 M Na_2SO_4 (Sigma Aldrich) solution was used, with Br^- acting as a sacrificial reagent to avoid photo-corrosion of GaN during photoelectrolysis.

Figure 5.1 (a) shows an image of a GaN sample with a nanopillar array at the center and the unetched GaN at the edge as a visual reference. In contrast to the planar GaN, the pillar array shows a great capacity of light absorption, as evidenced by its black color. A SEM top view and 45° side view are shown in Figure 5.1 (b) and (c), respectively. The pillars are uniformly distributed with an average density of 3.0 ± 0.4 ×10^8 cm^{-2}. No specific crystal facets were visually observed at the surface of the GaN pillar structure except the top plane has an orientation of (0001), which is protected by the SiO_2 layer during dry etching process.

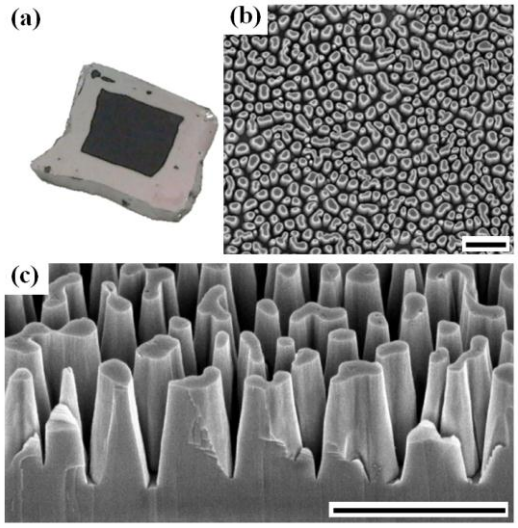

Figure 5.1: (a) A picture of nanoroughened GaN (black) in contrast to surrounding unetched GaN epilayer (light gray). SEM images of 1.6 μm high pillars (b) in top view and (c) at 45°. Scale bar: 2 μm.

5.3 Electrochemical properties of GaN pillars

5.3.1 Electrochemical measurements under illumination

Figure 5.2 shows photocurrent density-potential (j_{ph}-U) plots for the 1.6 μm high n-GaN pillars fabricated by dry etching. The chuck RF power varied from 13 W to 125 W. The dashed j_{ph}-U curve is for planar GaN layer prior to the surface roughening. The onset potential (U_{onset}) and the plateau potential ($U_{plateau}$) of the planar GaN are -0.36 V and 0.06 V, respectively. When planar GaN is under supra-bandgap illumination, excess electron-hole pairs are generated. For $U < U_{onset}$, carrier recombination is the predominant process; no photocurrent is observed. In the potential range between U_{onset} and $U_{plateau}$, photocarriers are partially separated and contribute to the photocurrent. Electrons escape to the counter electrode where they reduce water, while photo-holes oxidize Br^- at the surface of the GaN electrode. For $U > U_{plateau}$, the j_{ph} reaches a plateau value. In this potential range, the electric field is sufficient to separate all the photocarriers in the space

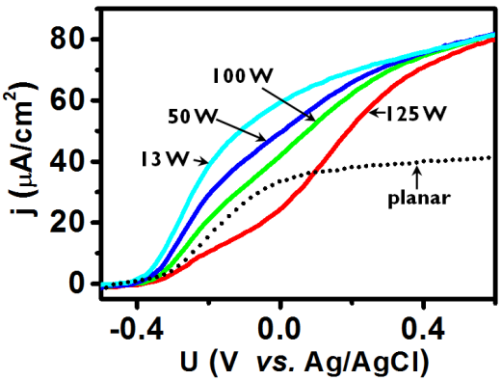

Figure 5.2: Photocurrent-potential (j_{ph}-U) plots of the 1.6 μm high n-GaN pillars fabricated by dry etching at different RF powers. The dashed curve is for the photocurrent of the unetched planar GaN. Solution: 0.1 M HBr + 0.2 M Na_2SO_4; scan rate (*v*): 100 mV/s.

charge region (SCR). All the GaN pillars have comparable j_{ph} in the plateau range. When the RF chuck power increases, both the U_{onset} and $U_{plateau}$ of the pillars shift towards more positive. The $\Delta U_{onset\text{-}plateau}$, defined as: $U_{plateau}$ - U_{onset}, increases with increasing RF power. The photoelectrochemical properties of n-GaN etched at 13 W and 125 W are listed in Table 5.1.

As ICP discharge is applied during dry etching, activated chlorine species chemically react with gallium at the sample surface and form etch products [6]. In the meanwhile, Ar and Cl ions are accelerated to the sample surface to removes Ga-Cl complexes and constituent atoms, which allows the chemical etching of the succeeding layer to proceed. The physical desorption of the etch products is therefore important in the control of etching rates and the anisotropy of the etched surface. However, the bombardment of energetic ions creates damage at the surface and near the surface region of GaN [7]. Specific plasma-induced surface states or traps act as carrier recombination centers [8], which reduce the lifetime of photo-holes. Therefore, for the most damaged pillars (p125W), see Table 5.1, a larger $\Delta U_{onset\text{-}plateau}$ is required to suppress carrier recombination in the SCR. In contrast, for the low-damaged GaN pillars (p13W), a smaller $\Delta U_{onset\text{-}plateau}$ is required or, from another perspective, the j_{ph}-U slope (Figure 5.2) is larger.

Table 5.1: Photoelectrochemical properties of different n-GaN pillars.

sample	RF (W)	NaOH etch (min)	U_{onset}[a] (V)	$\Delta U_{onset\text{-}plateau}$[b] (V)
planar	-	-	-0.36	0.42
p125W	125	-	-0.30	0.67
p125W15'	125	15	-0.42	0.46
p13W	13	-	-0.37	0.41

[a]In the plateau region, the j_{ph}-U relationship is a linear line. Plateau current density ($j_{plateau}$) and plateau potential ($U_{plateau}$) are reached when the current density deviates this linearity by 5 %. The onset potential (U_{onset}) is reached when the current density reach 5 % of the $j_{plateau}$.
[b]$\Delta U_{onset\text{-}plateau} = U_{plateau} - U_{onset}$.

Post-wet etching using alkaline solutions is an effective approach to remove surface damage of GaN [9]-[11]. In the second experiment of this work, we study the influence of the NaOH treatment time on the photoelectrochemical properties of the 1.6 μm-high n-GaN pillars (Figure 5.3). The pillars were fabricated by dry etching with 125 W RF power. The solid red curve and dashed black curve show the j_{ph}-U plots for the as-fabricated pillars and planar GaN, respectively. Both U_{onset} and $U_{plateau}$ of the pillars shift towards negative with increasing immersion time. This suggests that the plasma-induced surface damage is effectively removed by the alkaline solution. The 1 min-NaOH-etched pillars show similar $\Delta U_{onset\text{-}plateau}$ and j_{ph}-U slope as the pillars of 13 W RF power in Figure 5.2. The j_{ph} of the pillars in the plateau range (U = 0.5 V) is enhanced after the alkaline treatment: 8.7% and 11.4% for 5 minutes and 15 minutes of etching, respectively.

The morphology of the GaN pillars after immersion in NaOH solution has been assessed by SEM. The as-fabricated pillars are shown in Figure 5.4 (a). Figure 5.4 (b) and (c) show the GaN pillars in NaOH solution for 1 minute and 15 minutes, respectively. The top plane of the pillars, Ga-polar (0001), is not etched due to its high chemical stability [12],[13]. In contrast, the defective pillar walls were etched by the alkaline solution [14]. The $\{10\bar{1}0\}$ planes were gradually revealed, leaving a stepped surface at the pillar wall. After 15 minutes of etching, a layer of ~60 nm thick was removed at the

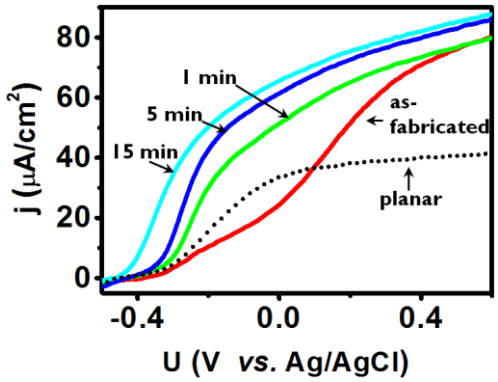

Figure 5.3: j_{ph}-U plots of the 1.6 μm high GaN pillars after a post-wet etching of 1 M $NaOH_{(aq)}$ for different periods of time. All the pillar samples were fabricated by dry etching using a RF power of 125 W. Solution: 0.1 M HBr + 0.2 M Na_2SO_4; *v*: 100 mV/s.

bottom of the pillars, as indicated in Figure 5.4 (cc).

To discuss the photoelectrochemical properties of the $\{10\bar{1}0\}$ planes of the GaN pillars, an additional experiment was performed. In this case, the SiO_2 on the top of the GaN pillars was not removed after dry etching. The fabrication details of the pillars are described in Section 5.2. Because of the SiO_2 capping layer, the top plane (0001) of the pillars is isolated from the solution. Therefore, charge transfer is not possible through this plane. Figure 5.5 (a) shows the j_{ph}-U plots of SiO_2-capped pillars before the wet etching in NaOH solution (Sp125W), SiO_2-capped pillars after wet etching (Sp125W15') and as-fabricated GaN pillars without the SiO_2 capping (p125W). The pillars were all fabricated by dry etching using 125 W RF power. The wet etching was performed in 1 M NaOH aqueous solution in the dark without solution agitation, as described earlier. The SEM image of the Sp125W15' is shown in Figure 5.5 (b).

The j_{ph} of the p125W is consistently higher than the Sp125W by ~9 μA/cm^2 for U > 0.0 V. The extra j_{ph} is contributed by the (0001) plane at the pillar top. It is worth noting that the capping of the top plane only prohibits the charge transfer at the pillar top. Photo-holes can still be generated under the top plane of the pillars and oxidize Br^- once they

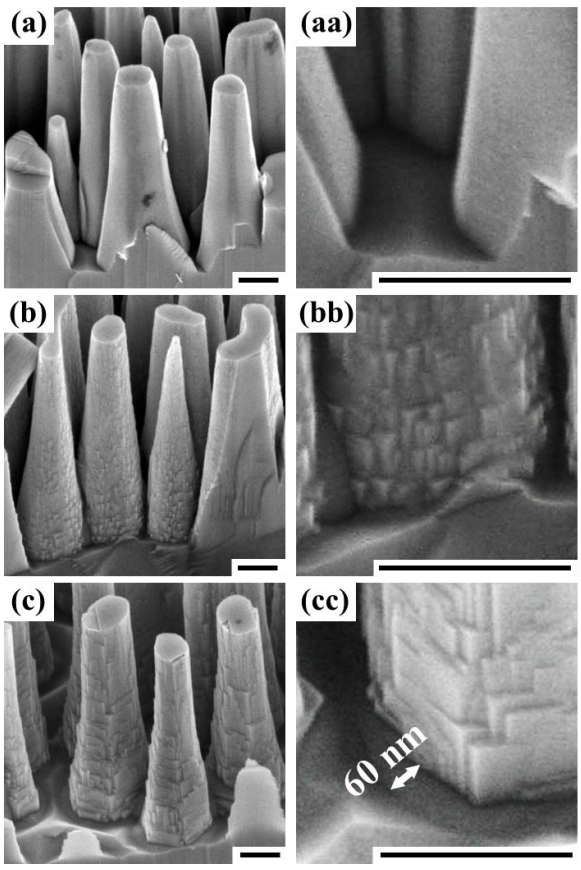

Figure 5.4: SEM images of the pillars at 45° before and after the NaOH wet etching. (a), (aa) The as-fabricated pillars; the pillars after NaOH wet etching for (b), (bb) 1 minute and for (c), (cc) 15 minutes. Scale bar: 300 nm.

reach the surface of the pillar wall. Therefore, the current loss in the Sp125W with respect to the p125W is attributed to carrier recombination during charge migration or surface recombination at the damaged pillar wall. The U_{onset} of the Sp125W shifts towards more positive by 0.1 V than the p125W, which confirms the poor photoactivity of the damaged pillar wall. After the NaOH wet etching, the U_{onset} of the Sp125W15' shifts towards negative by 0.19 V with respect to the Sp125W; the plateau current density becomes higher than the Sp125W. The U_{onset} of the Sp125W15' is even more negative than the planar GaN (Figure 5.2). This confirms the strong photoactivity of the $\{10\bar{1}0\}$ planes.

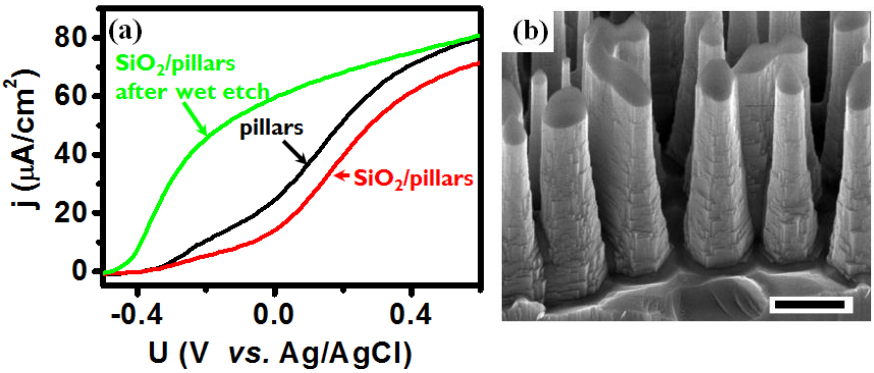

Figure 5.5: (a) j_{ph}-U plots for the as-fabricated pillars, using 125 W RF power, with and without SiO_2 capping at the top of the pillars and the SiO_2-capped pillars after the NaOH wet etching. (b) A SEM image of the SiO_2-capped pillars after the wet etching. Scale bar: 500 nm

Recently, the dissociative mechanisms of water molecules at the GaN surface have been studied using first principal calculations [15],[16] . The GaN surfaces of (0001), $(000\bar{1})$ and $(10\bar{1}0)$ planes show the capacity for water dissociation, but possess different energy barriers for the formation of intermediate species. It has been experimentally demonstrated that the $\{10\bar{1}0\}$ GaN planes of GaN nanowires are highly photocatalytic active and can perform water splitting spontaneously [17]. It is possible that the oxidation of Br^- at the $\{10\bar{1}0\}$ planes of the GaN pillars is more thermodynamically favorable with respect to (0001). This may explain why the U_{onset} of the GaN pillars shifts towards more negative when the $\{10\bar{1}0\}$ planes become more dominant at the pillar wall after the post-wet etching.

To exclude the pillar effect, the GaN epilayer was blanket etched for 1.6 μm by dry etching using 125 W RF power without Ni or SiO_2 mask. The j-U plots of this blanket-etched GaN in the dark and under illumination are shown in Figure 5.6. The scans were recorded at v = 1 mV/s to minimize transient currents. The dark current remains lower than 10 nA/cm^2 for U < 1 V, indicating a low reverse leakage current. However, the photoelectrochemical property of the blanket-etched GaN is seriously deteriorated with respect to the unetched planar GaN in Figure 5.2. The j_{ph} only increases significantly for

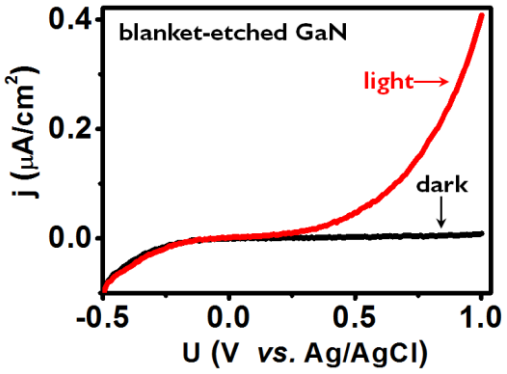

Figure 5.6: (a) j-U plots in the dark and under illumination for 1.6 µm-blanket-etched n-GaN electrode using a RF power of 125 W. Solution: 0.1 M HBr + 0.2 M Na_2SO_4; *v*: 1 mV/s.

U > 0.25 V and the j_{ph} only reaches 0.4 µA/cm^2 at 1 V. In contrast, the j_{ph} of the unetched n-GaN at 0.5 V is 40 µA/cm^2 (see Figure 5.2). The introduction of surface damage has a clear and distinct impact on the photoelectrochemical properties of n-GaN. Carrier recombination becomes a predominant process for the blanket-etched GaN [18]; nearly no photocarriers are available for the electrochemical oxidation of Br^-.

The impact of surface damage on the photoactivity of the pillars can also be investigated by a photo-corrosion experiment. A 0.4 µm high pillar sample was exposed under intense UV irradiation (100 mW/cm^2, Xe lamp) for 4 minutes in the solution of 0.1 M HBr + 0.2 M Na_2SO_4. The solution was not agitated. The potential was biased at the photocurrent plateau (U = 0.5 V). Total anodic charge transfer was 0.25 C/cm^2. Figure 5.7 shows the morphology of the pillars after the photoelectrochemical measurement. The upper part of the pillars (including the top plane) is corroded. The lower part of the pillars is only slightly corroded. GaN at the bottom between the pillars is intact.

In the presence of Br^-, interfacial charge transfer is a favorable process for photo-holes. However, photo-corrosion is not completely suppressed. Under illumination of intense UV, photo-corrosion of n-GaN is accelerated due to abundant photo-holes at the surface with respect to the weak UV experiments (Figure 5.2 and Figure 5.3). Photo-corrosion of

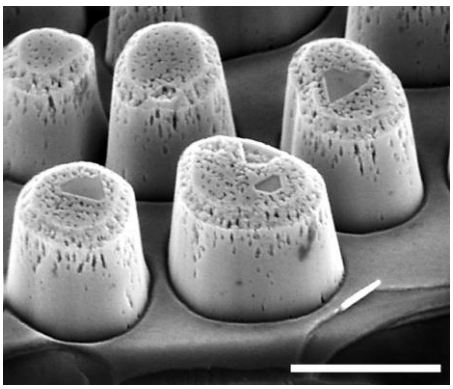

Figure 5.7: A SEM image of 0.4 µm high pillars after a chronoamperometric measurement in a solution of 0.1 M HBr + 0.2 M Na_2SO_4. The integrated anodic charge is 0.25 C/cm^2. Scale bar: 500 nm.

n-GaN is described by

$$GaN + 3h^+ \rightarrow Ga^{3+} + \frac{1}{2}N_2 \tag{5.1}$$

The corrosion of GaN at the upper part of the pillars indicates that the concentration of photo-holes is high. GaN at the bottom of the pillar array, as discussed earlier, is severely damaged by dry etching. Photo-holes generated at the bottom of the pillar array have a very short carrier life time, and predominately recombine with electrons at surface defect sites. Therefore, Br^- oxidation and photo-corrosion of GaN are not possible there. The lower part of the pillar wall receives some degree of damage. The concentration of photo-holes at the surface is not high. Therefore only few photo-holes are used to corrode GaN, resulting in a slightly-corroded surface at the lower part of the pillar wall.

Based on the experiments of Figure 5.3-Figure 5.7, we conclude that the increase of the plateau j_{ph} for the pillars etched $\geq$ 5 minutes results from the removal of damaged GaN at the bottom of the pillar wall. Due to the shape of the self-assembled Ni mask and the different etching rate of the layers, the geometry of the pillars in this work is taper-like. The shape of bottom part of the pillar wall is less vertical and straight than the upper part, as shown in Figure 5.3 (a). Consequently, the bottom part of the pillar receives the highest degree of ion bombardment during dry etching process. We therefore propose that most

of the photoactivity is lost at the bottom of pillar wall for the as-fabricated pillars. Fortunately, dry etching damage is normally introduced within a few hundred angstroms from the surface [19],[20]; the damage decreases significantly with the distance from the surface. After a period of etching in NaOH solution, the damaged layer at the bottom wall is removed. The high quality GaN which is subsequently exposed (Figure 5.4 (cc)) can contribute to the photocurrent.

5.3.2 Electrochemical measurements in dark

Figure 5.8 shows j-U plots for the unetched GaN and the GaN pillars and in the dark. The reduction of ambient-dissolved oxygen in solution by CB electrons is observed for U < ~-0.25 V for the pillar samples and for U < ~-0.4V for the planar GaN, respectively. In case of the pillar samples, a pair of cathodic and anodic peaks is observed at 0.16 V and 0.45 V, respectively. In contrast, this is not the case for the planar GaN. The cathodic peak has a higher peak current and is more symmetric and narrow as compared to the anodic peak. The p125W shows the highest peak current and the p13W shows the lowest peak current among the three pillars. The integrated charge of the cathodic peak is the same as of the anodic peak for all the samples in each scan.

In order to further investigate the electrochemical properties of the pillar samples, cyclic voltammetry measurements were performed in the potential range outside of the peak pair, which is shown in Figure 5.9 (a). In all cases rectangular j-U plots are observed. For U > 0.7 V we did not observe the anodic peak in Figure 5.8 (a) in the rectangular cyclic scans (Figure 5.9 (a)). This indicates that the anodic peak for U > 0.7 V in Figure 5.8 (a) is due to the time effect of the scan. Figure 5.9 (b) shows the current density-time (j-t) plots of the three samples at U = 0.7 V in the dark. No conditioning of potential or current was applied to the samples before the j-t measurements; no other measurements were executed five minutes before the j-t measurements. All the samples show a transient current decaying with time. The current becomes negligible after a period of bias, indicating a minimum of leakage current at the pillar/solution interface. Herein, we conclude that the rectangular j-U plots in Figure 5.9 (a) are a non-Faradaic process and suggest the existence of an electrochemical capacitor in the system [21],[22].

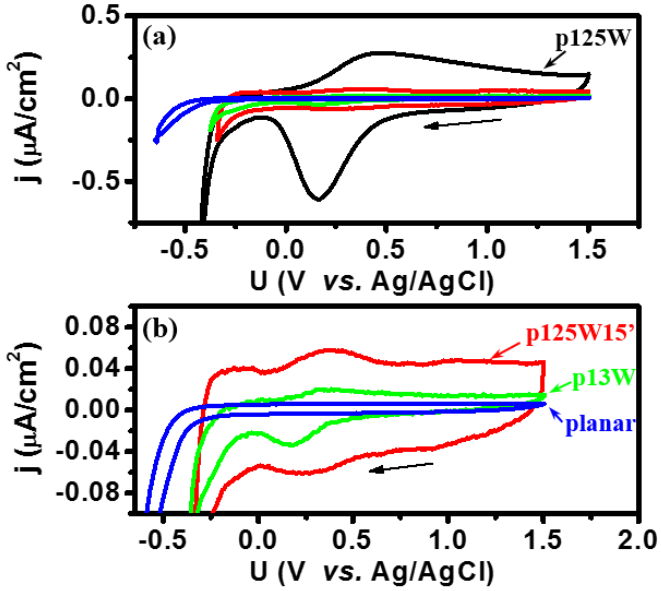

Figure 5.8: (a) j-U plots of the unetched GaN and the GaN pillars in the dark and (b) the j-U plots at a different scale. Solution: 0.1 M HBr + 0.2 M Na_2SO_4; *v*: 100 mV/s.

The differential capacitance (C_r) is defined by d*Q*/d*U*, where *Q* and *U* are the charge stored in the capacitor and the potential drop over the capacitor respectively. By a further differential of both *Q* and *U* with time, the capacitance can be linked to the current density (*j*) and scan rate (*v*) by

$$C_r = \frac{{}^{dQ}/_{dt}}{{}^{dU}/_{dt}} = \frac{j}{v} \tag{5.2}$$

Table 5.2 lists the capacitance (C_r) of the pillar electrodes deduced from the j-U plots (Figure 5.9 (a)). The C_r is found to be associated with surface damage. It decreases with decreasing dry etching damage and can be reduced by NaOH wet etching treatment. The C_r of the p125W15' is higher than the p13W. This indicates that although NaOH wet etching etches GaN surface effectively, the surface damage is not completely removed.

Figure 5.10 (a) shows the cyclic voltammograms of the p125W in the dark as a function of *v*. The cathodic peak potential (U_{peak}) is located at 0.16 V and is independent of *v*. The

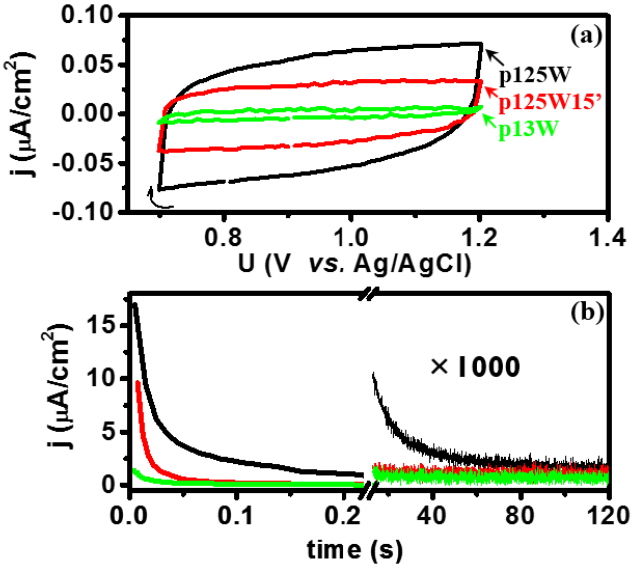

Figure 5.9: (a) j-U plots for the n-GaN pillars in the dark. Solution: 0.1 M HBr + 0.2 M Na_2SO_4; *v*: 100 mV/s. (b) j-t plots of the GaN pillars biased at 0.7 V in the dark.

cathodic peak current density increases linearly with increasing *v* (see the inset of Figure 5.10 (a)). This indicates that the reaction is under kinetic control. In contrast, the anodic U_{peak} shifts 0.18 V to 0.49 V with increasing *v*. The integrated charge of the cathodic current is the same as that of the anodic current for all *v*.

The cyclic voltammogram of the p125W under illumination is shown in Figure 5.11. The electrolyte was not purged prior to the measurement and was not agitated during the measurement. For U > -0.3 V, Br^- is oxidized by photo-holes to Br_3^- with the assistance of surface traps [23],[24]. Subsequently, Br_3^- at the GaN surface is reduced to Br^- in the backward scan at U = -0.5 V. The reduction of dissolved oxygen from ambient contributes to the peak at -1.06 V. Proton reduction occurs for U < -1.15 V. It is clear that no cathodic current is observed at U = 0.16 V. Consequently, the cathodic peak shown in Figure 5.10 (a) cannot be attributed to the electron charge transfer from the CB or surface traps. Hence, we ascribe the cathodic peak to the electron charging of the plasma-induced

Table 5.2: Capacitance (C_r) obtained from the rectangular cyclic voltammograms (Figure 5.9 (a)) where $C_r = j/v$.

Sample	C_r ($\mu F/cm^2$)
planar	<0.01
p125W	0.71
p125W15’	0.34
p13W	0.05

surface traps. The unetched planar GaN in Figure 5.8 (b) shows a low current and no anodic peak in the reverse bias regime. We therefore believe the anodic peak of the p125W in Figure 5.10 (a) can be explained by the discharging of occupied traps.

The Br^- oxidation is a process of photo-hole capture from the VB of GaN. Discharging of the traps through electron injection to the electrolyte is not possible. Bertoluzzi et al. constructed a model to interpret the cyclic voltammograms of charging and discharging of surface traps [25]. When the detrapping of electrons to CB is slower than the charging but is faster than carrier recombination, a broad anodic peak is found, as shown in Figure 4f in ref. [25]. In this case, the anodic U_{peak} shifts more positive than the cathodic U_{peak} and a long tail is found due to the slow discharging. This model confirms to our experimental observation. However, in our case the integrated cathodic charge is the same as of the anodic charge. The detrapping by carrier recombination should be ignorable. Hole concentration for carrier recombination is expected to be low, considering the electron concentration ($5\times10^{18}cm^{-3}$) and bandgap of GaN (3.4 eV). Therefore, only charging of traps and discharging of trapped electrons to the CB contribute to the cathodic peak and anodic peak, respectively.

Trap-assisted tunneling to the CB is one of main mechanisms for reverse leakage current at the metal/n-GaN Schottky interface. However, in our case with weak surface band bending, the trapped electrons cannot directly tunnel to the CB due to the thick barrier. Multistep tunneling may be involved in the detrapping process [26]. Although the traps found in Figure 5.10 is monoenergetic, dry etching not only damages GaN surface

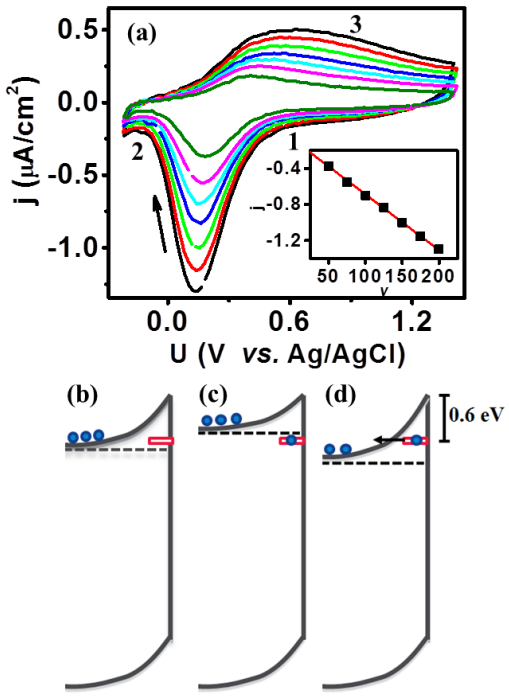

Figure 5.10: (a) j *vs.* U for the p125W at different *v* in the dark with the inset showing the cathodic peak current density as a function of *v*. Solution: 0.1 M HBr + 0.2 M Na_2SO_4. The band diagrams of the GaN pillars with surface traps under (b) the condition 1, (c) the condition 2 and (d) the condition 3.

but also creates damage in the near surface region. It is very possible the trapped electrons can tunnel to the CB via these plasma-induced traps in the near surface region.

The flat-band potential (U_{fb}) of the p125W, deduced from the Mott-Schottky relation, is -0.44 V (Table 5.3). The cathodic U_{peak} is observed at 0.16 V. Therefore, we can conclude that the energy of the trap level (E_t) is around 0.6 eV below the CB edge of GaN. When the GaN photoanode is biased more positive than 0.6 V below the CB edge, as schematically illustrated in Figure 5.10 (b), the Fermi-level is below E_t, leaving the trap levels unoccupied. While the n-GaN electrode becomes negatively polarized, Fermi level moves upwards and the surface electron concentration increases. Once E_f is higher

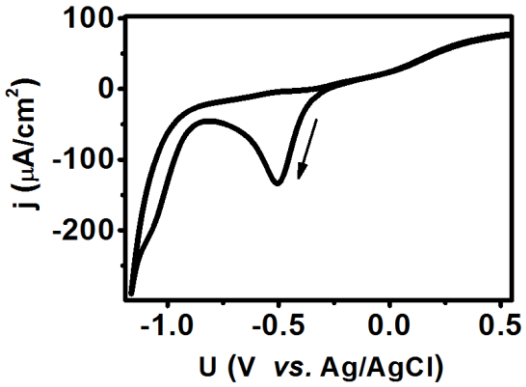

Figure 5.11: j-U plots for the p125W under illumination. The cathodic peaks located at -0.50 V, -1.06 V and V > -1.15 V are for the reduction of Br_3^-, dissolved oxygen from ambient and proton, respectively. Solution: 0.1 M HBr + 0.2 M Na_2SO_4; *v*: 100 mV/s.

than the energy of trap levels, shown in Figure 5.10 (c), the traps are rapidly filled, contributing to the cathodic current. The narrow cathodic profile indicates that the charging of the traps is kinetically favorable. When the bias scans positively from -0.2 V, E_f moves downward. The discharging of the traps starts when $E_f < E_t$. Electrons of the traps can be released to CB by multistep tunneling. Since the detrapping is a complex and slow process, the anodic j-U profile shows a long tail at U > 0.5 V. This peak current of the trapping and detrapping can be indication of surface damage for the pillars. The p125W gives the highest peak current due to the strongest damage. After immersion in NaOH solution, most of the damaged layer is removed for the p125W15'. However, due to the selective etching, some damaged layer, particularly at the bottom between the pillars, cannot be etched. Consequently, the peak currents are reduced but are still higher than the p13W.

5.4 Impedance measurements of GaN pillars

The electrochemical impedance spectroscopy (EIS) measurement of three samples: p125W, p125W15', p13W were measured in a solution of 0.1 M HBr + 0.2 M Na_2SO_4 in the dark. The AC frequency was modulated from 4500 Hz to 50 Hz; an AC potential of

0.1 V was applied for each scan. Figure 5.12 (a) shows Nyquist plots of these three pillars at U = 0.5 V. The scales of the Z' axis and Z'' axis are not identical for a better visualization. The Z' and Z'' here are obtained using projected working area of the pillar electrodes instead of the effective surface area. No second semicircle was observed for all Nyquist curves. The $R_s(R_{ct}C_{cs})$ was used as the equivalent circuit for the EIS analysis. The "Goodness of Fit" (χ^2) [27] is less than 0.02. The theory of the EIS and the equivalent model are addressed in Section 3.5.

The Mott-Schottky (M-S) plots of these three samples are shown in Figure 5.12 (b). The inset of Figure 5.12 (b) is for the M-S plot of planar n-GaN. The high linearity of the M-S relation shows the carrier concentration is uniformly distributed in the near surface region. Due to the high carrier concentration ($n = 5\times10^{18}$ cm^{-3}), the SCR width of the n-GaN is small. (i.e. 19 nm at U = 1 V for the planar n-GaN). The pillars all show a linear M-S relationship for U > ~0.4 V, but all have a smaller M-S slope for U < ~0.4 V. The U_{fb} of the planar GaN and the GaN pillars, obtained from the M-S plots, are listed in Table 5.3.

The surface area and carrier concentration of the electrodes both influence the capacitance of depletion region (Eq. (3.29)). In addition, plasma defects can change carrier concentration at the near surface region. The morphology of the p125W15' is different from the p125W and the p13W (see Figure 5.4). In order to avoid complexity, the slopes of the M-S plots for the p125W and p125W15' are normalized to that of the p13W (0.53×10^{11} $F^{-2}cm^4V^{-1}$), as shown in Figure 5.12 (c).

Three pillar samples show a linear M-S relationship for U > 0.4 V and U < 0.0 V. A smaller M-S slope is observed between 0.0-0.4 V for all the pillar samples. This is not the case for the planar n-GaN. The change of the M-S slope in this potential range is ascribed by the charging and discharging of surface traps, as described in Section 4.4. When the Fermi-level reaches the surface traps, the potential does not fall across the SCR, but is used to charge empty traps or deplete occupied surface traps. In our case, the energy position of the surface states can be dispersed, or the Fermi-level is not completely pinned by these surface traps. Therefore, the smaller slope is observed instead of a horizontal line between two parallel M-S lines (Figure 4.11).

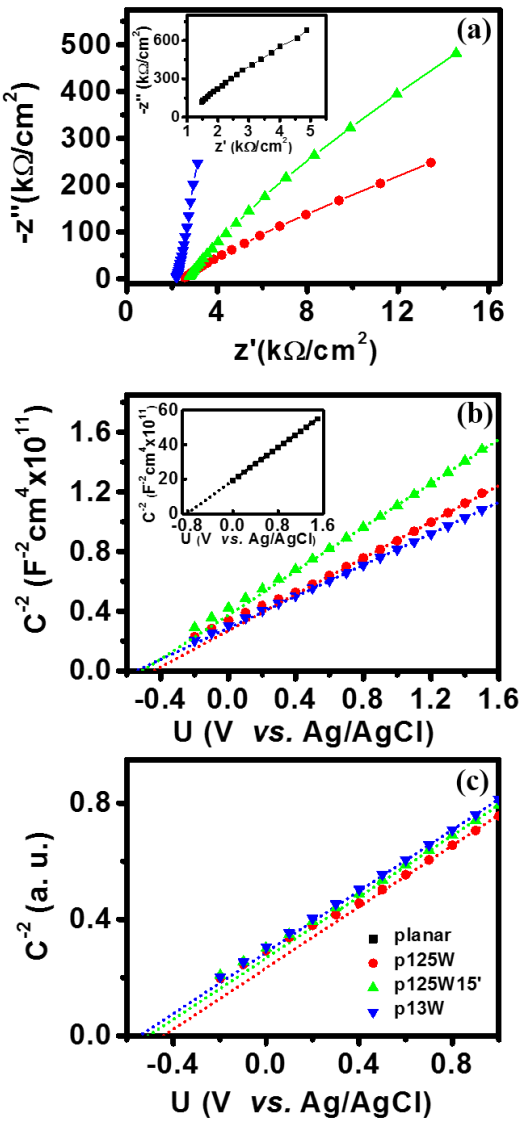

Figure 5.12: (a) Nyquist plots of the planar n-GaN and the n-GaN pillar samples (U_{WE-RE} = 0.5 V). (b) Mott-Schottky (M-S) plots for all the samples. (c) The M-S plots where all the M-S slope of the samples were normalized to that of the p13W (0.53×10^{11} $F^{-2}cm^4V^{-1}$). Solution: 0.1 M HBr + 0.2 M Na_2SO_4; scan frequency range: 4500-50 Hz; AC potential: 0.1 V.

Table 5.3: The flat-band potentials (U_{fb}) of the planar GaN and the GaN pillars, obtained from the M-S plots in Figure 5.12.

Sample	U_{fb} (V)
planar	-0.81
p125W	-0.44
p125W15’	-0.51
p13W	-0.55

The parallel potential shift of the M-S plot therefore can be used to compare relatively the density of surface states at damaged surface. The p125W has the largest potential shift and the p13W has the lowest potential shift among these three pillar samples. The damage is clearly reduced after bombardment energy is minimized or the damaged layer is removed. It is worth noting that the potential shift of the p125W15’ is still slightly larger than the p13W. Although wet etching removes the damaged surface effectively, a complete removal of the damaged layer is not possible due to etching selectivity of facets (Figure 5.4 (cc)).

The introduction of surface damage also have an impact on the U_{fb} (see Table 5.3). The U_{fb} of planar GaN is at -0.81 V, and U_{fb} of the most damaged pillars (p125W) is at -0.44 V. This positive shift of U_{fb} indicates the role of surface damage. The negative shift of U_{fb} for the p125W15’and p13W indicates that surface damage is reduced and the surface is partially recovered. The fact that the U_{fb} of the p13W is more negative than the p125W15’ also concludes the surface of the p13W is less damaged.

5.5 Summary

We fabricated n-GaN pillars by ICP dry etching from a planar GaN epilayer. Although, the j_{ph} is enhanced after surface roughening, the GaN surface is damaged by dry etching process. In this chapter, two approaches were used to minimize surface damage: process optimization and post wet etching. Electrochemical measurements under illumination and

in the dark and EIS measurements were used to characterize the properties of these GaN pillars.

For the photoelectrochemical measurements, we found that as the RF power is minimized (13 W), the pillar sample shows a similar $\Delta U_{onset\text{-}plateau}$ and j-U as the planar n-GaN. Using $NaOH_{(aq)}$ wet etching, the damaged GaN surface can be removed. The 1 min-NaOH-etched pillars show a similar j-U characteristic as the pillars etched using 13 W RF power. After 15 mins of wet etching, the plateau j_{ph} of the GaN pillars increases by 100% and the U_{onset} shifts negatively by 60 mV with respect to the planar GaN. As the etching time increases, the $\{10\bar{1}0\}$ planes of GaN become more dominant at the pillar walls. The high photoactivity of the $\{10\bar{1}0\}$ planes results in the negative U_{onset} shift with respect to the (0001) plane.

A pair of anodic and cathodic peaks are found in the cyclic voltammograms for the damaged pillars in the dark, which indicates charging and discharging of deep-level traps. For the low-damaged pillars and the pillars after wet etching, the capacitive current is strongly reduced. For the EIS measurements, all the pillars show a linear M-S relationship for $U > 0.4$ V and $U < 0.0$ V. A parallel potential shift of the M-S plots is observed for all the pillars, and the potential shift can be minimized by reducing surface damage. The U_{fb} of the highly damaged pillars becomes more positive by 0.37 V than the planar GaN. The U_{fb} of the low-damaged pillars and the pillars after wet etch shift towards negative with respect to the highly-damaged pillars as a result of surface damage reduction.

5.6 References

[1] W. J. Tseng, D. H. van Dorp, R. R. Lieten, B. Mehta, P. M. Vereecken, and G. Borghs, *ECS Electrochem. Lett.*, **2**, H51 (2013).

[2] W. J. Tseng, D. H. van Dorp, R. R. Lieten, P. M. Vereecken, R. Langer, and G. Borghs, *J. Phys. Chem. C*, **118**, 11261 (2014).

[3] K. Cheng, M. Leys, S. Degroote, M. Germain, and G. Borghs, *Appl. Phys. Lett.*, **92**, 192111 (2008).

[4] J. Benton, J. Bai, and T. Wang, *Appl. Phys. Lett.*, **102**, 173905 (2013).

[5] W. J. Tseng, M. Gonzalez, L. Dillemans, K. Cheng, S. J. Jiang, P. M. Vereecken, G. Borghs, and R. R. Lieten, *Appl. Phys. Lett.*, **101**, 253102 (2012).

[6] S. J. Pearton, R. J. Shul, and F. Ren, *MRS Internet J. Nitride Semicond. Res.*, **5**, 1 (2000).
[7] J. M. Lee, K. M. Chang, S. W. Kim, C. Huh, I. H. Lee, and S. J. Park, *J. Appl. Phys.*, **87**, 7667 (2000).
[8] D. E. Aspnes, *Surface Sci.*, **132**, 406 (1983).
[9] X. H. Wang, J. Q. Ning, S. J. Xu, and H. W. Choi, *J. Appl. Phys.*, **110**, 093111 (2011).
[10] M. Itoh, T. Kinoshita, K. Kawasaki, M. Takeuchi, C. Koike, and Y. Aoyagi, *Phys. Status Solidi C*, **6**, 1624 (2006).
[11] D. W. Jeon, L. W. Jang, J. W. Jeon, J. W. Park, Y. H. Song, S. R. Jeon, J. W. Ju, J. H. Baek, and I. H. Lee, *J. Nanosci. Nanotechnol.*, **13**, 3645 (2013).
[12] D. Zhuang and J. H. Edgar, *Mater. Sci. Eng. R*, **48**, 1 (2005).
[13] D. S. Li, M. Sumiya, S. Fuke, D. R. Yang, D. L. Que, Y. Suzuki, and Y. Fukuda, *J. Appl. Phys.*, **90**, 4219 (2001).
[14] D. A. Stocker, E. F. Schubert, and J. M. Redwing, *Appl. Phys. Lett.*, **73**, 2654 (1998).
[15] X. Shen, Y. A. Small, J. Wang, P. B. Allen, M. V. Fernandez-Serra, M. S. Hybertsen, and J. T. Muckerman, *J. Phys. Chem. C*, **114**, 13695 (2010).
[16] P.-T. Chen, C.-L. Sun, and M. Hayashi, *J. Phys. Chem. C*, **114**, 18228 (2010).
[17] D. F. Wang, A. Pierre, M. G. Kibria, K. Cui, X. G. Han, K. H. Bevan, H. Guo, S. Paradis, A. R. Hakima, and Z. T. Mi, *Nano Lett.*, **11**, 2353 (2011).
[18] J. Li and L. M. Peter, *J. Electroanal. Chem.*, **193**, 27 (1985).
[19] X. A. Cao, S. J. Pearton, G. T. Dang, A. P. Zhang, F. Ren, and J. M. Van Hove, *IEEE Trans. Electron Devices*, **47**, 1320 (2000).
[20] H. W. Choi, S. J. Chua, and S. Tripathy, *J. Appl. Phys.*, **92**, 4381 (2002).
[21] C. S. Du, J. Yeh, and N. Pan, *Nanotechnology*, **16**, 350 (2005).
[22] B. J. Yoon, S. H. Jeong, K. H. Lee, H. S. Kim, C. G. Park, and J. H. Han, *Chem. Phys. Lett.*, **388**, 170 (2004).
[23] S. Schaefer, A. H. R. Koch, A. Cavallini, M. Stutzmann, and I. D. Sharp, *J. Phys. Chem. C*, **116**, 22281 (2012).
[24] I. M. Huygens, A. Theuwis, W. P. Gomes, and K. Strubbe, *PCCP*, **4**, 2301 (2002).
[25] L. Bertoluzzi, L. Badia-Bou, F. Fabregat-Santiago, S. Gimenez, and J. Bisquert, *J. Phys. Chem. Lett.*, **4**, 1334 (2013).
[26] S. Karmalkar, D. M. Sathaiya, and M. S. Shur, *Appl. Phys. Lett.*, **82**, 3976 (2003).
[27] χ^2 of 10^{-4}, 10^{-2} and 10^{-1} approximately corresponds to a 1%, 10% and 30% difference between the measured and fitted impedances. Gamry Instruments, Equivalent Circuit Modeling. http://www.gamry.com/application-notes/equivalent-circuit-modeling-using-the-gamry-eis300-electrochemical-impedance-spectroscopy-software/

CHAPTER 6

Nanoporous n-GaN photoanodes by anodic etching

Chapter 6. Nanoporous n-GaN photoanodes by anodic etching

6.1 Introduction

As demonstrated in Chapter 4 and Chapter 5, surface roughening introduces more space charge region (SCR). Therefore, the separation of photocarriers can be improved at the nanoroughened GaN electrode, resulting in the enhanced photoactivity. Surface roughening using wet etching techniques are desirable due to the process simplicity and low costs. However, the superior chemical stability of the GaN (0001) plane, which is the predominant plane for GaN epitaxy, prevents etching by most chemicals [1]. To date, only the photoelectrochemical property of n-GaN etched by hot concentrated H_3PO_4 has been reported [2]. Light-assisted electrochemical etching is a well-developed technique to etch n-GaN. The n-GaN is oxidized by photo-holes and subsequently dissolves in the alkaline or acid solution. However, due to higher carrier recombination rate, the density of photo-holes at the defect sites is less than that at the high quality GaN region. Consequently, in the photoelectrochemical etching, the etching rate of the high quality defect-free n-GaN is relatively faster, resulting in the deteriorated material quality after the etching [3].

Recently, the porosification of n-GaN by electrochemical anodic etching has been developed, and is mainly motivated by the need for a strain-free template and light-emitting applications [4],[5]. The surface morphology of porous n-GaN etched in different etchants, such as HNO_3 [4], HF [6] and $H_2C_2O_4$ [7], has been reported. Furthermore, the correlation between dopant density of n-GaN and pore morphology has been established [8]. However, the electrochemical discussions of anodic etching of n-GaN are not well discussed. Moreover, the photoelectrochemical studies of anodically-etched porous n-GaN are very limited [7].

In this work, we have fabricated porous n-GaN using electrochemical anodic etching from a planar n-GaN epilayer in a 0.5 M H_2SO_4 solution. Under illumination, the plateau

photocurrent of the porous n-GaN increases over 4 times compared to planar GaN. Firstly, we used cyclic voltammetry and chronoamperometry to discuss anodic etching of n-GaN, followed by the morphology discussions of the porous GaN etched at different potentials. In the end, the photoelectrochemical properties of the porous GaN are presented. Some results of this chapter are published in Ref. [9].

6.2 Anodic etching of GaN studied by electrochemical measurements

6.2.1 Sample description

A Ga-polar GaN (0001) layer was epitaxially grown on a Si (111) substrate by metal organic chemical vapor deposition (MOCVD) [10]. The top 1.7 μm of the n-GaN layer is highly Si doped, followed by the unintentionally-doped (UID) GaN and AlGaN buffer layers. The electron concentration for the n-GaN and UID GaN layers are respectively 6 $\times 10^{18}$ cm^{-3} and 5×10^{16} cm^{-3}, assessed by Hall effect measurements. The full width at half maximum (FWHM) of the GaN X-ray diffraction measurement (Panalytical, Philips) is 350 and 550 arc second for the (0002) and $(10\bar{1}2)$ reflection, respectively. The details of working electrode preparation are described in Section 2.1.

The anodic etching was performed in the dark at room temperature using a two electrode configuration with a projected working area of the n-GaN electrode and the Pt counter electrode of 0.25-0.5 cm^2 and 4 cm^2, respectively. A potentiostat (Autolab, Metrohm) was used for current-potential control. A 0.5 M H_2SO_4 (Sigma Aldrich) aqueous solution was used for the anodic etching. The solution was stirred using a magnetic stirring rod during the etching to remove the bubbles generated at the n-GaN surface. To distinguish the applied potential used in the anodic etching and the photoelectrochemical measurement, the former one and later one are denoted by U_{etch} and U, respectively.

6.2.2 Cyclic voltammograms

Figure 6.1 shows cyclic voltammograms (CV) of n-GaN in the dark in the 0.5 M H_2SO_4 aqueous solution at the scan rates (v) of 5 V/s and 1 V/s. For $U_{etch} <$ 4 V, current is lower than 20 μA/cm^2. A Schottky junction is formed at the n-GaN/solution interface. For U_{etch} is more positive than the flat-band potential, electrons are depleted near the surface, leading to the formation of SCR. No holes are available in the dark for the charge transfer considering the high bandgap of GaN and high doping level. For $U_{etch} > 4$ V, the anodic current arises, and porous etching of n-GaN is observed for $U_{etch} \geq 5.5$ V as shown later.

Zener tunneling and avalanche breakdown are two main mechanisms for hole supply in anodic etching [11]. In this first case, when the distance between conduction band (CB) and valence band (VB) is short enough under an external reverse bias, the direct tunneling of electrons from VB to CB is possible. Therefore, this effect preferentially happens at a highly-doped semiconductor due to the thin SCR. Avalanche breakdown occurs when charge carriers possess high enough energy, empowered by acceleration of electric field, to break electron-hole bonds. It preferentially happens at lowly-doped semiconductors as charge acceleration in a longer SCR is needed. Considering high doping concentration of our samples, we believe that Zener tunneling is the dominant mechanism for hole generation during anodic etching.

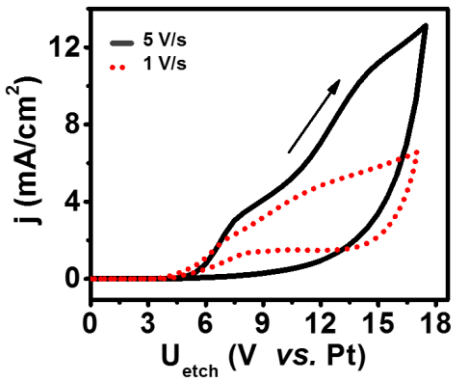

Figure 6.1: Cyclic voltammograms of n-GaN in the dark, measured at the scan rates (v) of 1 V/s and 5V/s. Solution: 0.5 M H_2SO_4.

For both scan rates, the current density increases monotonically with increasing U_{etch} in the forward scan direction. Two current plateaus are observed: the first plateau is located at 7 V < U_{etch} < 8 V for both *v*; the second plateau starts at 11 V and 14 V for 1 V/s and 5 V/s, respectively. For the first plateau, the difference in current density is ~32% for 1 V/s and 5 V/s; for the second plateau, the difference in current density is ~55%. The observation of two current plateaus indicate different etching mechanisms, as confirmed later by the pore morphology.

Hole generation during anodic etching strongly depends on the electric field of SCR. When U_{etch} increases in the forward scan (Figure 6.1), the electric field increases. More holes are generated and contribute to the oxidation of n-GaN. During etching, an oxide layer forms and passivates the GaN surface. The contact between the GaN surface and solution is locally blocked by this oxide layer. In the presence of surface oxide, the applied U_{etch} is predominately shared by both the SCR and the oxide layer. Consequently, once the forward scan is reversed, the electric field of the SCR is reduced because of the oxide layer; the etching current drops rapidly. For *v* = 5 V/s, the current decreases continuously in the reverse scan. At this fast scan rate, there is no sufficient time for the oxide to dissolve. The etching of the underlying GaN is not possible; the current therefore decreases continuously for decreasing U_{etch}. The dissolution of the oxide layer is observed in the slow reverse scan (1 V/s). The etching current remains approximately the same for 8 V < U_{etch} <14 V.

A chronoamperometric experiment (Figure 6.2 (a)) was performed as a complementary study of the CV scans. Two potentiostatic etches, which are indicated as the 1st and 2nd etching, were sequentially performed at the same n-GaN sample at U_{etch} = 15.0 V. The integrated charge for the first and second etch are 1.23 C/cm^2 and 1.36 C/cm^2, respectively. The porosification of the full n-GaN layer (1.7 μm) requires 4.59 C/cm^2. A rapid current drop is observed at the first 15 s. The current then rises to a current peak (15-60 s), followed by a continuous current increase (t > 60 s).

At t > 0 s, the GaN surface starts to be oxidized. The resistance increases due to the formation of oxide layer, resulting in the current drop. The formation rate of the oxide is higher than the dissolution rate, and the current density rapidly drops. At t > 15 s, some

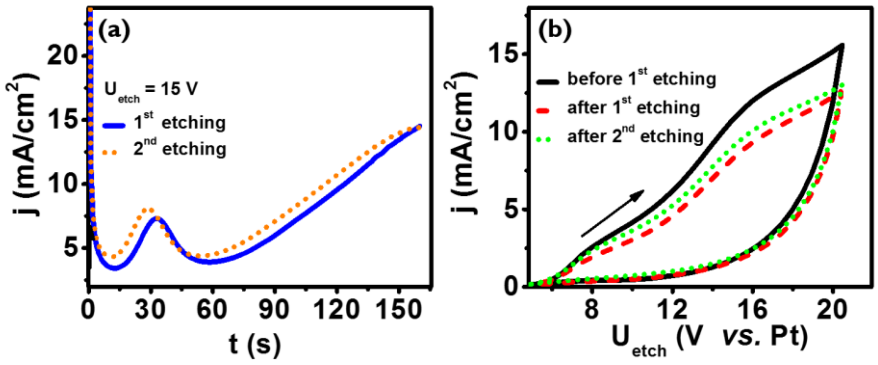

Figure 6.2: (a) Current density-time (j-t) plots of n-GaN etched at 15.0 V for 160 seconds. (b) Cyclic voltammograms of the n-GaN before and after the first and second potentiostatic etch. Solution: 0.5 M H_2SO_4; v = 5 V/s.

of the oxide is partially dissolved and the etching of the succeeding layer is possible. The current peak and the current increase after t > 60 s show the balancing of the surface oxidation and oxide dissolution. The similarity of these two j-t plots proves that the transient etching current is mainly determined by the kinetics and the rate balancing of the surface oxidation and oxide dissolution instead of the pore depth.

Three CV scans performed before and after these two potentiostatic etches are shown in Figure 6.2 (b). The solid and dashed curves are for the CV before and after the first potentiostatic etch, respectively. The dotted curve is for the CV after the second potentiostatic etch. The three CV scans are comparable. The current-potential characteristics are independent of the pore depth. Consequently, we conclude that the ion diffusion in and out of the pore is not a rate-limiting step in this work.

6.2.3 Chronoamperograms

Figure 6.3 (a) shows the j-t plots of the potentiostatic etch at different U_{etch}. The sudden current drop happens when the 1.7 µm n-GaN layer is completely porosified at the end of each curve. The anodic etching of the succeeding UID GaN layer is not possible. The etching time for the full layer decreases when U_{etch} increases as a result of increased etching rate. For the anodic etching at high U_{etch} (≥ 10.0 V), a rapid current drop is

observed for the first 15 s, followed by a few oscillations until the current reaches the steady state. This confirms that the oxidation kinetics is faster than the oxide dissolution. For the etching at small $U_{etch} \leq 8.5$ V, neither the current drop at the beginning nor the strong current oscillation are observed. At $U_{etch} = 18.0$ V, electropolishing of n-GaN layer happens, which may explain why the j-t curve is different from the curve trend.

Figure 6.3 (b) shows the steady-state current density (j_{ss}) as a function of U_{etch}, obtained from Figure 6.3 (a). The j_{ss} for $U_{etch} \leq 15.0$ V is determined by the convergence of the current oscillation. The etching experiments using $U_{etch} = 18.0$ V and 15.0 V were repeated for 3 and 5 times, respectively. The experiments using $U_{etch} \leq 13.0$ V were repeated twice for each U_{etch}. The error in Figure 6.3 (b) is defined by the difference between the maximum and minimum j_{ss} value of all etching experiments at each U_{etch}. For $U_{etch} \leq 13.0$ V, the error is smaller than the size of the symbols in the figure. The j_{ss} increases monotonically with U_{etch}, indicating that hole supply is the rate-limiting factor. Two current plateaus are observed at ~ 10.0 V and ~ 15.0 V, which are slightly more positive than in the CV scans (Figure 6.2 (b)). We believe in the case of the steady-state

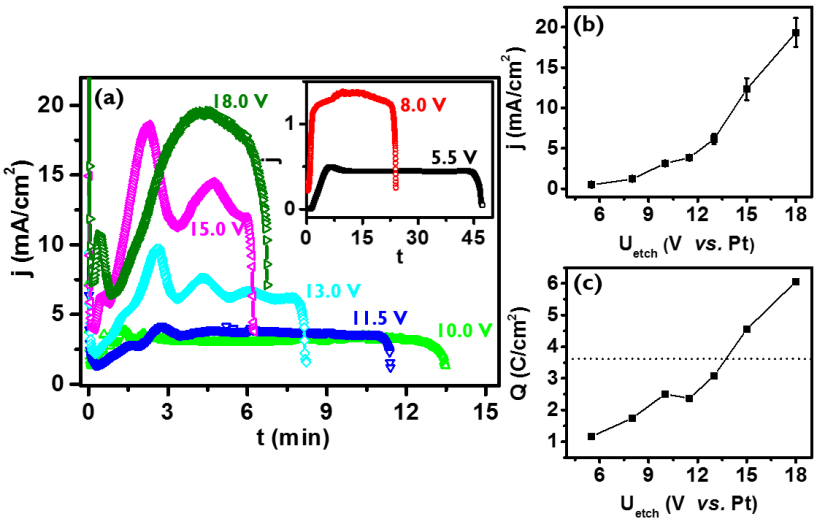

Figure 6.3: (a) j-t plots of n-GaN etched in the 0.5 M H_2SO_4 solution at different U_{etch} in the dark. (b) The steady-state current (j_{ss}) and (c) the integrated charge (Q) of the potentiostatic etch as a function of U_{etch}.

experiments, the formation and dissolution of oxide reach an equilibrium. Therefore, in this case, a thicker oxide layer is formed and there is a larger potential drop over the oxide layer with respect to the CV scans. Therefore, the U_{etch} of these two plateaus are positively shifted in the steady-state experiments.

Figure 6.3 (c) shows the integrated charge of each potentiostatic etch. The error of each data point was evaluated in the same way as Figure 6.3 (b), and is all smaller than the symbol size in the figure. The increase of the integrated charge shows that the porosity of the GaN film increases as U_{etch} increases. For anodic etching, 3 charges are required to oxidize a nitride of GaN (oxidation state: -3 to 0). The oxidation of a 1.7 μm n-GaN layer therefore requires 3.6 C/cm^2 of charge, indicated by a dashed line in Figure 6.3 (c). The integrated charge for $U_{etch} \geq 15.0$ V becomes higher than the charge required for the oxidation of the complete GaN layer. Hence, a part of the photo-holes must be used in the oxidation of water.

6.3 Morphology of porous GaN

In this section, the morphology of porous GaN etching at different U_{etch} is discussed. Figure 6.4 shows the top-view SEM images of different porous GaN. The U_{etch} varies from 5.5 V to 18.0 V. All images are presented using the same magnification except Figure 6.4 (f). The surface pore density and the pore size both increase as U_{etch} increases. For U_{etch} = 8.0 V and 11.5 V, the pore density at the top surface is 2.9×10^9 cm^{-2} and 2.6×10^{10} cm^{-2}, respectively. For $U_{etch} \leq 8.0$ V, the pores are isolated and distributed non-uniformly on the surface. For $U_{etch} \geq 11.5$ V, the pores become so close that some of the pores are merged. For U_{etch} = 15V shallow pits (grey) exist next to the deep pores (black). Partial electropolishing is observed at 18.0 V.

A heteroepitaxial GaN film contains various structural defects at the surface like vacancies, dislocations, and pits [12],[13]. Due to higher chemical activity, the etching at these defect sites is relatively faster than at other sites at the surface [14]. After the

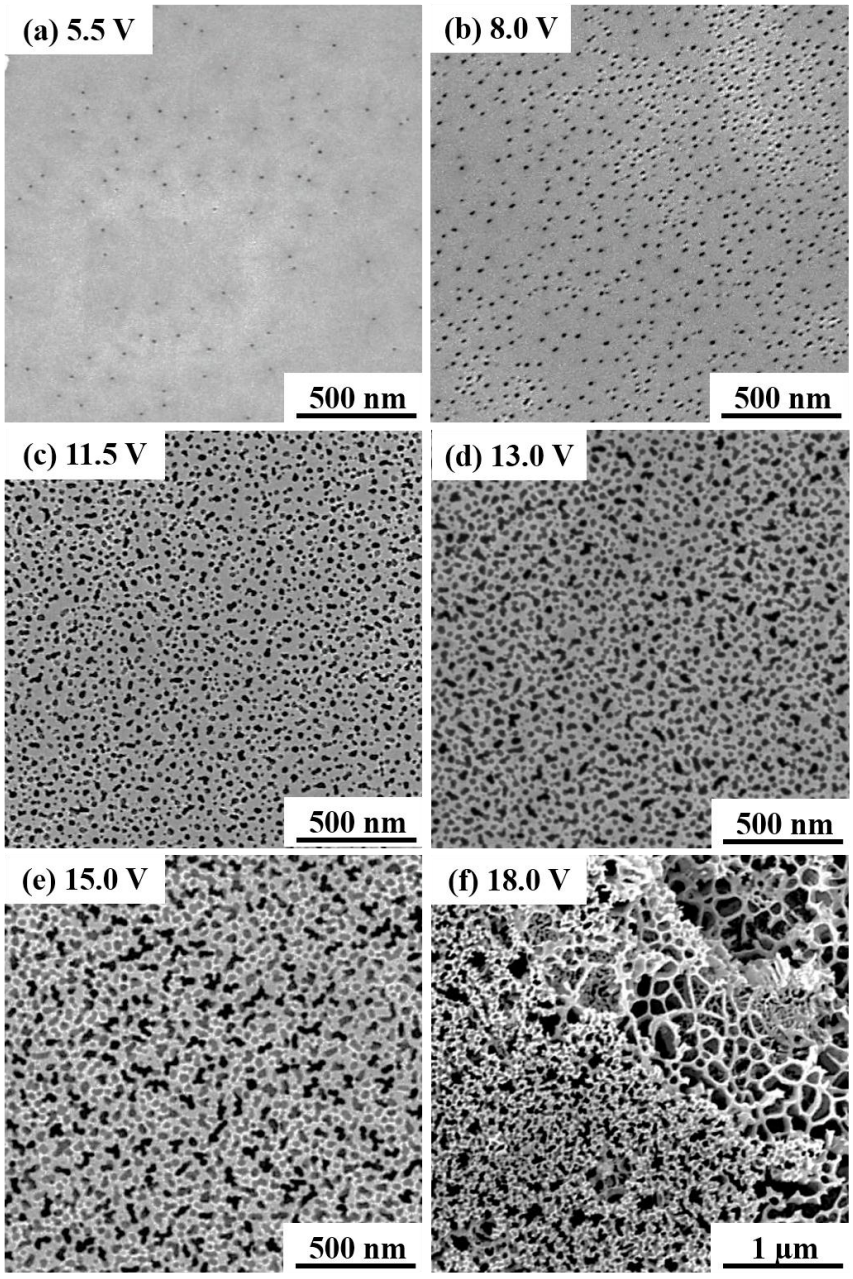

Figure 6.4: Top-view SEM images of the porous n-GaN etched at different potentials.

formation of pits at these defect sites, the enhanced electric field inside the pits accelerates the etching and eventually pores are formed. These defects, particularly threading dislocations, are influenced by layer coalescence during epitaxial growth and the local strain [15],[16], and are therefore distributed non-uniformly. The AlGaN intermediate layers used in our stack are known to reduce the threading dislocation density at the GaN surface to the range of $1\text{-}3\times10^{9}$ cm^{-2} [17],[18]. This agrees well to our observation in Figure 6.4 (a). For $U_{etch} \geq 11.5$ V, the pore initiation might also take place at some morphological defect sites such as microroughness, atomic steps, kinks and depressions [9],[19]. The initiation of surface pores can become a random process at high U_{etch} [20]-[22]. For $U_{etch} \geq 11.5$ V, the merging of surface pores is observed as a result of bigger pore size and the surface pore density. At $U_{etch} = 18.0$ V (Figure 6.4 (f)), a partially-broken GaN film is observed.

Figure 6.5 shows 45˚ SEM images of the 1.7 μm porous n-GaN layer etched at different potentials. The pore growth stops at the UID GaN layer, which corresponds to the current drop at the end of each j-t plot (Figure 6.3 (a)). As can be observed, the pore morphology strongly depends on the applied U_{etch}. Crystal-oriented pores, which are commonly observed in phosphor-based or arsenide-based III-V materials [23]-[25], have not been observed yet in the anodic etching of GaN. So far, the pores of n-GaN by anodic etching are all current-line-oriented (CLO). Branching pores and vertical pores are the two main types of CLO pores [8],[26],[27].

The growth mechanisms of these two pores are schematically illustrated in Figure 6.6. When the distance between two pores (d_w) is larger than the width of both their SCR ($2\times d_{sc}$), horizontal and vertical growth of pores are both possible, resulting in the branching structure (Figure 6.6 (a)). The growth of pores then depends on the local electric field and surface chemistry. In contrast, when the SCR of adjacent pores are so closely overlapped that electron tunneling from the VB to the CB is not possible, the lateral growth of pores is not possible (Figure 6.6 (b)). The pores then can only develop vertically. Consequently, branching pores are formed for lower U_{etch} (Figure 6.5 (b)) and the vertical pores are formed for higher U_{etch} (Figure 6.5 (e)).

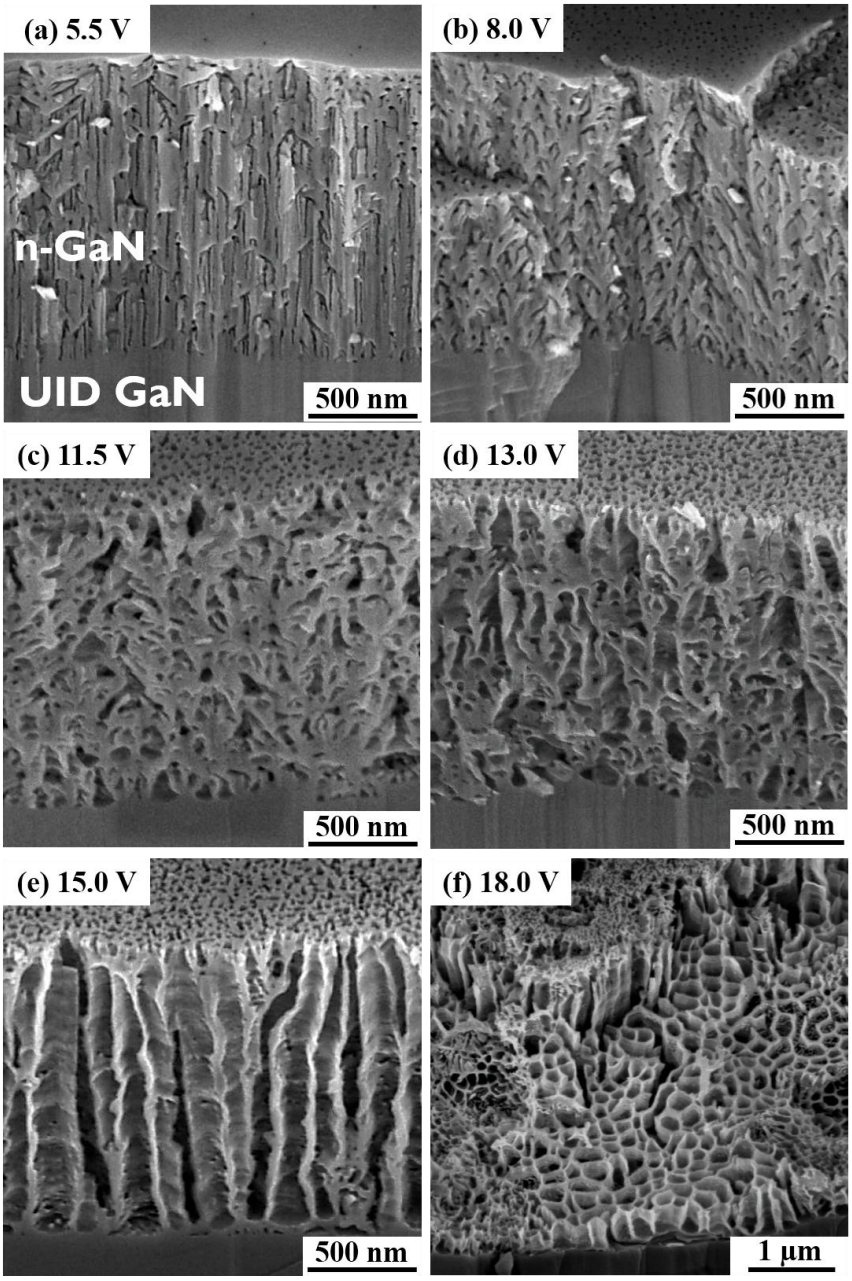

Figure 6.5: SEM images of the porous n-GaN etched at different potentials, imaged at 45˚.

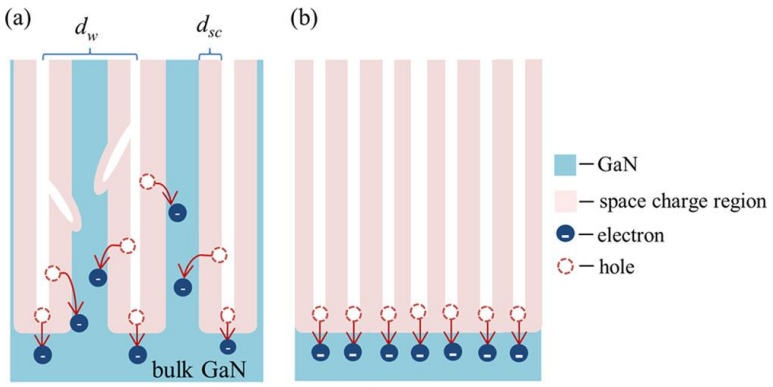

Figure 6.6: Schematic illustrations of hole supply mechanisms in anodic etching of (a) branching pores and (b) vertical pores [8].

Figure 6.7 shows the morphology of the porous GaN etched at U_{etch} = 15.0 V. The etching stopped at 200 s, and the rest etching condition is the same as the fully-porosified n-GaN in Figure 6.5 (e). The morphologies of the surface pores and the bulk pores are the same for both porous GaN. The etching of the pores starts from the surface and proceeds vertically. After the pores are formed, the morphology of the pores does not change with etching time. This confirm the model proposed in Figure 6.6. As the n-GaN between pores is fully depleted, the lateral etching is not possible. In this case, the etching only happens at the bottom of the pores. The same depth of all the pores indicates the same etching rate.

The morphology of the porous GaN shows a strong correlation to the j_{ss}-U_{etch} plot shown in Figure 6.3 (b). GaN etched using U_{etch} of the first current plateau gives the branching pore structure. A different hole supply mechanism is introduced when U_{etch} is at the second current plateau, resulting in the vertical straight pores. The pores etched at 11.5 V and 13.0 V are under the intermixing of both mechanisms.

Before the first current plateau, another type of pores is observed as shown in Figure 6.5 (a) (U_{etch} = 5.5 V). This morphology of this porous GaN is characterized by vertical pores with side branching pores. The vertical pores, either developed from the surface or the branching pores, grow straight down to the interface of UID GaN and n-GaN. The

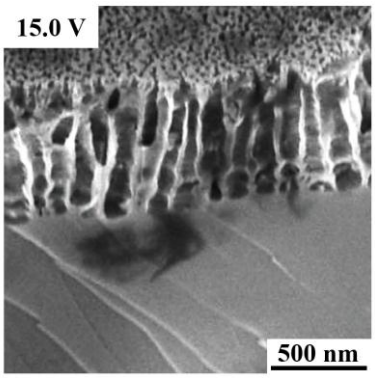

Figure 6.7: A SEM image of a porous n-GaN etched at 15.0 V, imaged at 45˚. The etching was stopped at the 200 s and the rest etching parameters were the same as the porous GaN in Figure 6.5 (e).

size of the pores etched at the lowest U_{etch} is the smallest for all conditions. This type of pore morphology is not reported in anodic etching of n-GaN so far.

For $U_{etch} \geq 11.5$ V, a surface transition layer is observed. The surface transition layer is characterized by a higher pore density and smaller pore size with respect to the bulk pore [14]. Figure 6.8 shows a top view SEM image of the porous GaN (U_{etch} = 15.0 V) with and without the transition layer. When pores are etched at a U_{etch}, the curvature of pore bottom, which determines the shape of the pore, should match the current distribution and the local electric field [14]. Therefore, the surface pores tend to reach the steady-state growth during the propagation by widening the pore dimension. The initiation and growth of the pores at the surface can possess different kinetics. The surface pores with faster kinetics may evolve to the bulk pores. The other surface pores are terminated in the transition layer when their SCR overlaps with others.

It is worth noting that we do not observe wire-like nanopores which are reported achievable for n-GaN grown on sapphire when U_{etch} is high (only the formation of vertical pores is possible) [4],[8]. Electropolishing happens for $U_{etch} \geq 18$ V in our work. This is much lower than reported U_{etch}, typically larger than 50 V, at similar carrier concentration level [8]. The different material properties of n-GaN grown on Si and on sapphire may result in a different etching mechanism during anodic etching. GaN on Si is under tensile

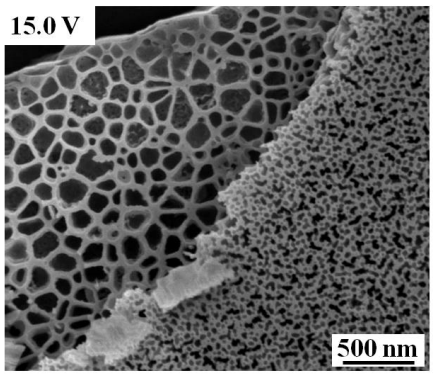

Figure 6.8: A top-view SEM image of the porous n-GaN etched at 15.0 V with (right) and without (left) the surface transition layer.

stress in contrast to the compressive stress for GaN on sapphire [28],[29]. Due to a larger thermal and lattice mismatch between GaN and Si, the defect density for GaN/Si is higher and the species of defects are different from GaN/sapphire [30],[31].

6.4 Photoelectrochemical properties of porous n-GaN

Finally we investigate photoelectrochemical properties of porous n-GaN. The photoelectrochemical measurements were performed using a UV-transparent quartz cell using a three-electrode configuration with a Ag/AgCl reference electrode (Metrohm). 0.1 M HBr and 0.2 M Na_2SO_4 (Sigma Aldrich) electrolyte solution was used, with Br^- acting as a hole scavenger to avoid photo-etching of GaN during photoelectrolysis. The solution was stirred using a magnetic stirring rod during measurements. The 150 W Xe lamp with the AM 1.5 filter was used as the light source. The light intensity of the integrated radiance spectrum illuminated at the sample surface was 63 mW/cm^2, measured by a thermopile detector. The details of the light source are referred to Section 2.3. To distinguish the applied potential used in the anodic etching and the photoelectrochemical measurement, the former one and latter one are denoted by U_{etch} and U, respectively.

We selectively present the j-U plots of some porous GaN and unetched GaN under illumination, as shown in Figure 6.9. The porous GaN samples were prepared by anodic

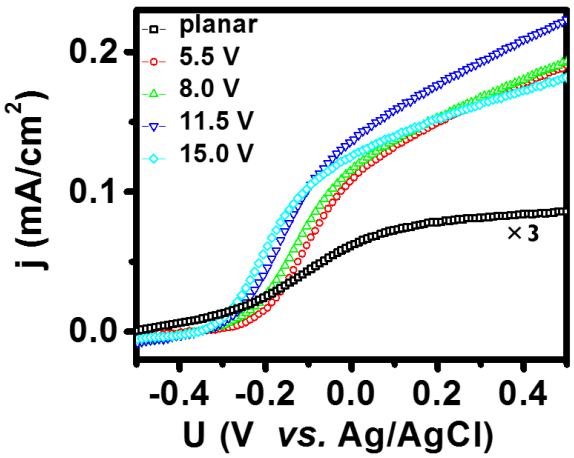

Figure 6.9: j-U plots under illumination for the unetched n-GaN and the 1.7 µm porous n-GaN samples etched at different potentials. The current density of the unetched GaN is multiplied by three for easier comparison. Solution: 0.1 M HBr + 0.2 M Na_2SO_4; *v*: 100 mV/s.

etching at 5.5 V, 8.0 V, 11.5 V and 15.0 V. Solution of 0.1 M HBr + 0.2 M Na_2SO_4 was used during the measurement. Table 6.1 lists the photoelectrochemical properties of these n-GaN photoanodes including the onset potential (U_{onset}), potential difference between the current onset and plateau ($\Delta U_{onset\text{-}plateau}$) and plateau current density ($j_{plateau}$). The definitions of U_{onset}, $U_{plateau}$ and $j_{plateau}$ are described in the footnotes of Table 1. Upon illumination, GaN absorbs supra-bandgap light and generates free photo-electrons and holes. For $U < U_{onset}$, electrons and holes recombine directly or via defects. For $U_{onset} < U < U_{plateau}$, some of photocarriers are separated by SCR and are participated in Br^- oxidation. For $U > U_{plateau}$, carrier recombination is suppressed; all photocarriers in SCR are separated and contribute to the photocurrent. The U_{onset} of porous GaN shifts more negative as U_{etch} increases, but are all more positive than the unetched GaN. The $\Delta U_{onset\text{-}plateau}$ of the porous GaN is independent of U_{etch}, and are all smaller by ~0.24 V than the unetched GaN.

The plateau photocurrent of n-GaN increases over 400% after porosification. The highest plateau current is found at U_{etch} = 11.5 V, which is higher than the unetched GaN by 470%. The abundant surface in the porous GaN leads to an increase in the total

Table 6.1: The photoelectrochemical properties of the planar GaN and the porous n-GaN.

U_{etch} (V)	U_{onset}[a] (V)	$\Delta U_{onset\text{-}plateau}$[b] (V)	$j_{plateau}$[a] (mA/cm^2)
planar	-0.447	0.560	0.025
5.5	-0.248	0.322	0.127
8.0	-0.285	0.327	0.126
11.5	-0.298	0.321	0.143
15.0	-0.314	0.320	0.127

[a]In the plateau region, the j-U relation is linear. Plateau current density ($j_{plateau}$) and plateau potential ($U_{plateau}$) are reached when the current density deviates this linearity by 5 %. The onset potential (U_{onset}) is reached when the current density reach 5 % of the $j_{plateau}$.
[b]$\Delta U_{onset\text{-}plateau} = U_{plateau} - U_{onset}$.

depletion region and therefore improves charge separation. Photo-holes in the charge neutral region recombine with electrons if they cannot reach the SCR. The small lateral dimension of GaN between pores reduces the charge neutral region; therefore less photo-holes are generated in the charge-neutral region of GaN. Surface recombination at defect sites is the main carrier recombination path in SCR. GaN grown by heteroepitaxy is well known for the rich intrinsic defects at the surface and the bulk [12],[13]. These rich defects reduces the lifetime of photo-holes. Therefore, a larger $\Delta U_{onset\text{-}plateau}$ is required to separate electrons and holes before carrier recombination occurs. As mentioned above, the anodic etching preferentially takes place at the defect sites (Figure 6.4). Consequently, the surface of the porous GaN is less defective than the planar GaN after anodic etching, resulting in a smaller $\Delta U_{onset\text{-}plateau}$. Although we cannot quantify the porosity of these porous n-GaN, the increase of porosity with U_{etch} is expected from the SEM images (Figure 6.5) and the Q-U_{etch} plot (Figure 6.3). The effective surface area also increases with U_{etch}, but is maximized at U_{etch} = 11.5 V (Figure 6.5). At U_{etch} = 15.0 V, the material loss is severe and leads to the degradation of the photoelectrochemical property.

Furthermore, we also discuss the photoelectrochemical properties of two different n-GaN layers before and after anodic etching. Figure 6.10 (a) shows the photocurrent

current-potential plots of Sample A and Sample B before porosification. A solution of 0.1 M HBr and 0.2 M Na_2SO_4 was used during the measurements, and the scan rate was 100 mV/s. Table 6.2 lists the photoelectrochemical properties of these two unetched photoanodes. $j_{plateau}$ of Sample B is higher than Sample A by 40%, and ΔUonset-plateau is shorter by 0.248 V. Here, we do not know the material properties of n-GaN for both samples except that the carrier concentration of the both samples is 6×10^{18} cm^{-3}. Sample A is the planar GaN used in Figure 6.9.

As the photocurrent plateau is reached, all photo-holes in the SCR of n-GaN are used in Br^- oxidation; surface recombination is suppressed. Due to the high doping level for the two samples, the width (W_{sc}) of SCR at the current plateau is small (i.e. W_{sc} = ~15 nm at 0.4 V). The absorption depth of UV light for GaN is ~100 nm considering α_{GaN} = 10^5 cm^{-1} [32]. Therefore, for the planar GaN many photo-holes are generated in the charge-neutral region. In the charge neutral region, photo-holes recombine with electrons unless they reach the SCR. For the n-GaN layer, whose minority carrier lifetime is longer, photo-holes of charge neutral region are more likely to reach the SCR, leading to a higher photocurrent. In the charge neutral region, carrier recombination is either a direct process or a trap-assisted process, as described in Section 3.8. The direct recombination rate is the same for both Sample A and B since the recombination coefficient is independent of

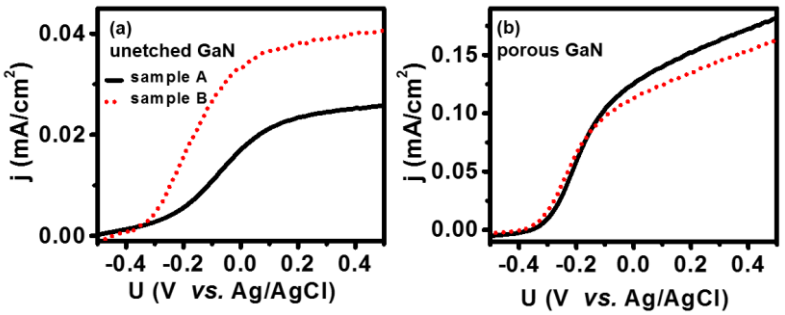

Figure 6.10: j-U plots under illumination for Sample A (concrete) and Sample B (dashed) (a) before and (b) after anodic etching (U_{GaN-Pt} = 15.0 V). Solution: 0.1 M HBr and 0.2 M Na_2SO_4; v = 100 mV/s.

Table 6.2: Photoelectrochemical properties of the unetched and porous n-GaN samples.

U_{etch} (V)	U_{onset}[a] (V)	$\Delta U_{onset\text{-}plateau}$[a] (V)	$j_{plateau}$[a] (mA/cm^2)
unetched sample A	-0.447	0.560	0.025
unetched sample B	-0.365	0.312	0.035
porous sample A	-0.314	0.320	0.127
porous sample B	-0.345	0.260	0.100

[a]The definition of the U_{onset}, $\Delta U_{onset\text{-}plateau}$ and $j_{plateau}$ see the footnote of Table 1.

material quality [33],[34]. Therefore, the defect density of Sample A may be higher than Sample B or some specific defects in Sample A may be more effective in carrier recombination. Furthermore, $\Delta U_{onset\text{-}plateau}$ of unetched Sample B is smaller than unetched Sample A by 0.248 V. This indicates that surface recombination in Sample A is stronger than Sample B.

Both samples were potentiostatically etched at 15.0 V in a 0.5 M H_2SO_4 solution in the dark using a two-electrode configuration. The full 1.7 μm layer was porosified for both n-GaN. The photocurrent-potential plots of the porous sample A and porous sample B are shown in Figure 6.10 (b). The photoelectrochemical properties of these two porous GaN are listed in Table 6.2. Both samples have a similar U_{onset}. $\Delta U_{onset\text{-}plateau}$ of Sample B is smaller by 0.06 V and $j_{plateau}$ is lower by 27% with respect to Sample A. The j-U curve of Sample A is more rounded for the potential around $U_{plateau}$ compared to Sample B. Therefore, Sample A and sample B seem to have a distinct $\Delta U_{onset\text{-}plateau}$ and $j_{pleateau}$. However, if we compare the photocurrent in the plateau (i.e. U = 0.4 V), the photocurrent of Sample B is only higher than Sample A by 13%.

In Figure 6.10 (a), we can conclude that carrier recombination in the bulk of GaN is stronger for Sample A. The j_{ph} of Sample A is higher than Sample B by 40% at U = 0.4 V. However, after the porosification, the j-U characteristics become more similar for both samples. The j_{ph} in the current plateau (U = 0.4 V) of Sample A is only higher than Sample B by 13%. The increased total area of the SCR and decreased area of the charge

neutral region in the porous GaN suppress carrier recombination for both sample A and sample B. Therefore, the photoelectrochemical properties of these two samples after porosification becomes less different.

6.5 Summary

In this chapter, we have fabricated porous n-GaN from a GaN epilayer grown on Si using anodic etching in 0.5 M H_2SO_4 solution in the dark. Anodic etching of n-GaN is first discussed using chronoamperometry and cyclic voltammetry. In the chronoamperograms, transient current oscillates before the steady-state condition is reached, which results from n-GaN oxidation and oxide dissolution. In the cyclic voltammograms, two anodic current plateaus are observed, which indicate different hole supply mechanisms.

The pore morphology shows distinctive differences depending on the applied potential: from narrow branching pores to wide parallel pores. Different etching mechanisms are observed for pore initiation at the surface and pore evolution in the bulk of GaN. The photoelectrochemical properties of the porous n-GaN layers are discussed. The plateau photocurrents for all the porous GaN increase over 4 times; the potential difference between the photocurrent onset and plateau is reduced by 0.24 V with respect to the unetched n-GaN. The increased depletion region of the porous GaN facilitates charge separation. Less photo-holes are generated in charge neutral region, where carrier recombination is strong. Carrier recombination in the GaN layer and at the surface are therefore suppressed after porosification.

6.6 References

[1] D. Zhuang and J. H. Edgar, *Mat. Sci. Eng. R*, **48**, 1 (2005).
[2] A. M. Basilio, Y.-K. Hsu, W.-H. Tu, C.-H. Yen, G.-M. Hsu, O. Chyan, Y. Chyan, J.-S. Hwang, Y.-T. Chen, L.-C. Chen, and K.-H. Chen, *J. Mater. Chem.*, **20**, 8118 (2010).
[3] C. Youtsey, L. T. Romano, and I. Adesida, *Appl. Phys. Lett.*, **73**, 797 (1998).
[4] M. J. Schwab, D. Chen, J. Han, and L. D. Pfefferle, *J. Phys. Chem. C*, **117**, 16890 (2013).

[5] L.-W. Jang, D.-W. Jeon, A. Y. Polyakov, H.-S. Cho, J.-H. Yun, D.-S. Jo, J.-W. Ju, J.-H. Baek, and I.-H. Lee, *Appl. Phys. Express*, **6**, 6 (2013).
[6] G. Gautier, D. Valente, J. Biscarrat, and A. Yvon, *ECS J. Solid State Sci. Technol.*, **2**, 146 (2013).
[7] S.-W. Ryu, Y. Zhang, B. Leung, C. Yerino, and J. Han, *Semicond. Sci. Technol.*, **27**, 015014 (2012).
[8] D. T. Chen, H. D. Xiao, and J. Han, *J. Appl. Phys.*, **112**, 064303 (2012).
[9] W. J. Tseng, D. H. van Dorp, R. R. Lieten, P. M. Vereecken, and G. Borghs, *"*Nanoporous n-GaN photoanodes by anodic etching", *J. Phys. Chem. C* (submitted).
[10] K. Cheng, M. Leys, S. Degroote, M. Germain, and G. Borghs, *Appl. Phys. Lett.*, **92**, 192111 (2008)**.**
[11] Y. Xiao, X. Li, H.-D. Um, X. Gao, Z. Guo, and J.-H. Lee, *Electrochim. Acta*, **74**, 93 (2012).
[12] A. Sakai, H. Sunakawa, and A. Usui, *Appl. Phys. Lett.*, **71**, 2259 (1997).
[13] G. P. Dimitrakopulos, P. Komninou, and R. C. Pond, *Phys. Status Solidi B*, **227**, 45 (2001).
[14] X. G. Zhang, *J. Electrochem. Soc.*, **138**, 3750 (1911).
[15] K. Cheng, M. Leys, S. Degroote, B. Van Daele, S. Boeykens, J. Derluyn, M. Germain, G. Van Tendeloo, J. Engelen, and G. Borghs, *J. Electron. Mat.*, **35**, 592 (2006).
[16] X. H. Wu, L. M. Brown, D. Kapolnek, S. Keller, B. Keller, S. P. DenBaars, and J. S. Speck, *J. Appl. Phys.*, **80**, 3228 (1996).
[17] A. Able, W. Wegscheider, K. Engl, and J. Zweck, *J. Cryst. Growth*, **276**, 415 (2005).
[18] H. Marchand, L. Zhao, N. Zhang, B. Moran, R. Coffie, U.K. Mishra, J.S. Speck, S.P. DenBaars, and J.A. Freitas, *J. Appl. Phys.*, **89**, 7846 (2001).
[19] J. Hertkorn, P. Brueckner, S. B. Thapa, T. Wunderer, F. Scholz, M. Feneberg, and K. Thonke, *J. Crys. Growth*, **308**, 30 (2007).
[20] M. I. J. Beale, J. D. Benjamin, M. J. Uren, N. G. Chew and A. G. Cullis, *J. Cryst. Growth*, **73**, 622 (1985).
[21] X. G. Zhang, *J. Electrochem. Soc.*, **138**, 3750 (1991).
[22] P. C. Searson, J. M. Macaulay, and F. M. Ross, *J. Appl. Phys.*, **72**, 253 (1992).
[23] S. Langa, I.M. Tiginyanu, J. Carstensen, M. Christophersen, and H. Foll, *Electrochem. Solid State Lett.*, **3**, 514 (2000).
[24] F. M. Ross, G. Oskam, P. C. Searson, J. M. Macaulay, and J. A. Liddle, *Philos. Mag. A*, **75**, 525 (1997).
[25] M. A. Stevens-Kalceff, I.M. Tiginyanu, S. Langa, H. Foll, and H.L. Hartnagel, *J. Appl. Phys.*, **89**, 2560 (2001).
[26] G. C. John and V. A. Singh, *Phys. Rep.*, **263**, 93 (1995).
[27] X. G. Zhang, *J. Electrochem. Soc.*, **138**, 3750 (1991).
[28] L. Liu and J. H. Edgar, *Mat. Sci. Engin. R*, **37**, 61 (2002).
[29] L. Zhang, K. Cheng, S. Degroote, M. Leys, M. Germain, and G. Borghs, *J. Appl. Phys.*, **108**, 073522 (2010).
[30] O. Ambacher, *J. Phys. D: Appl. Phys.*, **31**, 2653 (1998).
[31] M. O. Manasreh (ed.) and L. T. Ferguson (ed.) "III-Nitride Semiconductors: Growth", CRC Press (2013).

[32] J. F. Muth, J. H. Lee, I. K. Shmagin, R. M. Kolbas, H. C. Casey, B. P. Keller, U. K. Mishra, and S. P. DenBaars, *Appl. Phys. Lett.*, **71**, 2572 (1997).
[33] A. Dmitriev and A. Oruzheinikov, *J. Appl. Phys.*, **86**, 3241 (1999).
[34] J. S. Im, A. Moritz, F. Steuber, V. Harle, F. Scholz, and A. Hangleiter, *Appl. Phys. Lett.*, **70**, 631 (1997).

CHAPTER 7

Strain relaxation in GaN pillars

Chapter 7. Strain relaxation in GaN pillars

7.1 Introduction

Since Fujishima and Honda demonstrated the direct photoelectrolysis using a TiO_2 photoanode in the 1970s [1], photoelectrochemical and photocatalytic properties of many semiconductors have been investigated extensively [2]. GaN has drawn significant attention for the use in photoelectrolysis. Self-driven photoelectrolysis is possible using GaN because of the favorable energetic alignment to the redox potentials of water. However, due to the large bandgap (3.4 eV), most of the solar light cannot be absorbed by GaN.

The incorporation of indium in GaN is one of the main schemes to reduce the bandgap. The compound of InN and GaN has a direct bandgap of 0.7-3.4 eV, thereby covering the complete solar spectrum [3],[4]. However, the growth of indium-rich InGaN with low dislocation density is challenging. The difference in the optimized growth temperature of GaN and InN is as much as 400˚C, resulting in a large thermodynamic miscibility gap [5]. The difference in vapor pressure suppress the incorporation of indium into InGaN during growth [6]. Moreover, the lattice mismatch between GaN and InN (10%) introduces a large stress in the layer. This stress limits the critical layer thickness, and is typically released in the form of dislocations in the layer [7]. In contrast to the conventional epitaxy on a planar template, the growth of indium-rich InGaN on GaN nanopillars and nanowires has been recently demonstrated [8]-[10]. The abundant free surface area and high-aspect ratio results in the strain-relieving properties of the nanostructures. More indium could therefore be incorporated in the compound using these nanostructure templates. The strain relaxation through the formation of structural defects could be significantly suppressed for InGaN grown on the GaN nanostructures.

Insight in the strain relaxation of nanostructured GaN is therefore important for the development of InGaN growth on nanostructures. Measuring the strain at the nanostructure surface is however challenging. It requires high accuracy and good vertical

spatial resolution. Both (micro)photoluminescence (PL) or (micro-)Raman spectroscopy have been used to investigate strain relaxation in GaN (nano)pillars [11]-[13]. However, the strain state and strain variation at the surface of nanostructures cannot be precisely determined due to a relatively long penetration depth of the probing light beam in these technologies (typically 100-200 nm for PL). Grazing incidence in-plane X-ray diffraction (GIIXD) is widely exploited to characterize the in-plane alignment and lattice spacing of nanostructures [14]-[16]. During the GIIXD measurements, the incident angle of X-ray is set to be lower than the critical angle of the sample for total internal reflection. The penetration depth of the X-ray is typically less than 10 nm [17], resulting in the high resolution of the vertical depth. Therefore, the lattice constant at the top of nanostructures can be precisely measured.

In this section, strain relaxation of the GaN nanopillars was studied. The strain at the top plane of the pillars (~ 5 nm) was measured using GIIXD. The strain relaxation and strain distribution of the pillars were simulated using a finite element method. The impact of the pillar morphology on the strain relaxation were also discussed. Some results of this chapter are published in Ref. [18].

7.2 Sample fabrication: nanopillars at different heights

Metal organic chemical vapor deposition (MOVPE) was used to grown the GaN epilayer on the Si (111) substrate [19]. The GaN epilayer was used to fabricate the tapered nanopillars by dry etching using self-assembled Ni clusters as mask [18],[20]. The fabrication process of the GaN nanopillars is addressed in Section 4.2. The thicknesses of the Ni and SiO_2 film were respectively 10 nm and 100 nm. The samples were annealed at 850°C in N_2 environment for 1 minute to form Ni clusters. The etching parameter of the SiO_2 etch was: RF power/ICP power/SF_6 flow/ O_2 flow/chamber pressure/temperature/time: 50 W/300 W/ 100 sccm/10 sccm/10 mtorr/20 ˚C/3 mins. The etching parameter of the GaN etch was: RF power/ICP power/Cl_2 flow/Ar flow/chamber pressure/temperature: 100 W/50 W/ 15 sccm/4 sccm/5 mtorr/20 ˚C. The etching rate of SiO_2 and GaN were 50 nm/min and 140 nm/min, respectively. Figure 7.1 (a) and (b) show

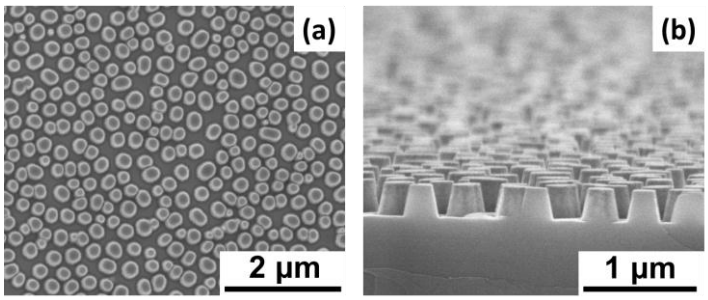

Figure 7.1: SEM images of GaN tapered nanopillars at (a) top view and (b) at 80°.

the SEM images of the GaN tapered pillars at top view and at 80°, respectively. The average top diameter is 250 nm with a size dispersion of 40 nm. The bottom diameter of the tapered pillars is increased by 0.4 nm when the pillar height is increased by 1 nm ($\emptyset_{\text{bottom}} = \emptyset_{\text{top}} + 0.4 \times \text{pillar height in nm}$).

7.3 Strain assessment by in-plane X-ray diffraction measurements

The in-plane lattice spacing was measured with a standard laboratory high resolution X-ray diffractometer (Panalytical X'Pert) in the grazing incidence configuration. The schematic illustration of the GIIXD measurement of GaN nanopillars is shown in Figure 7.2. The incoming X-ray beam angle (α_i) was chosen below the critical angle (α_c) of the total reflection to limit the penetration depth. The diffraction angle (2θ) was measured by using a triple axis monochromator in front of the detector. The energy of the X-ray beam was 8047.8 eV. For the in-plane XRD configuration, the incident beam angle was fixed at 0.13° which is below the critical angle (0.33°) for the total external reflection. The penetration depth of the incoming X-ray beam in GaN is calculated to be 5 nm [17]. Because this configuration lowers the intensity of the diffracted X-ray beam that reaches the detector, a relatively long integration time of 77 seconds per step was chosen to achieve sufficient intensity and to reduce the noise level.

Figure 7.3 (a) shows the normalized XRD spectra of the GaN tapered pillars with different pillar heights, scanned at the GaN $(10\bar{1}0)$ reflection. For the GaN pillars, two

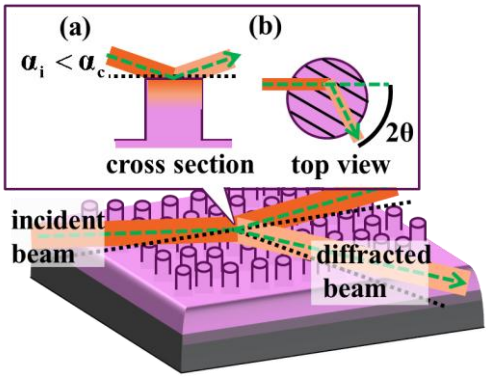

Figure 7.2: Schematic illustration of grazing incidence in-plane X-ray diffraction measurement of GaN nanopillars. Inset (a) shows the cross section of the pillar with the presence of light evanescing into the pillar and inset (b) shows the top view of the pillar with the presence of diffracting planes.

peaks were observed in the XRD spectra, and were fitted by two Gaussian curves. The right peak of the spectrum is attributed to the X-ray diffraction at the top surface of GaN pillars. With increasing pillar height, the diffraction peak position shifts towards higher 2θ values, indicating a reduction in the in-plane spacing. The sub-peak centered at 16.174° in the pillar spectra, which shifts slightly from the position of as-grown GaN peak (16.169°), originates from the X-ray diffraction at the edge of the pillar samples. Limited by the fabrication approach, the sample edge was not covered by the Ni clusters after annealing, and was hence etched blankly. Although the ICP dry etching etches uniformly, the etched surface can be still roughened from few angstroms to few nanometers [21], resulting in the surface which is slightly relaxed than the initial epilayer. The full width at half maximum (FWHM) of the pillar spectra is found all larger than the as-grown GaN. Increased FWHM of the XRD spectrum for GaN nanostructures etched by dry etching is commonly observed [22],[23]. The bombardment of energetic ions accelerates the removal of atoms at the surface during dry etching, and simultaneously damage the surface, deteriorating the crystalline quality of the nanostructure surface.

The in-plane lattice spacing (a-spacing) of the samples was derived from the angular position of the XRD peak using Gaussian fit. The a-spacing as a function of the pillar height is shown in Figure 7.3 (b). The error is the fitting error. The residual in-plane stress of the GaN epilayer grown on Si, whose a-spacing is 3.1941 Å, was calculated to be 780 MPa. The in-plane strain relaxes exponentially as a function of the pillar height. The a-spacing (a) as a function of the pillar height (x in nm) can be fitted by $a(x) = a_0 + be^{-\frac{x}{R}}$, resulting in the following fit: a_0 = 3.1892 Å, b = 0.0050 Å, and R = 22.0 nm. For large pillar heights ($x >> R$), this results in: $a(\infty) = a_0$, indicating that a_0 is the in-plane spacing

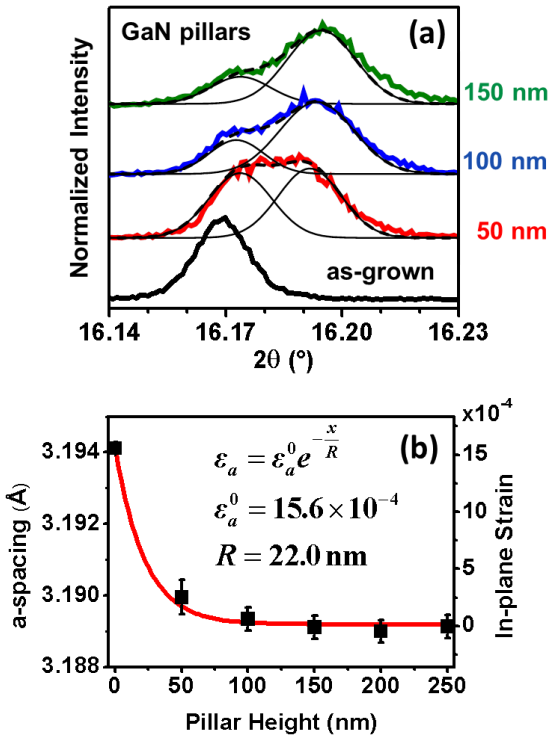

Figure 7.3: (a) Normalized in-plane XRD spectra of a planar GaN and GaN pillars at different pillar heights. Each spectrum of the pillars was fitted by two Gaussian curves. (b) Measured a-spacing and corresponding in-plane strain as a function of the pillar height. The strain *vs.* the pillar height was fitted by an exponential curve and the fitting parameters are shown in the figure.

Table 7.1: Measured lattice spacings and calculated in-plane stresses (σ_a)/strains (ε_a) of the unetched GaN epilayers and the GaN pillars (diameter = 250 nm) grown on Si and sapphire, derived from the in-plane XRD measurements.

GaN Sample	a-spacing (Å)	c-spacing (Å)	σ_a (MPa)	ε_a (%)
unetched GaN/sapphire	3.1847	5.1881	-660	-0.140
unetched GaN/Si	3.1941	5.1816	780	0.156
200 nm pillars/sapphire	3.1889	--	~0	-0.008
250 nm pillars/Si	3.1892	--	~0	0.002

of fully-relaxed GaN. The strain relaxation as a function of the pillar height can therefore be described by the equation

$$\varepsilon_a(x) = \frac{a(x)-a_0}{a_0} = \varepsilon_a^0 e^{-\frac{x}{R}} \tag{7.1}$$

For x equal to R, the strain reduces to 1/e (37.3%). The parameter R can therefore be defined as the relaxation depth at which the strain relaxes to 1/e of the initial strain (ε_a^0). The R depends on the pillar geometry and the material properties. In the case of GaN tapered pillars of 250 nm diameter at the top, we find a relaxation depth of 22.0 nm.

Additional to GaN grown on Si, we have fabricated the tapered nanopillars from a GaN epilayer grown on sapphire substrates. The XRD results of the GaN pillars and epilayers on Si and sapphire are summarized in Table 7.1. The difference in the lattice spacing and the thermal expansion for Si and sapphire substrates results in different residual strains of the GaN epilayers. The residual strain of the GaN layer grown on the sapphire (Si) is compressive (tensile). However, the measured a-spacings of the top of the pillars both converge to the same value which characterizes strain-free GaN.

7.4 Strain simulation using finite element method

The strain distribution in the GaN tapered pillars was simulated using a finite element method (FEM), based on the Hooke's law and elastic constants of GaN [24]. The in-plane stress of the GaN bulk was set to 780 MPa, as obtained by the GIIXRD measurement. The top diameter of the tapered pillar was set to 250 nm, and the bottom diameter was set to follow the equation: $\emptyset_{\text{bottom}} = 250 + 0.4 \times \text{pillar height}$. The simulated strain distribution in a fully-relaxed ($\emptyset_{top}/\emptyset_{bottom}$/height: 250/350/250 nm) and partially-relaxed ($\emptyset_{top}/\emptyset_{bottom}$/height: 250/270/50 nm) GaN pillar are illustrated in Figure 7.4 (a) and (b), respectively. In both cases, the surface in the neighborhood of the base around the pillar shows increased tensile strain (light orange and light yellow part), resulting from the inward pulling of the pillar. From our simulation, it is clear that the strain relaxation is highly location-dependent for the partially-relaxed pillars. The part more accessible to the surface is more flexible to release the strain. For a fully-relaxed pillars, the strain at top plane of the GaN pillars is zero.

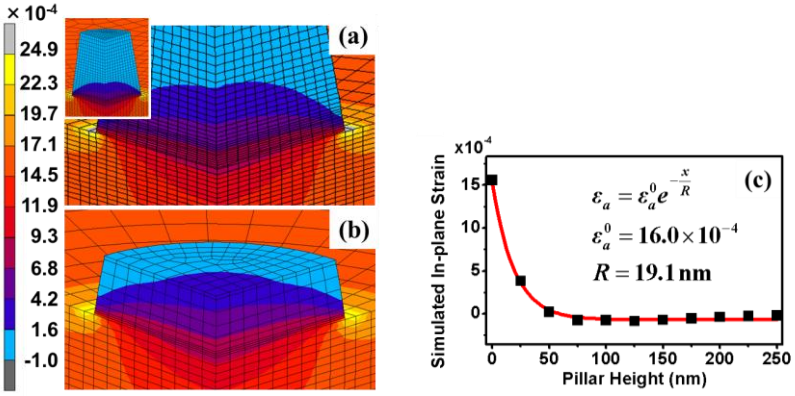

Figure 7.4: Simulated strain distribution of (a) a fully relaxed GaN pillar ($\emptyset_{top}/\emptyset_{bottom}$/height: 250/350/250 nm) and (b) a partially-relaxed pillar ($\emptyset_{top}/\emptyset_{bottom}$/height: 250/270/ 50 nm) on a GaN bulk whose initial in-plane stress is 780 MPa, and (c) the average in-plane strain at the top of the pillar as a function of the pillar height with the fitting curve and fitting parameters presented.

Figure 7.4 (c) shows the simulated average in-plane strain at the top plane of the pillar as a function of the pillar height. The strain relaxation was fitted using Eq. (7.1); the fitted R is 19.1 nm. The R obtained from the simulation is smaller than that of the XRD measurement. This discrepancy can be ascribed by the variation of the pillar morphology in the pillar array.

To study the influence of the geometric shape on the strain relaxation of the pillar, the strain relaxation of different nanostructure models have been simulated: a small circular cylinder (Ø = 250 nm), a big circular cylinder (Ø = 350 nm), and an elliptic cylinder ($Ø_{short}/Ø_{long}$ = 250/350 nm). The simulated in-plane strain as a function of the pillar height is shown in Figure 7.5. The height of the cylinders varies from 0 to 250 nm. The in-plane strain at the top of the pillar was simulated and was then averaged. The averaged strain relaxation as a function of the pillar height was fitted by Eq. (7.1). The fitted R at each

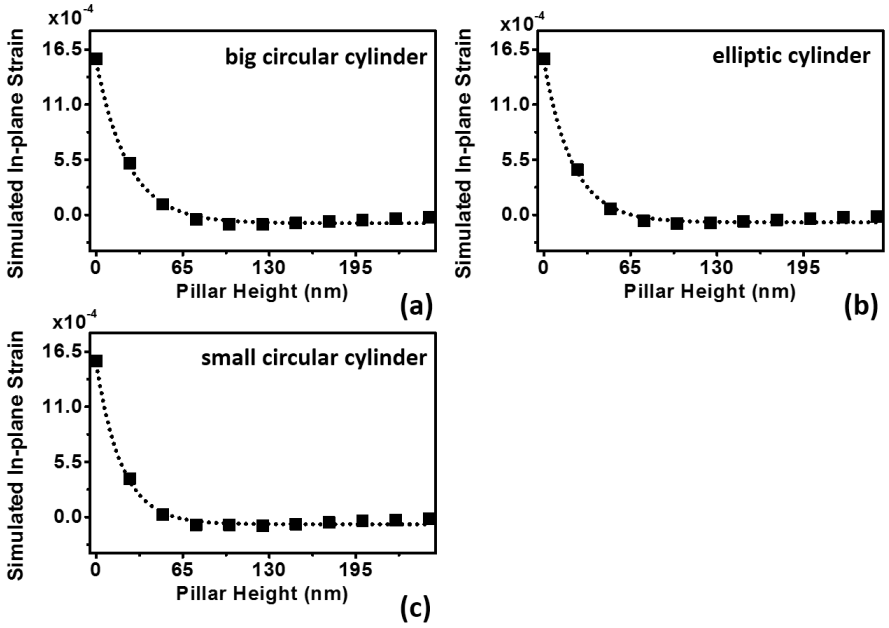

Figure 7.5: Average simulated in-plane strain at the top of the pillar as a function of the pillar height with its exponential fit for (a) a circular cylinder, (b) an elliptic cylinder and (c) a truncated cone. The fitting results and the geometry models are described in Table 7.2.

Table 7.2: Relaxation depths (R) obtained from three different pillar geometries. Three models from left to right are two circular cylinders and an elliptic cylinder. The R is defined by the equation: $\varepsilon_a(x) = \varepsilon_a^0 e^{-x/R}$, where ε_a^0 and x are the initial strain of unetched GaN epilayer and the pillar height, respectively.

pillar geometry (top view)		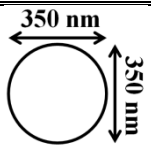	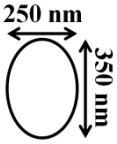
R (nm)	17.6	24.1	21.4

structure model are listed in Table 7.2. The strain relaxation is found to be sensitive to the nanostructure geometry. The increase of the pillar diameter prolongs the strain relaxation. The SEM images in Figure 7.1 show the morphology of the tapered pillars. The variation of the pillar size disperses the strain relaxation rate, which explains the discrepancy in the fitted R between the experiment and the simulation. The nanostructure fabrication can be further improved by the utilization of different mask or lithography in the future work. Nevertheless, the capability of the in-plane XRD in the strain evaluation at the very surface of the nanostructure is successfully demonstrated. With a systematic structure design, this technique can be further employed to study the strain relaxation of the nanostructures experimentally.

7.5 Summary

In this chapter, the strain state at the surface of nanostructures was measured by exploiting the in-plane XRD. The GaN nanopillars were fabricated by dry etching of a highly strained, epitaxially grown GaN layer using self-assembled Ni as mask. The in-plane lattice spacing of the top 5 nm of the pillars was accurately determined by the grazing incidence XRD with an incoming angle below the critical angle of reflection. The strain of the top plane of the pillars as a function of the pillar height was investigated and shows an exponential relaxation which can be described by a single parameter, the

relaxation depth. Moreover, we simulated the strain relaxation and distribution in the GaN nanopillars. A non-uniform strain distribution is found at the top of the partially-relaxed pillars. The simulated strain relaxation shows good agreement with the experimentally observed exponential relaxation. The impact of the pillar morphology on the strain relaxation has been also discussed.

7.6 References

[1] A. Fujishima and K. Honda, *Nature*, **238,** 37 (1972).
[2] A. Kudo and Y. Miseki, *Chem. Soc. Rev.*, **38,** 253 (2009).
[3] C. Hahn, Z. Zhang, A. Fu, C. H. Wu, Y. J. Hwang, D. J. Gargas, and P. Yang, *ACS Nano*, **5**, 3970 (2011).
[4] F. K. Yam, Z. Hassan, *Superlattices Microstruct.*, **43**, 1 (2008).
[5] G. B. Stringfellow, *J. Cryst. Growth*, **312**, 735 (2010).
[6] T. Nagatomo, T. Kuboyama, H. Minamino, O. Omoto, *Jpn. J. Appl. Phys.*, **28**, L1334 (1989).
[7] K. Cheng, M. Leys, S. Dergoote, B. Van Daele, S. Boeykens, J. Derluyn, M. Germain, G. Van Tendeloo, J. Engelen, and G. Borghs, *J. Electron. Mater.*, **35**, 592 (2006).
[8] H.-W. Lin, Y.-J. Lu, H.-Y. Chen, H.-M. Lee, and S. Gwo, *Appl. Phys. Lett.*, **97**, 073101 (2010).
[9] H. Sekiguchi, K. Kishino, and A. Kikuchi, *Appl. Phys. Lett.*, **96**, 231104 (2010).
[10] A.-L. Bavencove, G. Tourbot, J. Garcia, Y. Désières, P. Gilet, F. Levy, B. André, B. Gayral, B. Daudin and Le Si Dang, *Nanotechonology*, **22**, 345705 (2011).
[11] Y. D. Wang, S. J. Chua, S. Tripathy, M. S. Sander, P. Chen, and C. G. Fonstad, *Appl. Phys. Lett.*, **86**, 071917 (2005).
[12] N. Thillosen, K. Sebald, H. Hardtdegen, R. Meijers, R. Calarco, S. Montanari, N. Kaluza, J. Gutowski, and H. Lüth, *Nano Lett.*, **6**, 704 (2006).
[13] X. H. Wang, J. Q. Ning, S. J. Xu, and H. W. Choi1, *J. Appl. Phys.*, **110**, 093111 (2011).
[14] W. K. Koh, A. C. Bartnik, F. W. Wise, and C. B. Murray, *J. Am. Chem. Soc.*, **132**, 3909 (2010).
[15] L. Horák, V. Holý, C. R. Staddon, N. R. S. Farley, S. V. Novikov, R. P. Campion, and C. T. Foxon, *J. Appl. Phys.*, **104**, 103504 (2008).
[16] O. Landré, D. Camacho, C. Bougerol, Y. M. Niquet, V. Favre-Nicolin, G. Renaud, H. Renevier, and B. Daudin, *Phys. Rev. B*, **81**, 153306 (2010).
[17] H. Dosch, *Phys. Rev. B*, **35**, 2137 (1987).
[18] W. J. Tseng, M. Gonzalez, L. Dillemans, K. Cheng, S. J. Jiang, P. M. Vereecken, G. Borghs, and R. R. Lieten, *Appl. Phys. Lett.*, **101**, 253102 (2012).
[19] K. Cheng, M. Leys, S. Degroote, M. Germain, and G. Borghs, *Appl. Phys. Lett.* **92**, 192111 (2008).

[20] W. J. Tseng, D. H. van Dorp, R. R. Lieten, B. Mehta, P. M. Vereecken, and G. Borghs, *ECS Electrochem. Lett.*, **2**, H51 (2013).
[21] C. H. Chen, S. Keller, E. D. Haberer, L. Zhang, S. P. DenBaars, E. L. Hu, U. K. Mishra, and Y. Wu, *J. Vac. Sci. Technol. B*, **17**, 2755 (1999).
[22] J. Y. Chen, C. J. Pan, and G. C. Chi, *Solid-State Electron.*, **43**, 649 (1999).
[23] S. Keller, C. Schaake, N. A. Fichtenbaum, C. J. Neufeld, Y. Wu, K. McGroddy, A. David, S. P. DenBaars, C. Weisbuch, J. S. Speck, and U. K. Mishra, *J. Appl. Phys.*, **100**, 054314 (2006).
[24] A. Polian, M. Grimsditch, and I. Grzegory, *J. Appl. Phys.*, **79**, 3343 (1996).

CHAPTER 8

Summary and outlook

Chapter 8. Summary and outlook

8.1 Summary

Hydrogen, as a green and renewable chemical fuel, has attracted significant attention for the generation of electricity and motive power. Water photoelectrolysis, using semiconductor photo-electrodes, is a sustainable and renewable approach to produce hydrogen. The solar energy is directly converted and stored in chemical bonds. GaN-based semiconductors are attractive for the use in photoelectrolysis. GaN satisfies the energetic requirement for self-driven photoelectrolysis. By indium incorporation, the bandgap of the semiconductors can be further reduced (0.7-3.4 eV), thereby covering the complete solar spectrum. Photo-holes, generated in n-GaN under illumination, participate in one of the following activities: (a) oxidation of reductants in the solution, (b) photo-corrosion of GaN, (c) surface recombination and (d) carrier recombination in the bulk. Only the first process is desirable in the application of photoelectrolysis. In this dissertation, different etching technologies and surface treatments, to modify an n-GaN epilayer, have been applied to suppress processes (c) and (d). The thesis is summarized as follows:

In Chapter 3, the theory of semiconductor electrochemistry including the interfacial band diagram alignment, the interfacial charge transfer and the Mott-Schottky plot were briefly introduced using n-GaN photoanodes as examples. Cyclic voltammetry, chronoamperometry and impedance spectroscopy have been used to characterize n-GaN photoanodes. Photo-corrosion of n-GaN during photoelectrolysis is more favorable than water oxidation. To suppress the photo-corrosion process, Br^- has been used as a sacrificial reducing agent.

In Chapter 4, we have improved charge separation of n-GaN by surface nanoroughening. The GaN nanopillars were fabricated by dry etching of an n-GaN epilayer, using self-assembled Ni clusters as a mask. The plateau photocurrent (j_{ph}) of n-GaN in the photoelectrochemical measurements increased as a function of the pillar

height. The plateau j_{ph} of the 1.6 µm high pillars is enhanced by 84% with respect to planar GaN. However, dry etching damages GaN surface and creates surface defects. Consequently, a larger potential difference between current onset and plateau ($\Delta U_{onset-plateau}$) is required. The photoluminescence intensity of the near-bandedge transition is ~50 % lower for surface-damaged GaN than for unetched GaN as a result of promoted non-radiative recombination.

In Chapter 5, to minimize plasma-induced surface damage, two approaches have been used: etching process optimization and post wet etching. As the RF power of dry etching is minimized (13 W), the 1.6 µm high pillar sample shows a similar $\Delta U_{onset-plateau}$ as planar n-GaN. Alternatively, the damaged GaN surface can be removed by a post $NaOH_{(aq)}$ wet etching in the dark. After 15 mins of wet etching, the plateau j_{ph} of the 1.6 µm high pillars increases by 100% and U_{onset} shifts toward negative potential by 60 mV with respect to planar GaN. Specific surface traps whose energetic position is lower than the conduction band of n-GaN by 0.6 eV was observed using impedance spectroscopy. Trapping and detrapping of the deep-level traps result in a pair of anodic and cathodic peaks in the cyclic voltammograms in the dark.

In Chapter 6, we have porosified an n-GaN epilayer using electrochemical anodic etching in 0.5 M H_2SO_4 solution in the dark. Anodic etching of n-GaN was first discussed using cyclic voltammetry and chronoamperometry. The continuous increase of the anodic current as a function of potential indicates that hole supply is a limiting factor during anodic etching. In the etching chronoamperograms, the transient current oscillates as a function of time, which results from the balancing of oxidation of GaN and oxide dissolution. The pore morphology showed distinctive differences: from narrow branching pores to wide parallel pores when the etching potential was increased. The photoelectrochemical properties of the porous n-GaN layers have been discussed. For the porous GaN etched at 5.5-15.0 V, the plateau j_{ph} increased over 4 times; the $\Delta U_{onset-plateau}$ was all reduced by ~0.24 V with respect to unetched n-GaN. This indicates that carrier recombination inside the porous n-GaN and at the surface is suppressed.

In Chapter 7, to prepare the research of InGaN growth on nanostructured GaN templates, strain relaxation of the GaN nanopillars has been investigated using the in-

plane XRD measurements and finite element simulations. The in-plane lattice spacing of the top 5 nm of the pillars was accurately determined by the in-plane XRD measurements. The strain at the top of the GaN pillars is found to relax exponentially as a function of the pillar height, which agrees to the simulation. The impact of the pillar morphology on the strain relaxation were also discussed.

8.2 Comparison with state of the art

Table 1 lists the literature in which the plateau photocurrents ($j_{pla,ph}$) of planar and nanostructured (In)GaN are both reported. In the second column of the table, the increase of $j_{pla,ph}$ for nanostructured photoanodes with respect to planar cases is denoted as "$j_{pla,ph}$ increase (in %)". In the third column of the table, we present the $j_{pla,ph}$ of the nanostructured photoanodes. Since different light sources and light intensities are used in these works, the photocurrent onset and the plateau potential of photoanodes are not included in the table.

The achievements of the works in Chapter 5 [1] and Chapter 6 [2] are listed in the first and the second row, respectively. The 1^{st}-5^{th} rows and the 6^{th}-9^{th} rows show the nanostructuring works by top-down approaches and bottom-up approaches, respectively. High concentration of sacrificial reducing agents ($[Cl^-]$ or $[Br^-] > 0.1$ M) were used in all cited works except Ref. [9] (1 M $NaOH_{(aq)}$).

Nanostructuring of planar GaN epilayer using top-down approaches are desirable. Planar GaN grown by MOCVD is the most industrially mature approach to produce large-scale and cost-competitive GaN layers. However, most GaN nanostructures have been constructed using the bottom-up approaches (see Section 1.5). In this dissertation, we demonstrated that using dry etching the increase of $j_{pla,ph}$ can be comparable to that of bottom-up nanostructures. Moreover, we porosified the GaN epilayer using anodic etching. The increase of the $j_{pla,ph}$ for the porous n-GaN with respect to unetched epilayer is a bench mark (470%) for both bottom-up and top-down nanostructuring approaches.

Table 8.1: literature summary: plateau photocurrent ($j_{pla.ph}$) for planar and nanostructured (In)GaN. Ref. 1 and 2 are the values achieved in this disseration.

work description	$j_{pla.ph}$ increase (%)	$j_{pla.ph}$ of nano-structured (mA/cm^2)	Ref.
n-GaN nanopillars by dry etching of a epilayer using Ni cluster as mask	100 %	0.08	[1]
Porous n-GaN by anodic etching of a epilayer in 0.5 M $H_2SO_{4(aq)}$ in the dark	470%	0.14	[2]
n-GaN etched photoelectrochemically in 12 M $NaOH_{(aq)}$, followed by wet etching using $H_3PO_{4(aq)}$ (wt. 85%) at 200 °C	100%	0.83	[3]
Nanopillar by dry etching of a LED epilayer using Ni cluster as mask	450%[a]	1.80[a]	[4]
Porous n-GaN by anodic etching of a epilayer in 0.3 M oxalic acid in the dark	230%[b]	17.00[b]	[5]
n-GaN nanowires (NWs) grown by MBE	290%[c]	0.02[c]	[6]
n-GaN NWs obtained from nitridation of GaO NWs, where the GaO NWs were obtained by catalytic thermal reconstruction of a GaN epilayer	90%	0.80	[7]
InGaN nanowalls grown by MBE	57%[c]	0.15[c]	[8]
n-GaN ridges by selective area regrowth using MOCVD on a metal-strip-patterned planar GaN epilayer	260%[d]	80.00[d]	[9]

[a]obtained at U_{GaN-Pt} = 0.8 V due to undefined j_{ph} plateau.

[b]obtained at U_{GaN-Pt} = 1.5 V due to undefined j_{ph} plateau.

[c]calculated from generation of H_2 using j = nFN/At, where n is the charge transfer for hydrogen formation (n = 2), F is the Faraday constant (F = 96500 C/mol), N is the measured mole of H_2, A is the projected working area of the electrode and t is the measurement time.

[d]obtained at U_{GaN-RE} = 0.5 V due to undefined j_{ph} plateau.

8.3 Conclusions

Advantages and shortcomings of different surface roughening approachs

We demonstrated that the $j_{pla.ph}$ of the dry etched GaN pillars is enhanced by 100% with respect to pristine GaN epilayer [1]. We believe that the $j_{pla.ph}$ of the GaN pillars can be further increased when the pillars with a smaller dimension and higher pattern density are made. In this case, the total SCR will further increase and the charge neutral region will further reduce, leading to a more efficient carrier separation. The major shortcomings of this dry etching approach are the process cost and the process complexity, which requires depositions of metal and oxide, dry etchings and a thermal annealing. The first three processes require vacuum environment. Therefore, this approach is not expected to be applied industrially to produce low-cost photoanodes. However, this dry etching approach could provide a pattern-controlled pillar template, by using a well-defined mask via lithography, which enables systematical research on, for examples, the impact of surface band bending and surface states.

We also porosified the GaN epilayer using anodic etching [2]. The $j_{pla,ph}$ of the porous n-GaN increases by 470% with respect to pristine GaN. The advantages of this process are the process simplification and the low cost. Anodic etching only requires an acid or alkaline medium, in which gallium oxide dissolves, and a voltage-current control. The etching rate, depending on the applied bias, can be up to ~280 nm/min in our case (see Figure 6.3). Moreover, the small dimension of the GaN pores (20 nm -40 nm in our case, see Figure 6.4) suppresses carrier recombination and leads to high energy conversion efficiency. The pore morphology control can be a drawback of this technique, since the etching strongly depends on the local electric field. Although severe photocurrent variation between samples may not be expected if the photoanodes are large enough, the morphology variation at nanometer scales do complicate scientific discussion to some extent.

Light intensity effect on the photocurrent.

To suppress photo-corrosion of GaN, low intensity of UV light has been applied as the

light source in our work, leading to a lower $j_{pl,ph}$ compared with the literature (see Table 8.1). The light source used in this thesis is a Xe lamp filtered by an AM 1.5 G filter, which is a common light source used to simulate the solar spectrum in a laboratory standard. The integrated light intensity used in this thesis is 63 mW/cm^2 (the integrated light intensity of one sunlight = 100 mW/cm^2). Therefore, we expect that our light source simulates well the realistic situation with a j_{ph} enhancement of 1.6 under the one sunlight illumination condition. The details of the light source were described in Section 2.3.

When a higher UV light intensity is used, the $j_{pl,ph}$ increases as a result of more photocarriers at the surface of the photoanodes. The photocurrent enhancement is not always independent of light intensity. The photocurrent enhancement declines or saturates under illumination of higher light intensity if interfacial charge transfer becomes a rate-limiting process in the system (i.e. no sacrificial reagent in the solution, no efficient catalyst at the surface of electrodes). In this case, carrier lifetime for charge transfer increases, and the efficiency of carrier recombination therefore increases. We expect that this situation does not happen at least for $j_{pl,ph}$ < ~0.4 mA/cm^2 in our case. The reason is that Br^- has been used in the thesis as a hole scavenger to consume photo-holes at the surface of GaN. The diffusion-limited current of Br^-/Br_3^- oxidation for the solution we used (0.1 M HBr) is estimated to be at least > ~4 mA/cm^2 (see Figure 3.9). The electrochemical reaction is considered to be dominated by the kinetics for current lower than 10% of diffusion-limited current. Moreover, the convection introduced by the stirring of solution, which was applied in this work, further increases the diffusion-limited current density.

The electrical resistance is inversely proportional to the cross section area of the current path and proportional to the length of the current path. Therefore, the resistance from the GaN/solution interface to the metal contact for the nanoroughened GaN is higher than planar GaN film. For the case of the 1.6 µm high GaN pillars [1], the cross section diameters of the pillar are in the range of 250 nm- 450 nm (see Figure 5.4). After arriving the bottom of the pillars, charges can migrate horizontally in the GaN film to reach the metal contact. For the case of the 1.7 µm porous n-GaN [2], the dimensions of GaN between the pores are in the range of 20 nm-40 nm (see Figure 6.5). Electrons reach the

metal contact from the GaN/solution interface through complex current paths which are constructed by GaN between pores (see Figure 6.8). We expect, for both nanostructures, that the electrical resistance will be higher than the planar GaN film, particularly for the porous GaN considering its current path dimensions. Consequently, as j_{ph} increases with the light intensity, more potential will drop across the nanostructured GaN, leading to a lower j_{ph} enhancement.

8.4 Outlook

Direct water photoelectrolysis is a promising scheme to generate hydrogen renewably. Currently this approach is at the stage of laboratory research. There are still challenges for this technology innovation to be applicable to industrial production. From industrial perspective, the energy production cost is crucial. In this outlook, three research directions for n-GaN-based photoanodes are suggested to reduce the production cost of hydrogen: solar-to-hydrogen conversion efficiency, lifetime of photoanodes and production cost of photoanodes.

First, the optimal bandgap of semiconductors for water photoelectrolysis is ~1.8-2.0 eV, which compromises light absorption and overpotential for water electrolysis. Due to its high bandgap (3.4 eV), GaN only absorbs UV light. Material research to reduce the bandgap is necessary for GaN-based photoanodes. Indium incorporation into GaN is a typical approach to reduce the bandgap (see Section 1.4.1). Several groups have demonstrated $In_xGa_{1-x}N$ photoanodes for photoelectrolysis [10]-[15]. Chen et al. has examined the photoelectrochemical properties of a planar $In_{0.2}Ga_{0.8}N$ (E_g = 2.6 eV) [14]. Kamimura et al. reported that the incident photon-to-current efficiency of $In_{0.04}Ga_{0.96}N$ is ~40% for supra-bandgap light [15], which is comparable to GaN. However, due to different material properties, the epitaxy of InGaN with low defect densities on a conventional planar template is challenging (see Section 7.1). InGaN growth on a nano-patterned or nanopillar template may benefit from strain-relieving properties of the nanostructures. The formation of some structural defects in InGaN may be avoided.

The ultimate goal of the application is to generate oxygen from water at the n-GaN

photoanode and to generate hydrogen at the counter electrode. Although sea water containing Cl^- is a cheap and abundant resource for water photoelectrolysis, Cl_2 as a byproduct of the reaction can have negative impacts on the environment. The improvement of the photo-stability of n-GaN is a must. Other material(s) (e.g. TiO_2 and Al_2O_3) with high photo-stability can be coated on top of the n-GaN surface using technologies such as sol-gel, ALD or CVD. In this case, during photoelectrolysis, photo-holes are generated in n-GaN and are transferred to the second material at the surface for the oxidation of water. Moreover, reaction kinetics of water oxidation at most solid state surfaces is slow. Loading of specific catalysts (i.e. RuO_2, IrO_2, and PtO_2) on the surface is necessary to improve the reaction kinetics of oxygen formation. When interfacial charge transfer becomes more favorable, the photoanode is more robust during photoelectrolysis.

The material cost of the n-GaN epilayer is currently high. To achieve GaN epilayer grown on Si with low defect density by MOCVD growth, several intermediate layers and thick layer stacks (totally ~ 3 µm) are required. This takes a long growth time (typically > 4 hours) and consumes high volume of precursors. To reduce the cost of epitaxy, the material quality of n-GaN is sacrificed and defect density increases. In Chapter 6, we demonstrate that after anodic etching the photoelectrochemical properties of the porous GaN become less dependent of material quality (see Section 6.4). Carrier recombination in the bulk and at the surface is strongly suppressed for the porous GaN. Therefore, the porous GaN made of a cheaper n-GaN epilayer (high defect density) may still have a comparable photoelectrochemical property as the porous GaN made of expensive n-GaN (low defect density).

8.5 References

[1] W. J. Tseng, D. H. van Dorp, R. R. Lieten, P. M. Vereecken, R. Langer, and G. Borghs, *J. Phys. Chem. C*, **118**, 11261 (2014).

[2] W. J. Tseng, D. H. van Dorp, R. R. Lieten, P. M. Vereecken, and G. Borghs, "Nanoporous n-GaN photoanodes by anodic etching" (in preparation).

[3] A. M. Basilio, Y.-K. Hsu, W.-H. Tu, C.-H. Yen, G.-M. Hsu, O. Chyan, Y. Chyan, J.-S. Hwang, Y.-T. Chen, L.-C. Chen, and K.-H. Chen, *J. Mater. Chem.*, **20**, 8118 (2010).
[4] J. Benton, J. Bai, and T. Wang, *Appl. Phys. Lett.*, **102**, 173905 (2013).
[5] S.-W. Ryu, Y. Zhang, B. Leung, C. Yerino, and J. Han, *Semicond. Sci. Technol.*, **27**, 015014 (2012).
[6] D. F. Wang, A. Pierre, M. G. Kibria, K. Cui, X. G. Han, K. H. Bevan, H. Guo, S. Paradis, A. R. Hakima, and Z. T. Mi, *Nano Lett.*, **11**, 2353 (2011).
[7] J.-S. Hwang, T.-Y. Liu, S. Chattopadhyay, G.-M. Hsu, A. M. Basilio, H.-W. Chen, Y.-K. Hsu, W.-H. Tu, Y.-G. Lin, K.-H. Chen, C.-C. Li, S.-B. Wang, H.-Y. Chen, and L.-C. Chen, *Nanotechnology*, **24**, 055401 (2013).
[8] N. H. Alvi, P. E. D. Soto Rodriguez, P. Kumar, V. J. Gomez, P. Aseev, A. H. Alvi, M. A. Alvi, M. Willander, and R. Noetzel, *Appl. Phys. Lett.*, **104**, 223104 (2014).
[9] I. Waki, D. Cohen, R. Lal, U. Mishra, S. P. DenBaars, and S. Nakamura, *Appl. Phys. Lett.*, **91**, 093519 (2007).
[10] Y. J. Hwang, C. H. Wu, C. Hahn, H. E. Jeong, and P. D. Yang, *Nano Lett.*, **12**, 1678 (2012).
[11] C. Pendyala, J. B. Jasinski, J. H. Kim, V. K. Vendra, S. Lisenkov, M. Menon, and M. K. Sunkara, *Nanoscale*, **4**, 6269 (2012).
[12] M. Li, W. Luo, B. Liu, X. Zhao, Z. Li, D. Chen, T. Yu, Z. Xie, R. Zhang, and Z. Zou, *Appl. Phys. Lett.*, **99** (2011).
[13] H. Gerischer, *J. Electrochem. Soc.* **113**, 1174 (1966).
[14] W. Luo, B. Liu, Z. Li, Z. Xie, D. Chen, Z. Zou, and R. Zhang, *Appl. Phys. Lett.*, **92**, 262110 (2008).
[15] J. Kamimura, P. Bogdanoff, J. Laehnemann, C. Hauswald, L. Geelhaar, S. Fiechter, and H. Riechert, *J. Am. Chem. Soc.*, **135**, 10242 (2013)